DEVELOPMENT OF AN EARLY WARNING SYSTEM FOR PREDICTING ROCK BURSTS AND ROCK INDUCED DISPLACEMENTS IN SEISMICALLY ACTIVE MINING BLOCKS AT MUFULIRA UNDERGROUND MINE (DEEPS SECTION)

By

MUKUKA MOSES

A thesis submitted to the University of Zambia in fulfilment of the requirements for a Master of Engineering in Rock Mechanics

The University of Zambia

Lusaka

2024

DECLARATION

I, **Moses Mukuka**, declare that this thesis is a product of my own work. The work of other researchers in this thesis has been acknowledged accordingly. This research work has not been previously presented at this or any other university for similar purposes.

Signed: ……

Date: …….

CERTIFICATE OF APPROVAL

This thesis of **Moses Mukuka** has been approved as fulfilling the requirements for the award of Master of Engineering in Rock Mechanics by the University of Zambia.

Name	Signature	Date
Dr. V. Mutambo (Supervisor)	……..	…….
…… (Internal Examiner I)	……..	……
……. (Internal Examiner II)	…….	…….
…….. (External Examiner)	……	…….
…….. (Chairperson)	……	…….

DEDICATION

I dedicate this thesis to specific individuals without whom this masters would not have even commenced:

My lovely family for their consistent support and love, before, during, and after this work. In a very special way, Dr. Patricia Chipalabwe, cousin, best friend and competitor. This master‘s degree wouldn‘t have been easy without her encouragement.

Thank you, cousin.

ABSTRACT

Mufulira Mine has been in operation since 1933. The Mine is situated on the Copperbelt region of Zambia. It is predominantly rich in copper mineralization. Due to increase in mine depth which currently stands at 1,557 m, the mine has been experiencing geomechanical challenges such as rock failures due to excessive stress changes around some mining blocks. This has necessitated changes in mining sequences to suit the present geomechanical conditions such as development of de-stressing cross-cuts between 62 and 64 blocks. Additionally, blocks have been subjected to shotcrete support method to prevent possible rockbursts/rock falls which can endanger safety of men working in these areas.

This study applied laboratory geotechnical investigations for intact rock mass to determine unconfined compressive strength (UCS), secant and tangent Young's Modulus (E Sec and E Tan), and secant and tangent Poisson's Ratio (ν Sec and ν Tan), Brazilian and Triaxial Compressive Strength tests as well as geological field mapping methods to understand the Geomechanics mechanisms controlling rock burst prone mining blocks at Mufulira mine.

Laboratory findings indicated high values of Brazilian (Tensile strength) ranging from 7 MPa to 12.1 MPa, Uniaxial Compressive Strength (UCS) ranging from 126 MPa to 226 MPa and Triaxial Compressive Strength ranging from 124 MPa to 466 MPa were obtained. Damage mapping conducted in the footwall drives, cross-cuts and mining drives excavations indicate that there is a changing stress as one moves away from the retreating stope face to the east.

An early warning monitoring system at Mufulira mine has been developed through modification of the existing micro-seismic monitoring system to allow the quantification of exposure to seismicity and provide a logistical tool to guide the effort into the prevention and control of, and alerts to, potential rock mass instabilities that could result in rock bursts. Two geophones have been interconnected in series and connected to the network system via the optical fibre junction box within the seismically active mining blocks to enhance accuracy in picking up rockbursts and rockfalls. Geomechanics properties of rocks determined in the laboratory experiments, geotechnical and geological mapping results were used to suitably place the geophones in suitable proximities within the seismically affected mining blocks.

This modified micro-seismic monitoring system is susceptible to change if mining locations change due to changes in geotechnical and geological parameters such as rock types, jointing and fracturing.

ACKNOWLEDGEMENTS

This research would not have been possible without the financial, emotional, physical and spiritual support of the following: First and foremost, I would like to acknowledge my Heavenly Father and Creator, God Almighty, for the wisdom and insight given to me during my master‘s studies.

My main supervisor, Dr. Victor Mutambo, thank you for allowing me to express myself freely in my work; for the guidance, insightful criticism and the quickest responses rendered to me. Mr Ellan Chanda, for introducing me to this research topic that I have enjoyed greatly.

Mopani Copper Mines (MCM) for permitting my research work. In particular Mr. Johnstone Mwandu, from Rock Mechanics section, for facilitating the smooth flow of my data collection. Miss Mirriam Mapyapya from Rock Mechanics section, whose immeasurable assistance and dedication are highly appreciated. Mr. Alex Simutowe and Mr. Adriano Miti from Geology section, for helping me acquire the much-needed geological information key to this research. Mr. Roy Nyambe, Mufulira Mine Manager, for allowing me to get samples from the mine. Mr Beza Mwanza from the University of Zambia. Geotechnical Engineering Laboratory, for the support and input during laboratory analyses of samples.

Many thanks go to my friends and family. You lifted my burden when it seemed heaviest. I cannot say thank you enough. Lastly but not the least, the Ministry of Technology and Science for the financial support given to me during my study.

TABLE OF CONTENTS

LIST O F TABLES

TABLE OF LIST OF FIGURES

LIST OF ABBREVIATION AND ACRONYMS

Abbreviation	Description
E Sec	Young's Modulus Secant
E Tan	Young's Modulus Tangent
FoG	Fall of Ground
FPGA	Field Programmable Gate Array
Ga	Giga annum
ISRM	International Society for Rock Mechanics
L/D	Length/Diameter
MCM	Mopani Copper Mines
MCR	Mechanised Continuous Retreat
mL	Metre Level
PGV	Peak Ground Velocity
RMR	Rock Mass Rating
RMS	Rock Mass Strength
TCS	Tensile Compressive Strength
UCS	Uniaxial Compressive Strength
ZCCM-IH	Zambia Consolidated Copper Mines-Investment Holdings
YSFs	Yield Stress Fluids

CHAPTER ONE: INTRODUCTION

1.0 INTRODUCTION

This chapter gives general location of the study area, highlights major reasons which necessitated the research work to be undertaken, as well as the main and sub-objectives followed to achieve the desired outcomes.

1.1 Background

Base metal mining in Zambia has been in occurrence since 1926 (Limpitlaw, 1998). The entire mining process includes activities such as extraction of the ore and processing i.e. concentrating, refining, smelting, and acid production (Limpitlaw, 1998; Moukanna et al., 2018). The two mining methods; Open pit/cast and underground mining are being employed in Zambia. This research work was conducted at Mufulira underground mine, Mufulira, on the Copperbelt Province of Zambia.

Mufulira underground copper mine has been in operation since 1933, and the mine became prone to seismicity due to challenges associated with implementing a sustainable correct mining sequence that trigger rockfalls/rockbursts. In view of this, a live seismical monitoring system was installed in 1994 to monitor rockbursts and rockfalls. Micro-seismicity is attributed to the remnant pillar collapse, deeper mining and associated high abutment stress, and ore reclamation operations. Currently the system is operating with 19 active sensors and the mine is divided into seven (07) polygons for specific monitoring of micro-seismicity in different areas. The micro-seismical monitoring network has continued to be expanded and used for monitoring ground movement as the depth of the mine increases.

Rapid development of world economy has been gradually exhausting the shallow mineral resources of which Mufulira mine is not exceptional. More and more attentions have been paid to the mineral exploitation in deeper subsurface of the earth. For examples, current coal mining has reached 1,500 m in depth; geothermal exploitation has reached over 3,000 m, the depth for ferrous metal mining over 4,350 m and for oil and gas development 7,500 m. Therefore, deep mining is an on-going mining industry. However, more engineering accidents or hazards have occurred in deep mining (Kristoffer and Daniel, 2014). These accidents or hazards are difficult to be predicted with the current theories or experiences because the mechanical behaviours in deeper ground have not been well understood. On the other hand, current research and development in rock mechanics cannot solve the practical problems in deep ground engineering. A novel research and development scheme should be specifically designed for deep ground engineering (Siyanda, 2015). Particularly, fundamental concepts and basic theory

of rock mechanics should be revisited for deep ground engineering. For examples, what is the deep ground engineering? Is it measurable by the depth of ground? What is the essential difference of the mechanical properties of rock in deeper subsurface? Can the classical rock mechanics be applied to describe the mechanical behaviours of rocks in deep ground? How can the black box of rock mechanics in deep ground be revealed during the mining induced disturbance?

This research work focuses on the development of an early warning system that can help in predicting rockbursts and rock induced displacements in seismically active mining blocks at Mufulira underground mine (DEEPS SECTION) located in Mufulira, on the Copperbelt Province of Zambia.

1.2 SCOPE OF THE STUDY

The Mufulira mine site lies approximately 420 km from Lusaka City, close to Mufulira town on the Copperbelt province of Zambia. Mufulira has approximately 140,000 inhabitants (Encyclopedia Britannica academic online edition, 2013) of which a majority works in connection with the mine. The mine is owned and operated by Mopani Copper mines plc a subsidiary of Zambia Consolidated Copper Mines-Investment Holdings (ZCCM-IH). Mopani employs over 2,600 direct employees with a complement of contract labour of about 7,000, thereby making the total labour strength of approximately 9,600 working at Mufulira mine.

Figure 1.1 shows the location of the Mufulira mine in relation to the mining license area from google earth image with general lithological trend of north-west to south-east.

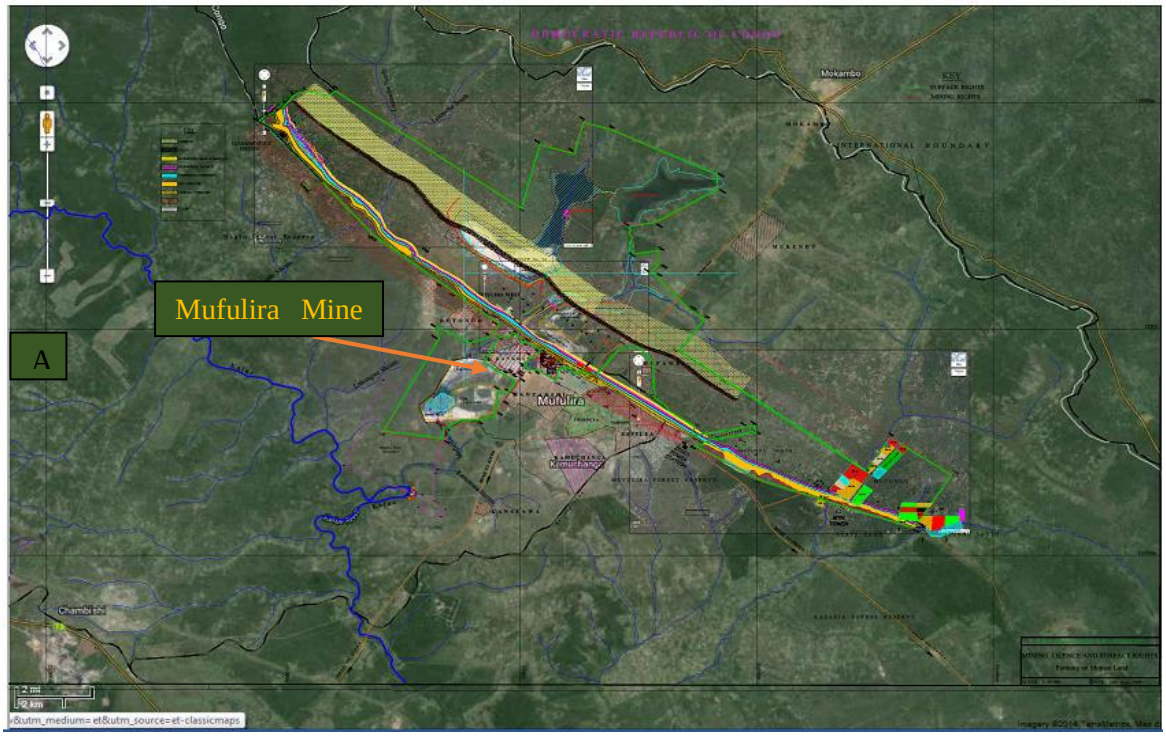

Figure 1.1. Showing location of Mufulira Mines licence area on google map

1.3 PROBLEM STATEMENT

Mufulira underground mine has been experiencing rockbursts due to seismic events during mining operations and primarily consist of sliding in the hanging wall and failures related to the stress concentrations in areas close to the crown pillars. The failures cause disruption in the mining operations and delays in production because once there is any seismic event, people working in underground sections are withdrawn and seek safety in waiting places until the event passes. These seismic events are accompanied by rock falls/rock bursts and have contributed to low productivity as well as creation of unsafe working environments which further have been endangering the safety of workers and machinery during mining operations. For instance, on 16th January, 2018, a seismic event of magnitude 2.8 occurred at 1440 mL causing damage to the mine infrastructure. Such events are accelerated by geological and geotechnical structures such as faults, unconformities, folds, bedding planes, aquifers, discontinuities and chemical weathering of rocks. However wrong mining practices due to limited time, such as wrong blasting techniques can also lead to seismic activities. Rock falls/rock bursts that result from seismic events are catastrophic hazards and require statistics or trends of rockburst ocurrences to be put in place, so that safety measures can be put in place

before they occur due to damage that accompany them such as underground infrastructure damage, machinery damage and possible loss of life of mine workers.

1.4 JUSTIFICATION OF THE STUDY

So far no detailed research work has been done to develop an early warning system for predicting rockbursts and rock induced displacements in seismically active mining blocks at Mufulira underground mine. All the previous seismic monitoring works have relied on the current Micro-seismic monitoring system that was established in 1994 when the underground mine was shallower 500 m deep than it is currently 1,500 m deep. The seismic monitoring system has however not fully addressed lapses in timely attending ground failures. Hence its effectiveness, accuracy and efficiency as the mine deepens must be critically analysed.

1.5 MAIN OBJECTIVE

To develop an early warning system that can predict rockbursts and rock induced displacements in seismically active mining blocks at Mufulira mine.

1.5.1 SUB-OBJECTIVES

a) Review previous and existing mining methods in terms of development, stope dimensioning, extraction practices and sequences
b) To conduct detailed geotechnical assessments of ground condition in all seismically active areas and mining blocks
c) To carry out rock and rock mass structural analysis using geological methods such as discontinuity and lithological mapping and drilled core logging in seismically active mining blocks.
d) To develop an efficient and cost effective early warning system for predicting rock bursts/rock falls in seismically active mining blocks.

1.6 RESEARCH QUESTIONS

a) What mining methods have been used previously and currently when mining within seismically active mining blocks?
b) What methods can be employed to conduct an assessment on the ground condition within the seismically active mining blocks?
c) What methods can be employed to conduct rock and rock mass structural analysis within seismically active mining blocks?

d) What efficient and cost effective early warning system can be used to predict rock bursts/rock falls in seismically active mining blocks?

1.7 SIGNIFICANCE OF STUDY

This study is important as it will benefit the rock mechanics section at Mufulira mine and the mining industry at large by raising safety standards while mining in seismically active mining blocks and enhance profitable productivity at the mine.

1.8 THESIS STRUCTURE

The following is the structure of the thesis:

Chapter one introduces the research topic by describing the background of the study and identifying the problem statement. It further highlights the study area, key research questions and the objectives of the study which are to be achieved through the outlined methodology.

Chapter two provides a literature review and theoretical background to the research. It gives a brief overview on the use of Micro-seismic monitoring system in deep mines as well as other possible early warning systems such acoustic emission intelligent real-time monitoring system

Chapter three gives the overall methodology and the step by step procedures used to achieve the research objectives. The data collection and analysis instruments and techniques are described in this chapter.

Chapter four presents the research findings of this study. The chapter presents the laboratory results obtained from experiments conducted on core samples collected from Mufulira underground mine. All laboratory experiments were done at the university of Zambia great east road campus. The chapter also provides findings of desk studies to establish the mining types and sequences being used at Mufulira underground mine.

Chapter five gives the flow chart of the development of a modified Micro-seismic monitoring system capable of predicting rockbursts and rock induced displacements within seismically active mining blocks at Mufulira underground mine.

Chapter six provides the conclusions drawn from the study based on the data analysis and findings of chapters four and five. These conclusions were used to deduce relevant recommendations for implementation.

1.9 SUMMARY

The first chapter introduced the research, including the background of the study, the study area, the objectives of the research and the methodology used to achieve these objectives. The study was necessary as it will benefit the rock mechanics section at Mufulira mine and the mining industry at large by raising safety standards while mining in seismically active mining blocks and enhance profitable productivity at the mine. The chapter also provided a summary of the layout of the thesis. The next chapter provides a detailed review of literature on the application of Micro-seismic monitoring system in underground mines.

CHAPTER TWO: LITERATURE REVIEW

2.1 INTRODUCTION

In this chapter, all the necessary information about the Mufulira underground mine which include its geological setting and mining methods used. Literature written by other researchers about seismic monitoring systems and any other system with potential to operate as an early warning system in determining rock bursts and rock falls in underground mines will be reviewed as well.

2.2 GENERAL DESCRIPTION OF MUFULIRA MINE

Mining at the Mufulira mine site conducted through two underground mines: Mufulira main Central and Mufulira East Portal. Mining operations used to extend over 5.5 km of strike length, but since the Mufulira West deep mining area was mined out and closed down, current operations now take place over a 3 km strike length. The total ore reserves at the Mufulira mine including the shallow oxide ore with a cut-off grade of 1.5% is 19 million tonnes only including proven and probable resources, with the inferred resources included it is 20 million tonnes. Out of this the Mufulira main Central has 16 million tonnes. The annual production of the mine is 1.5 million tonnes. After a newly commenced shaft down to the 1507 m level is developed, the production is expected to increase to 2 million tonnes. The mine has with the current metal price and with the reserves down to the 2020 m level, a mine life of 25 years.

2.2 MINING METHODS

There are three types of mining methods currently in use at the Mufulira mine; In the Mufulira East Portal, the mining method employed is Room and Pillar with waste rock backfill. Mining operations extend down to its deepest level of 140 m. The ore is then trucked to the surface and treated in the VAT-Leach plant. In the Mufulira main central the mining methods are called Mechanized Continuous Retreat 1 and Mechanized Continuous Retreat 2 (MCR1 and MCR2) respectively. These are essentially variations of the sublevel open stoping mining methods and are the most widely employed methods in the Mufulira mine. In the shallower part of the main central, Room and Pillar with waste rock backfill is employed. As a complement to the mentioned mining methods the mine also employs in-situ leaching of old stopes. Due to the nature of this research the focus of this case study has been on the mining operations at the Mufulira main central and within the Mufulira Deeps section. The Mufulira main central consist of eight vertical, one sub vertical and three sub inclined shafts that provide logistical support to the mine from the surface to the Mufulira Deeps section. The Mufulira Deeps section

is the deepest area in the Mufulira Mine Central and mining is currently being conducted up to 1,557 m level.

2.3 GEOLOGICAL SETTING

Basement at Mufulira comprises granodiorite, intruded into the Palaeoproterozoic, Eburnian (2.05 to 1.85 Ga) calc-alkaline magmatic arc sequence of metasedimentary, metavolcanic and intrusive rocks of the Lufubu Metamorphic Complex. The topography of the basement at the onset of Neoproterozoic Katangan Supergroup, Roan Group sedimentation was irregular, with the highest ridges up to 150 m above the deepest valleys (Fleischer et al., 1976). This topography was influenced by the differential resistance to erosion of the granodiorites and the Lufubu schists. Mufulira orebody is the largest of the orebodies found on the north-east margin of the Kafue Anticline, and is principally hosted by arkose/quartzites (Figure 2.1).

At Mufulira mine, the basal Lower Roan Subgroup is 200 m to 250 m thick, and has been interpreted as having been deposited within a depression within the pre-Katangan basement. It unconformably overlies the Palaeo- to Mesoproterozoic basement complex, and comprises, from the base: Footwall Formation, part of the Mindola Clastics Formation, 0 to >150 m thick, this sequence is divided into three 'sub basins' by palaeo hills which cut right through the formation. Consequently there are considerable variations in thickness of this part of the section (Figure 2.1). It comprises;

- Basal Conglomerate
- Footwall Quartzite
- Ore Formation
- Inter B/C Horizon
- Inter A/B Horizon
- Marker Grit

Basal Conglomerate, 0 to 20 m thick- a poorly developed boulder to cobble conglomerate, best represented on the margin of a pronounced palaeo hill. Footwall Quartzites and Grits, 0 to 150 m thick - the principal lithology is a grey arkosic cross bedded sandstone, interpreted as including both aeolian and aqueous varieties. Several grit lenses are mapped, as are shale/arenite interbeds near some of the palaeo highs. The arkosic quartzites have up to 35% anhydrite cement in places and range from grey to reddish in colour.

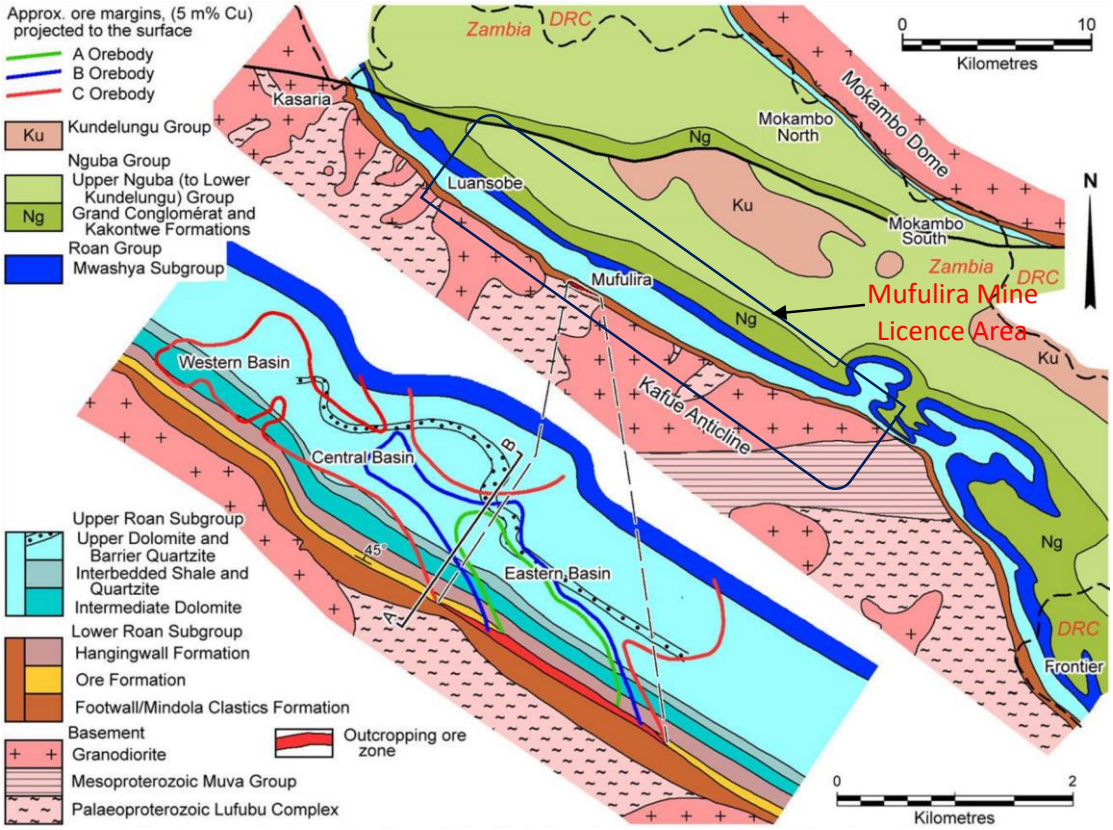

Figure 2.1 Showing Geology of Mufulira Mine Area (Porter, 2013)

Ore Formation, 30 m to 80 m thick - containing the three main ore intervals, the three "Orebody Quartzites". Unlike most of the other major deposits on the Copperbelt, the ore at Mufulira is almost exclusively within 'arenites' and not in the immediately overlying fine sediments. Basement highs have a strong influence on ore, although none ever cuts the lowermost 'C' orebed. This implies a period of erosion between the Footwall and Ore Formations. The Ore Formation may be subdivided as follows;

'C' Orebody Quartzite, 3 to 20 m thick - the lowest and most important and laterally extensive orebody, with a strike extent of 5800 m, averaging 2.5 to 3.5% Cu, mainly as bornite. The gradation from the footwall to the ore quartzites shows a marked increase in silicification and loss of the prominent dark cross beds/laminae that define the stratification, to a more massive quartzite. The 'C quartzite is grey, fine to medium grained, feldspathic, (but glassy when hosting ore), with some grit bands and a chaotic breccia zone. A black carbonaceous massive quartzite occurs within the upper section of this unit in the zone of maximum development of the 'C' quartzite. It contains up to 2% free carbon and abundant sericite. Identical carbonaceous arenites are found within the other two orebodies, but not elsewhere in the sequence. Within the ore there are buff to pale green argillaceous shale bands developed within the quartzite,

generally <1 cm thick. Anhydrite and gypsum cements are abundant in sections of the quartzite, although within the ore dolomite and sericite are the principal interstitial cements. As the top of this unit is approached within the ore flecks of dolomite increase upwards towards the overlying dolomitic siltstone 'mudseam'.

Inter 'B/C Horizon, 0 to 15 m thick - commences with a 0.3 to 1.2 m (averaging 0.5 m) thick dolomitic siltstone, known as the 'Mudseam', which forms a cap to the 'C' Orebody. In general the change from the 'C' Orebody Quartzite is abrupt, apart from the increase in flecks of dolomite in the upper quartzite. Where sighted underground this is a pale silty unit with associated anhydrite. Further to the east it has cherty layers.

The 'Mudseam' grades upwards into a 0 to 1.5 m thick mid-grey banded dolomite and siltstone unit which passes in turn into a 1.5 to 4 m thick interbedded shale and quartzite. This is followed by the 2 to 12 m thick Inter B/C Quartzite which is a greyish pink to a clear and glassy feldspathic quartzite with grit lenses and anhydrite cement. As with the quartzites in the footwall to the main 'C' Orebody Quartzite, these arkosic quartzites are cross bedded, and again the bedding disappears and the rock becomes more massive and siliceous as the base of the 'B' Orebody is approached. This banding tends to have diffuse boundaries in places sighted underground, suggesting a replacive origin. Sections of the Inter B/C Quartzite are mineralised.

A barren, extensive stromatolitic dolomite lens occurs at the top of the unit on the western fringe of the 'B' Orebody at the contact with the overlying [1] B' Orebody Quartzite. Well-developed collenias are observable (Malan, 1964). Copper mineralisation is antipathetic to the development of the stromatolitic lens/reef.

'B' Orebody Quartzite, 3 to 15 m thick - grey to dark grey feldspathic quartzite, similar to the 'C' Orebody Quartzite. Black carbonaceous quartzite is also present, but only in the central mining area. Also present, as in the 'C' Quartzite, are slump breccias and grit bands. It thins towards the west where it becomes more argillaceous, but thins more rapidly to the east (as do the 'A' and 'C' Orebody Quartzites). On passing from the Inter B/C Quartzite to the 'B' Orebody Quartzite the rock becomes more massive and siliceous.

Inter 'A/B' Horizon, 0 to 30 m thick - commences with a 3.5 to 6 m thick white to pink sugary dolomite (the Lower Dolomite) with associated chert and containing up to 30% anhydrite. This dolomite unit forms the cap of the 'B' Orebody. It is overlain by a 10 to 15 cm thick, well mineralised gritty dolomite known as the 'Gritty Marker', with bornite-chalcopyritechalcocite (up to 4% Cu) and sometimes primary uraninite. Following this is a thin (0.5 to 1.5 m thick) barren algal/stromatolitic bed, then 5 m of dark greenish grey argillite sporadically capped by

a further thin algal dolomite, then 2 to 4 m of interbedded quartzite and argillite, followed by the 2 to 15 m thick pink to rusty Inter A/B Quartzite which is mineralised to ore grade in parts.
'A' Orebody Quartzite, 3 to 12 m thick - grey to dark grey feldspathic quartzite, similar to the B' and 'C' Orebody Quartzite. Black carbonaceous quartzite is again present, but as for 'B', only in the central mining area. A characteristic of the unit is the presence of pebble bands towards the top. Ore grades are generally 4.5 to 5.5% Cu as chalcocite and bornite.
Hanging-wall Formation, 65 to 75 m thick - comprising Lower Argillaceous Quartzite, 35 to 65 m thick - commencing with a shale band and comprising mainly a grey green argillite with irregular arenite bands, this unit caps the 'A' Orebody Quartzite and the orebody itself. Three main dolomite bands occur within it, with the Dolomite and Shale at the top. Gypsum and anhydrite are conspicuous as fracture and joint fillings.
Marker Grit, 4 to 6 m thick - gritty pink quartzite, the beds of the Marker grit lie approximately midway between 'A' quartzite hangingwall and the base of the Upper Roan group. Upper Argillaceous Quartzite, 20 to 45 m thick - sandy argillite, similar to the Lower Argillaceous Quartzite, with a dolomitic band at the top.
Glassy Quartzite, 6 to 12 m thick - very hard and compact, glassy white to grey quartzite with minor shale bands. At the top a persistent (over 100 km strike) thin mineral zone is present as a 2 to 3 m thick partly carbonaceous dolomite with minor pyrite, chalcopyrite and bornite.
The Lower Roan Subgroup is conformably overlain by the Upper Roan Subgroup, which is 10 to 800 m thick, being represented largely by breccias at it thinnest, and is from the base:
Intermediate Dolomite, which comprises dolostone, talc-schist, argillite and minor quartzites. The base of the unit is marked by a 0.5 to 1.5 m thick grey silty dolostone, in which pre-consolidation slumping and brecciation are obvious.
This is followed by a thin and impersistent dark grey dolostone, and by up to 25 to 35 m of dolostone and talc-schist, before the Middle Quartzite, which is, in turn, overlain by the Upper Intermediate Dolomite sequence. The 6 to 12 m thick Middle Quartzite is grey to greyish-pink, glassy and slightly dolomitic. The Upper Intermediate Dolomite is 30 to 45 m thick, and is predominantly dolostone to the east, with argillite beds up to 6 m thick near the top. Further argillites appear and increase in frequency westward, to dominate in the west, where they are greenish-grey, massive and usually carry disseminated pyrite. Gypsum and anhydrite occur throughout the Intermediate Dolomite, except in the quartzite beds (Brandt et al., 1961).
Interbedded Shale and Quartzite, which is generally 45 to 50 m thick and is composed of shale, quartzite and minor dolostone. The base of the unit is marked by the Blue Shale, a massive to weakly bedded carbonaceous shale carrying large blebs of pyrite, varying from 2 m in the east

to 12 m in the centre and 5m in the west where it is less carbonaceous. The beds above the Blue Shale vary markedly in facies and thickness laterally. Eastward the Blue Shale disappears, as do the other facies of the Interbedded Shale and Quartzite, and the Intermediate Dolomite, such that the Glassy Quartzite at the top of the Lower Roan, is overlain by a condensed sequence of white dolomite and breccia. West of the mined area, the Intermediate Dolomite is dominantly arenaceous, but then becomes more shaley and decreases in thickness from 50 to <20 m (Brandt et al., 1961).

Upper Dolomite, that is >500 m thick and is predominantly composed of white talcose and pink dolostone, with minor greenish-grey argillite and dolomitic argillite. An intersection of 22.24 m at 2.42% Cu has been encountered at the base, separated from rocks of the Lower Roan Group by a polymictic breccia. Abundant breccias appear 200 m above the base of the unit. However, in the east of the deposit area, these breccias extend down to the base of the Intermediate Dolomite. They comprise rounded to angular clasts of dolomite, argillite/shale and chert, from <1 to —10 cm in diameter, set in a dark greenishgrey argillaceous matrix. The enclosing quartzites and argillites are partially brecciated. In the middle of the unit, the Barrier Quartzite member has been locally recognised, but is of limited extent. It is overlain by dolomite, talcose dolomite and argillite/shale and is 250 to 450 m thick (Brandt et al., 1961).

The Mwashia/Mwashya Subgroup, which at Mufulira is 450 to 600 m thick, and is composed of shale, black-carbonaceous shale and grey, glassy quartzite with minor dolomite and grit bands. Nearby, it also locally includes some dolostones and interbeds of up to 30 m of grey-pink quartzite (Brandt et al., 1961), and is shown by Wimberley et al. (2010) as comprising a basal conglomerate with clasts of Roan Group rocks, a middle unit of siliciclastic rocks, carbonates and shales, overlain by an upper suite of sandstones and shales.

The Nguba Group, commences with 140 to 150 m of grey shaly and slightly carbonaceous Grand Conglomérat diamictite, containing a variety of poorly sorted clasts. This is overlain by the Kakontwe Limestone, which is 450 to 600 m thick, composed of grey to white, and moderately well bedded, dolomite and minor shale at Mufulira. The overlying shales, carbonaceous shales, argillite and minor quartzite are up to 3500 m thick in the middle of the syncline to the north of Mufulira, and belong to the upper Nguba and Kundelungu groups (Brandt et al., 1961).

Mufulira mine is located on the southwestern limb of the NW-SE trending, asymmetric Mufulira Syncline, on the northeastern margin of the regional Kafue Anticline. The host sequence and ore deposit, overall, dips at 45 ^{0} NE on the SW limb, but is locally steep to overturned.

The Mufulira deposit is elongated and plunges at -10 ^{0} to the NW. The NE limb of the Mufulira Syncline, which laps onto the Mokambo Dome, is mostly steep to vertical. This limb hosts the smaller Mokambo North and South mineralisation, 12 to 15 km to the NE of Mufulira. In the intervening keel of the synline, the Ore Formation is estimated to be as deep as >10 500m below the surface.

The basement topography at Mufulira mine appears to have had a strong influence on the distribution of ore at the mine. A number of basement rises cut through the sequence, almost to the orebodies, with the highest grades tending to flank these basement hills, while increased pyrite is common over the crests of some of these hills (Freeman 1988). However, a palaeo hill or ridge has never been found to protrude into the lowest, or C orebody, implying that these were not hills during the deposition of the ore host (Fleischer, Garlick and Haldane, 1976). This implies a control based on events during compaction when these buried hill/ridges would have influenced the geometry of the compacting sequence. Where the Footwall Formation is absent and the ore rests on basement, the basement itself may be mineralised. In these locations, disseminated chalcopyrite and/or native Cu is present to about 0.5% Cu for 1 to 2 m into the basement. The base of each of the "Orebody Quartzites" corresponds to an increase in the silicification of the hosts sediments, and the disappearance of banding and argillaceous and arkosic content. The upper limit of each orebody is usually marked by the appearance of fine dolomites and argillites.

Copper sulphides occur at 21 distinct stratigraphic positions within the Mufulira mine, of which only three are economically exploited (Fleischer, Garlick and Haldane, 1976). For simplicity

in mining the eighteen different ore beds are grouped into five broad mining units, termed the 'C', lnter B/C, ' B', 'Inter A/B and 'A' (Figure 2.2).

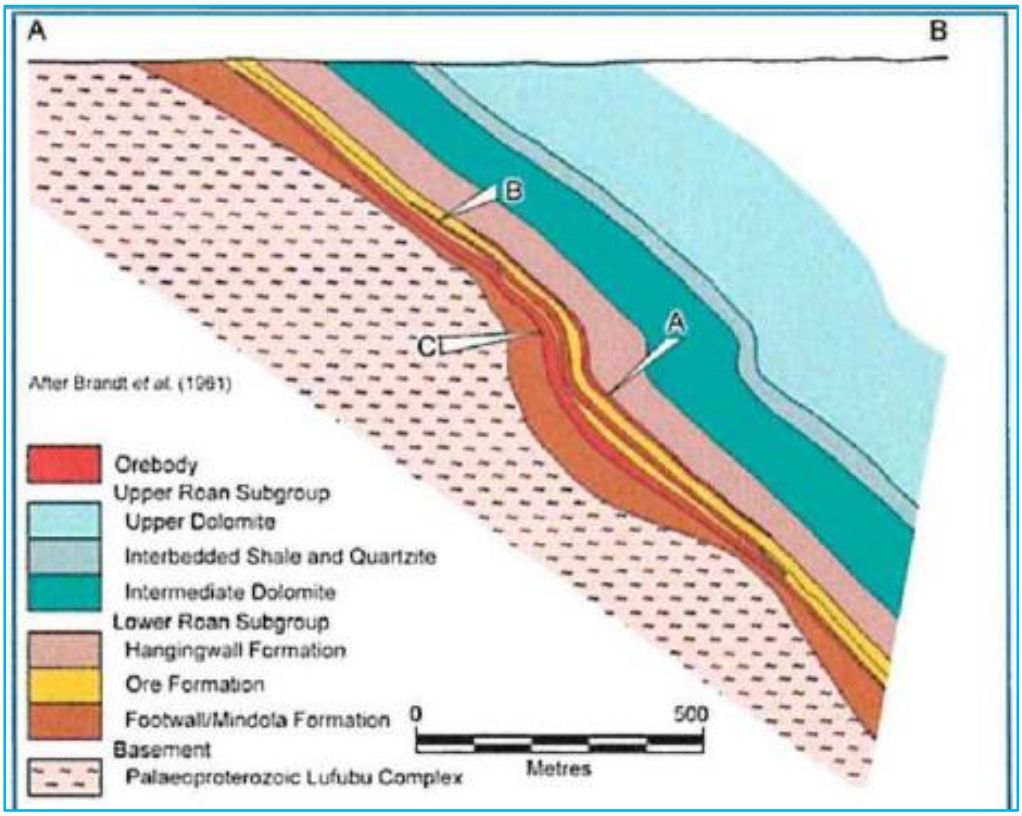

Figure 2.1A Sowing geological cross-section from Figure 2.1 through the Mufulira ore deposit

The 'C' Orebody is the lowest and most extensive, having lateral dimensions of 5800 m, and is continuous down dip for >1300 m, to at least the 1500 m level and is up 23 m thick, averaging -14 m. The 'A' and 'B' orebodies cover smaller areas, of 1800 x 900 x 6 (up to 13.7) m, and 3200 x > 900 x 7.6 (up to 15.2) m. Ore, while being largely confined to the 'A, 'B and 'C' orebodies, is also found within the Inter B/C and Inter A/B quartzites, and at one point where all three overlap is continuous from the base of the 'C' Orebody Quartzite to the top of the 'A' Orebody Quartzite, a thickness of up to 65 m. Elsewhere sections of the 'Inter B/C' and 'B' orebodies are mined together, with laterally narrow and weak mineralisation within the lower Inter B/C argillites and dolomites, and a wider connecting zone of ore grade in the Inter B/C Quartzite, mushrooming out to connect to the overlying 'B' orebody.

Within the 'Inter B/C' and 'Inter A/B' units, mineralisation is generally absent from the finer argillaceous and dolomitic beds, and abundant within most interbeds of arenites, although absent from some of the thicker coarse beds. The stromatolitic dolomites are almost invariably

barren, although laterally developed arenites and those between the stromatolites may contain sulphides. However, locally the fine sugary dolomites I immediately overlying the 'B' Orebody may contain minor Cu mineralisation, generally < 1 0/0 Cu.

The base of each of the 'A', 'B' and 'C orebodies closely corresponds to an increase in silicification of the host sediments and the disappearance of the primary sedimentary structures, particularly lithological banding. In these positions the characteristic banding gradually disappears, the rock becomes less argillaceous/feldspathic and grades to more siliceous massive quartzite. In general the 'grade boundary' base of the 'C' Orebody, for example is close to the disappearance of bedding, usually within 1 to 2 m above or below this change. In some cases however, up to 20 m of low grade 1 to 2% Cu mineralisation occurs in this transition zone which may be carried by the higher grade overlying ore. The top of the individual orebodies is generally determined by the appearance of the overlying fine dolomites and argillites. In the case of the 'C' Orebody the top of the orebody is generally very close to the overlying 'Mudseam', although grade commonly begins to decrease over the last metre below the contact. As the Cu drops off, the dolomite content increases correspondingly.
The lateral equivalents of the 'C' Orebody Quartzite contains anomalous Cu levels, stated as being of the order of 0.1 to 0.5% Cu at a distance of 1 km to the west of the margin of the orebody. In this zone, trace chalcopyrite and pyrite are recognised. Within the mine, the lateral equivalents to the 'B' and ʿA' Orebodies contain 0.2 to 0.5% Cu in less siliceous but more argillaceous/feldspathic quartzites from 500 m to 1 km along strike from ore. Apart from the sulphide content, these rocks are hard to distinguish from the orebody hosts, except by direct comparison where the marginal difference in silica and argillaceous/feldspar content is just discernible.

The Mokambo North deposit occurs as 5 lenses, which average 6.2 m in thickness, with respective strike lengths and dips of 200 m - 45^0 SW; 850 m - 50^0 SW; 100 m - 65^0 SW; 1250 m - 65^0 SW; and 450 m - 55^0 SW. Mineralisation is hosted by one or two horizons within a Lower Roan Subgroup sequence of quartzites, greywackes, grits and conglomerates. Copper sulphides, predominantly chalcopyrite, ranges from 1.12 to 2.22% Cu over thicknesses that vary from 2.8 to 21.8 m. The thickest intersections are to the south. The deepest mineralisation encountered is at 1200 m. Resources total 12.65 I Mt at 1.61% cu.

The Mokambo South deposit is hosted by Lower Roan Subgroup quartzites, greywackes, grits and conglomerates that strike north-south and dip at 55^0 W.
Mineralisation is confined to a single unit near the top of the sequence. The best mineralisation was near the boundary with the Mokambo North deposit. Chalcopyrite is the main copper sulphide, with grades of 1.32 to 3.62% Cu, over thicknesses of 1.5 to
13.6 m, averaging 4.6 m. Mineralisation persists over a strike length of 1000 m, and to depths of between 100 and 1000 m below the surface. Resources are 5.98 Mt at 2.38% cu.

The Luansobe deposit occurs within quartzites in the same host sequence as Mufulira, also on the SW limb of the Mufulira Syncline, but 6 km to the NW. Resources are quoted at 8.4 Mt at 1.6% cu 0.13% co (Selley et al, 2005), or 5.6 Mt at 1.58% cu Total, 0.76% Cu Acid Soluble.
The host sequence comprises a 0 to 70 m thick Footwall Formation composed predominantly of grits and poorly bedded conglomerates, with silty partings. The grits grade up into feldspathic to argillaceous quartzite. The thickness varies with the basement topography.

The overlying Ore Formation is 50 to 110 m thick, and commences with the 15 to 30 m thick E Quartzite, which is moderately well-bedded, feldspathic and argillaceous, grading to a fine to medium grained and gritty variety, and containing beds of grit, conglomerate and sandstone, with argillaceous partings. The overlying D Quartzite has a gradational contact, and is 6 to 8 m thick. It comprises massive to distinctly bedded, light grey, gritty and feldspathic quartzite, grading upwards into a greywacke. The succeeding C Quartzite is similar to the underlying D, but is locally dark, due to minor carbonaceous material and pyrite. This is overlain by a 1.5 m dolomitic shale, termed the "Mudseam", followed by the 9 to 20 m thick B Quartzite, which is similar to the C and D Quartzites, and is, in turn, overlain by the 8 to 20 m thick Lower Dolomite and Shale. The formation is capped by the 6 to 14 m thick A Quartzite, similar to the other quartzites, although it contains numerous cavities filled with anhydrite.

The Hangingwall Formation is made up of the 20 to 33 m thick, massive to poorly bedded Argillaceous Quartzite, comprising an argillaceous quartzite to sandy argillite, with shale partings, a local pink dolostone and an uppermost 5 m of siltstone with argillite partings.
The overlying 5 to 10 m thick, light grey Marker Grit is a pitted, glassy feldspathic quartzite with quartz and feldspar grit, followed by the 15 to 27 m thick, massive to poorly bedded, grey, Sandy Argillite, and then the 25 m thick, light grey, poorly bedded and hard Glassy Quartzite.

Sulphide mineralisation occurs as pyrite, chalcopyrite, bornite, chalcocite and sphalerite. Pyrite is dominant from the Mudseam to the top of the A Quartzite. Pyrite with chalcopyrite and local chalcocite are found in the C Quartzite; chalcopyrite, bornite and chalcocite in the D Quartzite, and only chalcocite in the E Quartzite.

The Kasaria deposit is located adjacent to, and passes under the DRC border, hosted by the same stratigraphic sequence seen at Mufulira. Mineralisation occurs over a 3 km strike length and 500 m width, as discontinuous lenses at three stratigraphic positions, the A, B and C horizons seen at Mufulira. These lenses cross the DRC border at a depth of 200 to 1000 m. Grades range from 1 to 6% Cu over widths of 1 to 18 m, averaging 4.5 m. The host sequence dips at 25 to 30 ^{0} NE. Most of the mineralisation in Zambia is relatively shallow, at depths of 100 to 300 m, and is mainly malachite, cuprite, chrysocolla, native copper and chalcocite in the upper sections, grading down into a primary ore of pyrite, chalcopyrite and minor bornite. Without a 3 m thickness cut-off, the main lens might contain —20 Mt at 2.51 % Cu. However, applying cut-offs, the resource is estimated at 5.8Mt at 2.57% cu.

2.3.1 Mineralogy and Mineralisation

According to Fleischer (1976), there is a general antipathetic relationship between the presence of sulphides and anhydrite within the host sequence. Barren interbeds within the Ore Formation, the intermediate hanging wall quartzites, and barren 'ore' horizons adjacent to the Mufulira deposit contain as much as 19 to 31% anhydrite. On the other hand the orebeds themselves contain interstitial dolomite with little or no anhydrite. He also mentions that the drainage problems at Mufulira are due to the dissolution of the high anhydrite/gypsum content of the wall rocks, whereas the ore is less permeable, more competent and less weathered. The sulphides are characteristically disseminated within particular beds as described above.

These disseminated sulphides are found in a number of forms, including,
Discontinuous bands of sulphides, occurring either as 'fly speck disseminations (much less than 1 mm), blebs (1 to 2 mm) or thin lensoid bands (1 to 2 mm), defining bedding planes at irregular intervals across the host bed, or as irregular clots of weak to strong disseminations up to 10 cm across. In the basal sections of the 'Orebody Quartzites' these sulphides are often concentrated on the foresets and bottomsets of crossbeds, accompanied by rounded heavy minerals.

Irregular angular or jagged (but not rounded) clots of weak to dense disseminations of sulphides whose elongation is influenced by bedding, but may also be strongly transgressive. These clots are from a few millimetres across to 10 cm or more. While they may appear dense, the sulphides are still largely interstitial to the silicate minerals of the arenite hosts.

The zonation of ore minerals at Mufulira is more complex than at the other deposits of the Zambian Copperbelt. Within the ‘C’ Orebody, chalcopyrite is the dominant sulphide mineral, although in sections this grades to bornite dominant. The average grade is 2.5 to 3.5% Cu. Within the 'B' Orebody the predominant ore mineral is bornite and the average grades are from 3.5 to 4.5% Cu . The uppermost 'A' Orebody is also the highest grade, generally averaging 4.5 to 5.5% Cu, with bornite and chalcocite. A small pocket of uranium mineralisation is found at the top of the 'A' orebody in the central section, consisting of yellow uranium ochres. Black disseminated uraninite also occurs at several horizons within the 'C' Orebody quartzite on the western flank of a palaeo ridge, with some associated bright secondary salts adjacent to the ridge.

2.3.2 Mufulira Ore

Ore styles at Mufulira mine samples from the lower 'C' Orebody and the middle of ‘B’ Orebody. Both are silicified quartzites, in which bedding is not obvious, in contrast to the bedded, variably argillaceous arenites stratigraphically above and below each. Copper sulphides are dominantly bornite in the 'B^{I} Orebody, but with significant chalcopyrite also in the 'C Orebody. These sulphides occur as both fine 'flyspeck' disseminations.

2.3.3 Alteration

Alteration is not specifically described within the much of the literature on Mufulira. However underground traverses strongly infer that there is enhancement of silica, alteration of arkose feldspar to sericite and anhydrite to dolomite within the ore zones at Mufulira. As described above, well developed banding within the footwall arkosic quartzites fades as the base of the ore is approached and the rock becomes more siliceous and sericite rich, with the virtual total loss of primary sedimentary features coinciding with the base of the orebody. Similarly the host quartzites are less siliceous and more feldspathic to argillaceous along strike where not strongly mineralised. The increase in silica in the lower orebody corresponds to the presence of authigenic overgrowths of silica on corroded detrital quartz grains, lowering of the detrital

feldspar content and increase in the presence of sericite. The detrital feldspars of the footwall arkosic quartzites are generally microcline, while the matrix contains appreciable albite or oligoclase which appear to be authigenic. The more siliceous quartzites have also lost their original sedimentary features almost completely by recrystallisation of quartz and feldspar as seen in thin section. This might be taken to imply the introduction of silica, producing authigenic feldspars, altering feldspar to sericite and removing part of this argillaceous material. The silicification decreases upwards into the orebodies, while the argillaceous (sericite) content increases. The characteristic carbonate cement (dolomite) within the orebodies, with varying accompanying anhydrite, contrasts with the anhydrite cement of the lateral equivalents and footwall arkosic quartzites. This also implies alteration of original, mainly diagenetic cement anhydrite, during mineralisation.

From personal observation, there is at the base of the 'C' Orebody at Mufulira, a transgressive 'red line' oxidation front marking the change from underlying oxidising conditions to sulphide rich reduced conditions within the orebody, similar to that described at Musoshi. At Mufulira, the bornite and chalcocite zones do not contain more free Fe oxides than the chalcopyrite zone as is common in some other sedimenst hosted coper deposits.

At the top of the best developed section of each of the orebodies, there is a black carbonaceous quartzite lens known as the 'Greywacke'. This lithology is characterised by the presence of up to 2% carbon and a high percentage of sulphides. Like the other ore bearing arenites it has a low feldspar and elevated sericite content. On its lower and lateral fringes it passes gradationally through a 'mottled sandstone' to the orebody quartzite. The mottled sandstone is a lateral equivalent of the black carbonaceous quartzite, and apart from the mottling, differs from the latter mainly in its lower preserved carbon and increased carbonate. It comprises light and dark grey diffuse patches subparallel to bedding or randomly distributed. Copper minerals and organic carbon are more abundant in the dark grey parts while the lighter sections contain more carbonate and are sometimes more porous, probably due to the dissolution of the carbonate and anhydrite constituents.

In general, there appears to be an inverse relationship between carbon and Cu within these black carbonaceous quartzites. In the 'C' carbonaceous quartzite which contains up to 2% carbon, the grade is relatively low compared to the 'B' and A analogues. For example the 'A' carbonaceous quartzite in places has up to 20% Cu sulphide accompanied by only -0.5% carbon.

2.3.4 Leaching and Oxidation

Leaching and oxidation of sulphides in the orebodies is general to depths of 60 m below surface, and sporadic below that. Oxidation in some footwall quartzites and grits reaches depths of 600 m or more. These beds are leached and porous (resulting from the dissolution of the up to 35% anhydrite they contain), in contrast to the more silicified orebody quartzites. Below the leached cap zone, malachite is the chief oxidised Cu mineral, generally accompanied by chrysocolla, cuprite or native Cu, as well as some chalcocite which is hard to distinguish from the primary sulphide.

Outcrops near the ore horizon within the footwall arenites are limonite stained, but show no indication of leached primary sulphides. At surface the original discovery outcrop had minor, but not pronounced malachite staining. Although the main 'C' Ore Quartzite is followed by a stream, now filled with mine waste, there is little evidence of Cu mineralisation at surface apart from the carbonates at the 'Discovery Outcrop'. Patches of diffuse limonite staining are evident, within a sequence of weathered, pitted (after anhydrite) sandstones and argillite, with carbonate rich bands (with a white powdery appearance). In places the brown staining is more pronounced, reminiscent of weathered sulphide, although it is more likely that this is fall-out from the smelters. Figure 2.1 shows the general geology and its relationship to the orebodies.

2.4 DEPOSIT TYPE

2.4.1 The Ore Bodies

The Mufulira mine is comprised of three ore bodies, referred to as orebody A, B and C. Ore body A is the smallest of the three and stretches horizontally 300 m, orebody B is slightly larger and stretches horizontally 600 m, while orebody C is the main ore body, this mineralization is also mined in the mine in Mindola approximately 40 km south of Mufulira. But the ore body itself is limited by the cut-off grade of 1.5% to a horizontal stretch of 1400 metres and has been followed down to a depth of at least 2000 m. The ore body generally dips 45 degrees in the North East direction but at some places it flattens towards 35 degrees.

The ‘C’ orebody comprises mineralized grey quartzite, which is present throughout the mine area and is underlain by a mud seam. The ‘B’ orebody comprises mineralized grey sericitc quartzite. The ‘A’ horizon comprises a pink to dark grey feldspathic generally massive quartzite with some greywacke carbonaceous lenses. The orebody contact is generally distinct

in all the ore bodies; In C they have a mud seam, in B they have a clear-cut and the ore and host rock is pink respectively black, in A they also have a clear-cut with the pink quartzite against the grey argillite, but in the hanging wall the contact is not as clear. Table 1 summarizes the different orebody characteristics. The hanging-wall formation overlaying the ore bodies, mainly consists of the argillaceous and dolomites. These sediments indicate an evident change from the pre-dominantly arenaceous rocks of the Lower Roan Group to the Dolomite rocks of the Upper Roan Group (MOPANI, 2013b) (Sarpong, 2013).

2.5 GEOTECHNICAL CONDITIONS

The Mufulira rock mass generally consists of a sequence of strong sedimentary formations overlying competent basement Schist and Granites, with rock strengths that range from 200 to 300 MPa. The Mufulira orebodies generally dips on average 45 degrees to the Northeast, but flatter areas exist were the dip is 35 degrees. The three ore bodies are described in; stratigraphic units, thickness and general geotechnical competency. The rock mass below 500m level is by Copperbelt standards generally very strong. Due to this the mine experience brittle stress fractures and seismic activity in the areas below 500 m. In the enrichment zone above 500 m the problem concerns the effect of water in the rock mass (MOPANI, 2013b).

2.6 FOLDING

A special category of folds with flat or low-dipping axial planes exposed has been recognised in the Copperbelt mines and is in contrast with drag-folds with steeply dipping axial planes. A list of folds and their attitudes and some of the properties is given in Table 2.1. The flat or low dip of the axial planes of these 'flat' folds and the inversion of the middle limb, giving the latter generally a flat dip towards the south-west, necessitates an explanation by a nearly horizontal stress directed towards the north-east against the stable foreland of the Katangan geosyncline. Participation of the underlying Basement, including the competent Basement granite, in these overfolds indicates the strong tectonic stresses required to deform the relatively rigid granite and demonstrates that slide or slump phenomena are inadequate to explain these structures. These 'flat' folds as listed in Table 2.1 are regarded as related in tectonic age and may be an embryonic form of the major nappe structures of the Katanga province to the north-west. Three recumbent folds occur in Mufulira mine. One, to be described in detail, crops out on surface

and is presented on plan, vertical longitudinal projection, and in cross-sections. The axes of this fold plunge at an average of 10° to the north-west. The cross-section reveals apparently horizontal axial planes. The lateral amplitude is up to 122 m and the vertical distance between crest and trough is 46 to 90 m. The fold has been traced down the plunge of its axes for over 1,524 m, beyond which it gradually fades out. Schistosity, quartz veining, jointing and shearing are very irregular in both the sediments and the Basement granite involved in the fold. The granite core with its numerous xenoliths has locally been metamorphosed to biotitechlorite schist with considerable epidotisation. DeSwardt (1962) has suggested that later doming associated with the rise of the Kafue anticline has tilted these earlier inclined folds to a more recumbent attitude and those at Mutundu-Mutupa to a diving attitude. At the same time the doming would cause back-tilting of the same type of early inclined folds to a nearly vertical attitude as at Chambishi and Nkana on the south-west limb of the Kafue anticline

Table 2.1 List of common folds found on the Copperbelt province

Type of Fold	**Property**	**Plunge of Fold**	**Attitude of Axial Plane in Cross-section**
'Flat type' type	Chingola Pit	0^0-15^0 NW	Near horizontal
	Mufulira	0^0-20^0 NW	Near horizontal
	Mutundu South and Mutupa	Variable SE	Corrugated
	Ndola West	15^0 N to 15^0 S	30^0-50^0 W
'Drag' type	Chambishi	0^0-10^0 W	70^0 S
	Nkana	20^0-30^0 NW	Steeply S-W
	Roan Antelope	45^0 E to 80^0 W	70^0 NE
	Chibuluma West	0^0-15^0 W	80^0 S to 80^0 N

2.6.1 Relation between Folding and Mineralization

As observed from the vertical longitudinal projection, the top fold diverges from the upper fringe of the 'C' ore-body eastwards from 60 mining block. Recent development indicates that the bottom fold is also oblique to and intersects a limit of the 'C' ore-body, in this case the

western economic fringe against pyritic mineralization on the 2650 level. Likewise no enrichment or impoverishment of ore grade has been observed within the fold areas, except where the flat pod-folds cross structures associated with irregularities due to compaction folding over sub-Katanga palaeo-hills. These tectonic folds in Mufulira are thus in no way genetically related to the ore-bodies. In fact, the only influence noticeable is accentuated oxidation where the top fold intersects the upper fringe of the 'C' ore-body west of 60 mining block. Yet the folds manifestly distort all the bedded formations including the orebodies and have in places resulted in minor breaks, commonly filled with minerals appropriate to the adjacent wall rock. Consistency of stratiform mineralization through both the undistorted and the folded areas can only be ascribed to the tectonic folds post-dating mineralization.

2.7 GEOMECHANICS

Safety levels in the deep underground copper mining industry have improved. However, a lot more can be done to further reduce accident rates. During excavation design or shaft pillar stability assessment in-depth knowledge of the geological setting, petrography, rock mechanical behaviour and strength characteristics of rock material, place a rock engineer and a mining engineer in a better position to make safe and sound judgments (Bieniawski, 1974).
Mining engineers and rock engineers use many parameters to describe the properties of rocks, such as the uniaxial and triaxial strength, Young's modulus and the Poisson's ratio. It is well understood that a rock material is part of a complex rock mass (Bieniawski, 1974). Nonetheless, studies in deep African mines found that mechanical properties determined in the laboratory from small rock specimens provided valuable information about characteristics and behaviour of the rock mass (Ortlepp and Cook, 1960).

2.8 MICROSEISMIC MONITORING

2.8.1 Introduction to Microseismic Monitoring

A common way of determining instability and changing stress conditions in underground mines is to monitor mining-induced microseismic events. A microseismic event occurs when a rock under a critical amount of stress fractures and emits an energy wave of short duration and small amplitude (Obert and Duvall, 1967). Each waveform contains a grouping of elementary wave signals that represent particle velocity initiated by individual pulses of stress wave energy (Descour and Miller, 1987). The energy pulse’s shape details the amount of stress released at

the source and the effect of non-uniformities in the rockmass along its travel from the source to a microseismic sensor such as a geophone. The polarity of a waveform from both man-made and natural sources can be used to determine whether an event's driving force was shear or compressional (Swanson, Stewart, and Koontz, 2008). Individual waveforms are analyzed to determine the time, location, and magnitude of a single event. A seismic event with a moment magnitude of typically less than 2.0 is considered ‘‘micro" (Spence, Sipkin, and Choy, 1989). Over time, the failure process of a monitored area can be studied from the progression of the located events. At least three microseismic surveys have been completed and analyzed in longwall coal mines (Alber, Fritschen, Bischoff, and Meier, 2009; Ellenberger, Heasley, Swanson, and Mercier, 2001; Luo, Hatherly, and McKavanagh, 1998; Swanson et al., 2008). These studies and analyses verified that microseismic monitoring is a useful tool for understanding stress redistribution in an underground coal mine setting. In contrast, room and pillar retreat mines have had only one published microseismic study. This study, completed in 1987 by Descour and Miller, monitored various parts of a retreat mine section over a 10-month period. The mine layout however was not the same as what is currently found underground. Modern rectangular retreat panels, which incorporate five to seven entries encompassed by barrier pillars on both sides, were not employed. Instead, an entire section of the mine was extracted. Much smaller barrier pillars, approximately the size of 10 production pillars, were placed in vital areas of the section. Microseismic events are the results of changes in the stress distribution of a rockmass, where the physical event is a slip or shear of the rock. These events are too small to be felt on the surface of the earth but can be detected and measured by equipment such as geophones or accelerometers. This is considered a passive method as the instruments are monitoring seismic activity already taking place, also known as induced seismicity (ESG Solutions, 2016). This monitoring can provide results in real-time, providing knowledge of what is happening underground at exact points in time (Ge, 2005). Microseismic monitoring can reveal information such as when and where the microseismic event occurred underground, and the event's magnitude (Ge, 2005). The main goal of such monitoring is to observe these events over time and identify patterns and correlations between events and production activities. Monitoring seismic activity in mining operations can improve mine safety through risk management, and be used to study overall ground conditions.

2.8.2 Planning the Monitoring System

Efficient mine microseismic monitoring can be summarized in three aspects: monitoring planning, data processing, and event location (Ge, 2005). Thorough planning is essential for establishing an efficient and lasting monitoring system. In planning, it is important to assess monitoring objectives, including target areas, accuracy, and conditions of the area being monitored. The size of the monitoring system is another important aspect to the design. The degree to which a monitoring system is effective is proportional to its ability to pick up signals. Large channel systems, therefore, are the most effective as they can record more signals and a relatively higher number of signals due to the decrease in distance between potential event locations and sensors. Initial and regular calibrations should be conducted on the sensor array to ensure the most accurate data. As mining environments are very dynamic and potentially harsh on monitoring equipment, regular equipment and signal checks should be performed to allow for uninterrupted data collection.

2.8.3 Event Location and Processing

These microseismic events are detected in the form of an energy wave that travels from the point of origin outward through surrounding rock (ESG, 2016). The waves travel by elastic deformation of the rock medium, creating compressive and shear stresses. The types of waves that are monitored are called body waves. There are two types of body waves: P-waves, or primary waves, and S-waves, secondary waves. P-waves are fast traveling seismic waves, and move through a medium in the longitudinal direction by compression, pushing and pulling the material. S-waves are much slower and move through material causing vibrations perpendicular to the direction of the wave propagation, as opposed to parallel with P-waves. P-waves can move through solids and fluid, while S-waves can only travel through solids. Because P-waves travel faster, the greater the distance between the arrivals of the two waves, the greater the distance between the sensor and location of the microseismic event (ESG, 2016). The efficiency of a microseismic monitoring system is generally measured by the accuracy of event locations (Ge, 2005). A suitable source location code is necessary for a reliable monitoring system. There are many different approaches to source location, but in general there are four aspects that should be considered. First, the searching algorithm should have a good convergence character so that the divergence problem is less likely to occur and the system will not be interrupted. Second, is the ability to use P and S-wave arrivals simultaneously. This allows for better use of the data, as both arrivals are not always detectable, and provides a better

method for reducing error in source location. Third is the ability to limit the impact of errors, by array and data optimization. The least-squares and absolute-value methods are the most commonly used for defining the error. The fourth aspect necessary for an effective mine monitoring system is a reliability analysis of the source location result. In determining reliability, the residuals, sensitivity, and hit sequences are analyzed (Ge, 2005).

Processing microseismic data from a mine site is usually very complex. There are often large levels of background noise from the mining operation that interfere with microseismic signals. One of the primary tasks of data processing is the filtering of the background noise. If the frequency range for the signals is different from that of the background noise, frequency filters can be used to clear the background noise. Another important aspect of data processing is the identification of arrival types. First arrivals may be P-waves, S-waves, or outliers, which are arrivals not due to the physical source. If these arrivals are not properly identified, the database would contain many systematic errors (Ge, 2005).

2.8.4 Seismic Characteristics of Rock Failure and Mechanism Solutions

In-situ rock masses may fail in five different modes (Gale et al., 2001):

I) Shear fracture through intact rock.
II) Tensile fracture through intact rock.
III) Shear fracture of bedding planes.
IV) Tensile fracture of bedding.
V) Movement of pre-existing fractures.

The stress levels before a failure depend on the strength properties of the intact rock, and after the failure this stress is reduced to an amount dependent on the strength properties of the fractured material. The difference between these two stresses is known as the stress drop. Shear failures create much larger stress drops than tensile failures. Similarly, much more strain energy is released in shear failure than tensile failure (Gale et al., 2001). During monitoring, the direction of the P-wave can be used to differentiate between shear and tensile failure. Movement both towards and away from the source reflect shear failure, while P-wave motions moving toward the source at all sensors represents tensile failure (Swanson et al., 2008). When analysing the characteristics of seismic activity, focal mechanism solutions are used to display the mechanism of failure occurring in the rock. A focal mechanism solution is derived from analysing waveforms generated by seismic activity (Cronin, 2010). As seen in the graphic

created by the US Geological Survey (public domain), the focal mechanism is a spherical ball with two black quadrants and two white quadrants, also known as a beach ball. The full-circle arcs that divide the quadrants represent two nodal planes, one of which represents the plane on which the failure actually occurred. Local geologic knowledge is usually required to differentiate between the planes (Cronin, 2010). The colour of the quadrants represents the movement of material during the failure (USGS, 2016). Material moves in the direction toward the dark quadrant from the white quadrant, meaning compression towards dark quadrants and tension away from the white

2.9 ROUTINE MICRO-SEISMIC MONITORING IN MINES

2.9.1 Introduction

Routine seismic monitoring in mines enables the quantification of exposure to seismicity and provides a logical tool to guide the effort into the prevention and control of and alerts to, potential rock mass instabilities that could result in rock bursts. One can define the following five specific objectives of monitoring the seismic response of the rock mass to mining: rescue of personnel, prevention, seismic hazard rating, alerts- including short term response to unexpected strong changes in certain parameters, and back analysis to improve the efficiency of both the mine layout design and the monitoring process. A quantitative description of seismic events and of seismicity are necessary but not sufficient in achieving the above objectives. The basis of a modern digital seismic technology and seismological parameters used to quantify seismic sources and seismicity for seismic hazard assessment and rock mass stability analysis has been described.

2.9.2 Objectives of Seismic Monitoring in Mines

In general, routine seismic monitoring enables the quantification of exposure to seismicity and provides a logistical tool to guide the effort into prevention, rating of seismic hazards and alerts to potential rock mass instabilities that could result in rock bursts in underground mines (Mendecki, 1997b) and slope instabilities in open pit mines (Lynch et al., 2005). One can define the following five specific objectives of monitoring the seismic response of the rock mass to mining (Mendecki et al., 1999).

1) Rescue. To detect and locate potentially damaging seismic events, to alert management and to assist in rescue operations.

2) Prevention. To compare the observed and the expected seismic rock mass response to mining. To confirm the rock mass stability related assumptions made during the design process and enable an audit of, and corrections to, the particulars of a given design while mining.
3) Seismic hazard rating. To quantify the exposure to seismicity and to monitor its spatial and temporal changes. To classify the observed spatial and temporal seismic patterns into an agreed seismic hazard system.
4) Alerts. To detect strong and unexpected changes in the spatial and/or temporal behaviour of seismic parameters that could lead to instability, affecting working places immediately or in the short term.
5) Back analysis. To improve both the mine design and seismic monitoring processes. Particularly important is thorough and objective back analysis of larger rock mass instabilities even if they did not result in injuries, loss of life or damage. Back analysis should form the basis for a regular critical review of the applied seismic risk management strategy, guidelines and procedures.

A quantitative description of seismic events and seismicity is considered the minimum requirement to achieve the above objective.

2.9.3 Importance of Location

The location of a seismic event is assumed to be a point within the seismic source that triggered the set of seismic sites used to locate it. The complexity of processes at the source, however, may complicate the location of a seismic event. If a slow or weak rupture starts at a certain point, the closest site(s) may record waves radiated from that very point while others may only record waves generated later in the rupture process by a higher stress drop patch of the same source. One needs to be specific in determining the arrival times of different phases if the location of rupture initiation is sought, otherwise the location will be a statistical average of different parts of the same source. A reasonably accurate location is important for the following reasons:

a) To indicate the location of potential rock bursts.
b) All subsequent seismological processing e.g. quantification of seismic sources, attenuation or velocity inversion, depends on location.

c) All subsequent interpretation of individual events depends on location e.g. events far from active mining, close to a shaft or, in general, in places not predicted by numerical modelling, may raise concerns.
d) All subsequent interpretations of seismicity, e.g. clustering and specifically localization around planes, migration, spatiotemporal gradients of seismic parameters and other patterns are judged by their location and timing.

Since the source of a seismic event has a finite size, the attainable location accuracy of all seismic events in a given area should be within the typical size of an event of that magnitude which defines the sensitivity of the seismic network for that area, i.e. the minimum magnitude, m_{min}, above which the system records all events with sufficient signal to noise ratio.

2.9.4 Quantification of Seismic Sources

A seismic event is considered to be described quantitatively when apart from its timing, t, and location, X = (x; y; z), at least two independent parameters pertaining to the seismic source namely, seismic potency, P, which measures co-seismic inelastic deformation at the source and radiated seismic energy, E, are determined reliably.

2.9.4.1 Seismic potency

Seismic potency (P), represents the volume of rock, of whatever shape, associated with co-seismic inelastic deformation at the source (Ben-Menahem and Singh, 1981, King, 1978). The scalar seismic potency is the product of the strain change and the source volume

$$\mathbf{P = \Delta \epsilon V} \qquad \textbf{(2.1)}$$

Where

$\mathbf{\Delta \epsilon}$ is change in strain

V is the source volume

For a planar shear source, the potency is defined as **P = uA**

Where

A is the source area [m^2]

u is the average slip [m]

At the source, seismic potency is the integral of the source time function over the duration. At the recording site potency is proportional to the integral of the P or S-wave displacement pulse corrected for the far-field radiation pattern $u_{corr}(t)$

$$\mathbf{P_{P,S} = 4\pi \upsilon_{P,S} R \int_0^{ts} u_{corr}(t)\, dt,} \qquad \textbf{(2.2)}$$

Where

$\boldsymbol{\upsilon}_{P,S}$ is P or S-wave velocity,

R distance from the source,

$\mathbf{t}_s$ is source duration

$u(0) = 0$ and $u(t_s) = 0$.

It is most frequently estimated in frequency domain from the amplitude of the low frequency displacement spectra Ω_0 of the recorded waveforms (Keilis-Borok, 1959)

$$\mathbf{P_{P,S}} = \mathbf{4\pi\upsilon_{P,S}R\frac{\Omega 0p,s}{\Lambda p,s}} \qquad \textbf{(2.3)}$$

Where

$\Lambda_{P,S}$ is the root-mean-square value for the radiation pattern of farfield amplitudes averaged over the focal sphere

$\Lambda P = 0.516$ for P-wave and $\Lambda S = 0.632$ for S-wave (Aki and Richards, 2002).

2.9.4.2 Seismic energy

The energy released during fracture and frictional sliding is due to the transformation of elastic strain into inelastic strain. This transformation may occur at different rates ranging from slow creep-like events to very fast dynamic seismic events with an average velocity of deformation at the source of up to a few meters per second. Slow type events have a long time duration at the source and thus radiate predominantly lower frequency waves, as opposed to dynamic sources of the same size. Since excitation of seismic energy can be represented in terms of temporal derivatives of the source function one may infer that a slower source process implies less seismic radiation. In terms of fracture mechanics, the slower the rupture velocity, the less energy is radiated; the quasi-static rupture would radiate practically no energy. In time domain the radiated seismic energy of the P or S-wave is proportional to the integral of the radiation pattern corrected far-field velocity pulse squared $\mathring{u}^2(t)$ of duration t_S,

$$\mathbf{E_{P,S}} = \mathbf{\frac{8}{5}\pi\rho\upsilon_{P,S}R^2\int_0^{ts}\mathring{u}^2_{corr}(t)dt} \qquad \textbf{(2.4)}$$

Where

$\boldsymbol{\rho}$ is rock density

$\boldsymbol{\upsilon}_{P,S}$ is S or P-wave velocity

R is the distance from the source

In the far field of seismic observations the P and S-wave contribution to the total radiated energy are proportional to the integral of the square of the P and S velocity spectrum. For a reasonable signal to noise ratio in the bandwidth of frequencies available on both sides of the dominant (corner) frequency $\mathbf{f}_0$, the determination of that integral from waveforms recorded by seismic network is fairly objective. The high frequency component of seismic radiation needs to be recorded by the seismic system if a meaningful insight into the stress regime at the source is to be gain.

2.9.4.3 Apparent stress

The apparent stress σ_A is defined as the ratio of the radiated seismic energy E to potency (P) It measures the amount of radiated seismic energy per unit volume of inelastic deformation at source (Aki, 1966; Wyss and Brune, 1968).

$$\mathbf{O_A = \frac{E}{P}} \qquad \textbf{(2.5)}$$

Where

$\mathbf{O_A}$ is the apparent stress

E is the seismic energy

P is the potency

2.10 ACOUSTIC EMISSION INTELLIGENT REAL-TIME MONITORING SYSTEM

The acoustic emission intelligent real-time monitoring system named YSFS (A) for mine dynamic disasters, independently developed by China Coal Technology Engineering Group Chongqing Research Institute, is a multi-channel parallel intelligent real-time monitoring and early warning system that the surface and the underground intersect each other, which is mainly composed of underground acoustic emission monitoring host, power supply, serial sensors, special signal shielded cables and ground real-time processing analysis software as shown in Figure 2.2.

The system processes the massive acoustic emission signals collected by the acoustic emission sensors in situ by the underground acoustic emission monitoring host, and then the processing results are transmitted to the upper computer on the ground through the safety monitoring industrial network, so as to realize the real-time and advanced monitoring and early warning

for the coal-rock dynamic disasters in the working face, effectively overcoming the shortcomings of the traditional prediction methods, such as point prediction, large quantities of work, and many human factors. It has the advantages of high accuracy of disaster prediction, wide field application experience, strong underground applicability, high degree of automation, low cost of use and maintenance. The technology and system are mainly used for monitoring and warning for coal and gas outburst, rock burst and other mine dynamic disasters, and also for monitoring the stability of roadways, tunnels and geotechnical slopes.

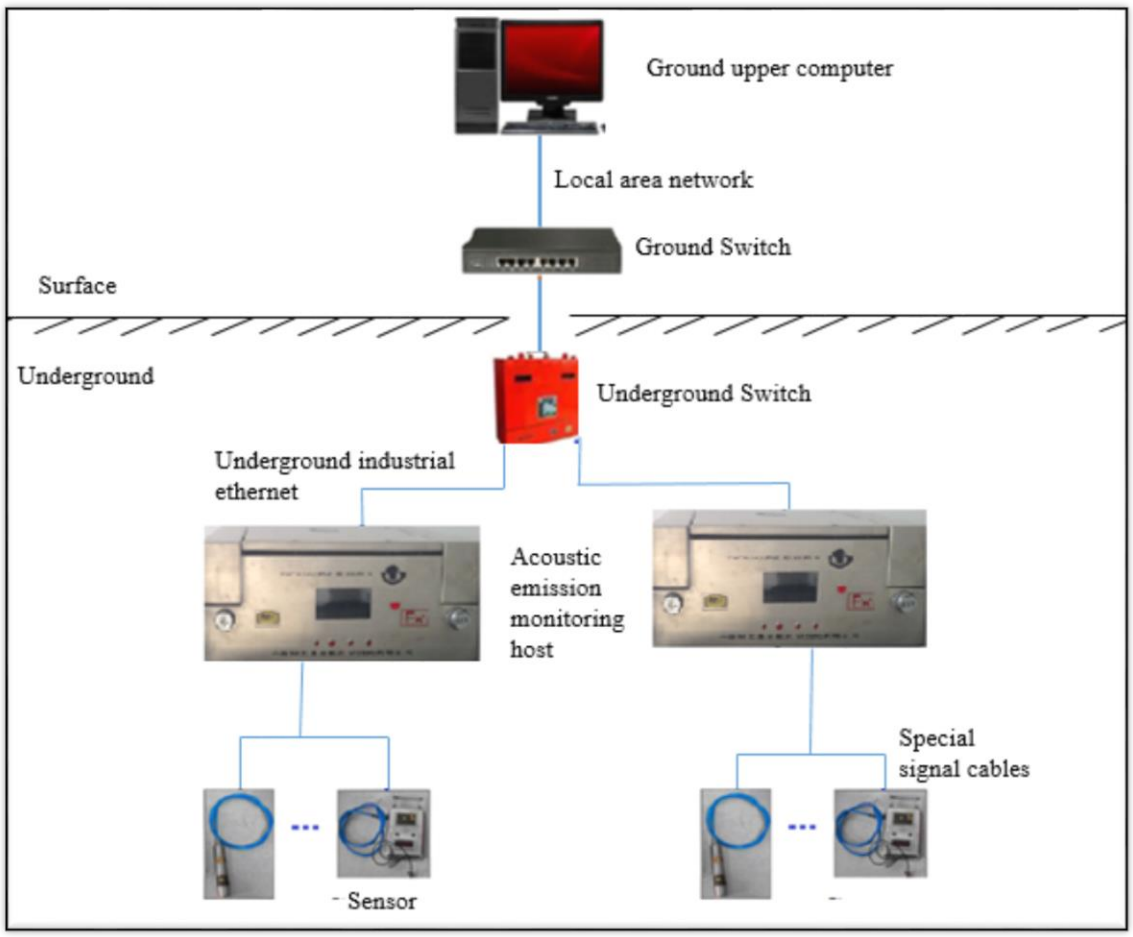

Figure 2. 2. Schematic diagram of acoustic emission monitoring system named YSFs (A)

The main technical parameters of the acoustic emission monitoring system are as follows;

(1) Underground monitoring host

The underground monitoring host realizes multi-channel parallel signal acquisition, data pre-processing, communication, working status display and alarm,

a) Working voltage: 660 V,

b) Monitoring host capacity: 8-channel acoustic emission signals and 4-channel analog signals such as gas and stress are collected synchronously in parallel,

c) Sampling rate: up to 51.2 KS/s per channel, optional,

d) Sampling accuracy: 24 bit,

e) Real time data analysis speed: FPGA hardware level high-speed data processing,

f) Explosion proof type: mine intrinsic safety type.

(2) A series of acoustic emission sensors

a) Installation mode: according to different monitoring environment, there are various installation modes such as waveguide installation and hole bottom installation,

b) Working voltage: 12~18 V,

c) Working current: ≤ 70 mA,

d) Measurement range: 0~1 g,

e) Output range: 1~5 mA,

f) Band width: 0~3000 Hz,

g) Effective transmission distance from signal to monitoring host: no less than 2 km.

(3) Ground real-time processing analysis software

a) The system realizes the all-weather real-time monitoring and early warning of coal-rock dynamic disasters with multi-channel parallel intersection between the ground and the underground.

b) The full waveform, characteristic parameters and alarm results of the signals collected by all channels are dynamically displayed and stored on the ground upper computer in real time.

c) The instruction configuration for monitoring host is remotely carried out, including attribute setting, data export and different signal acquisition mode settings.

d) The independent database is owned, which can be used for data query and report printing.

2.11 ACOUSTIC EMISSION MONITORING METHOD AND TECHNOLOGY

2.11.1 Monitoring Method

Through the installation of acoustic emission sensors in advance, the acoustic emission monitoring system is used to continuously monitor the work face, real-time collect and analyse

the acoustic emission signals inside the coal and rock mass, to obtain the change rule, trend and disaster precursor characteristics of the acoustic emission indexes, and continuous monitoring and real-time early warning for the coal-rock dynamic disasters in the work face.

2.11.2 Installation Technology of Acoustic Emission Sensors

The installation effect of acoustic emission sensors directly affects the ability of receiving acoustic emission signals and the effect of noise barrier. According to different monitoring objects and monitoring environment, the sensors can be installed in the way of waveguide installation and hole bottom installation. The waveguide installation method is to use the guided wave function of waveguide, fix the inner end with the coal and rock mass at the bottom of the hole through the elastic materials after solidification, install the acoustic emission sensors at the outer end, and transmit the signals to the sensors through waveguide. The waveguide installation method is convenient and recyclable, which is suitable for use in the space environment with less noise interference from external operation, as shown in Figure 2.3 (A). For the hole bottom installation method, the acoustic emission sensors are coupling installed in the coal and rock mass at the hole bottom through constructing a certain depth of drilling by cement mortar, and the noise isolation treatment of the hole opening can largely isolate the external interference noise. The hole bottom installation method has the advantages of strong signal receiving ability and strong anti-interference ability, as shown in Figure 2.3 (B)

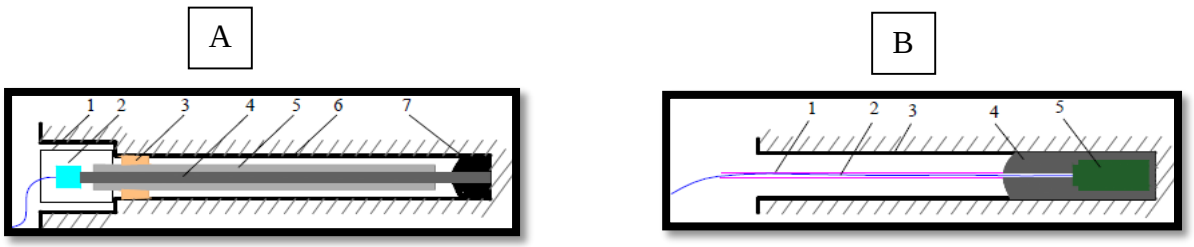

1. Sensor sleeve
2. Sensor
3. Wood wedge
4. Waveguide
5. Waveguide sleeve
6. Drill hole

1. Rubber hose
2. Signal line
3. Drill hole
4. Cement mortar
5. Sensor

Figure 2.3: ***(A) The waveguide installation method, (B) The hole bottom installation method***

For the longwall working face: one acoustic emission sensor should be respectively installed in advance at the place 50 m away from the front of the working face in the machine roadway and wind roadway of the working face, and the acoustic emission sensors should be installed in advance with the mining of the working face in a monitoring cycle of 30 m.
For the excavation working face: one acoustic emission sensor should be installed in advance in front of the working face. With the excavation of the working face, the acoustic emission sensors should be installed in advance in a monitoring cycle of 20~30 m.

2.11.3 The Acoustic Emission Monitoring and Early Warning Indexes

The acoustic emission signal is a kind of pulse waveform signal with many characteristic parameters, such as ring count, energy, amplitude, signal duration. Through a large number of field application research, it is found that the combination of acoustic emission ring count and energy two characteristic parameters can effectively predict the rock dynamic disasters in the working face. The activity of coal and rock in working face can be analysed by the change of ring count, and the energy release in the process of coal and rock mass activity can be analysed by the change of energy index.

2.12 SUMMARY

This chapter reviewed literature that highlighted mining method techniques that are used at Mufulira mine. It also reviewed the geological setting and economical potential in terms copper ore mineralisation at the mine. The use of Micro-seismic monitoring system techniques in deep mines were also reviewed and an early warning system of acoustic intelligent gives a brief overview on the use of Micro-seismic monitoring system in deep mines as well as other possible early warning systems such acoustic emission intelligent real-time monitoring system were studied. The next chapter highlights the methods used to carry out the research.

CHAPTER THREE: METHODOLOGY

3.1 Introduction

This chapter highlights different methods used during data collection which involved field trips to conduct both geological and geotechnical mapping. It also presents all the objectives followed in achieving the intended purpose for research work. For the successful completion of this research, secondary and primary information was collected. Careful effort was made to collect secondary data that is representative of the study area. Primary data was collected through sampling, mapping, geological and geotechnical logging.

3. 3 Primary/ Field Data Collection

All sampling, geophone installation and structural geological and geotechnical mapping were conducted, during which underground trips were conducted at Mufulira mine DEEPS section.

3. 2 Secondary Data Collection

Secondary data was collected to better understand the mining methods being used, geology and hydrogeology of the study area. This information also assisted in the development of a conceptual and numerical model. Publications on studies completed around the Mufulira mine related to this research were reviewed as a source of secondary data. Information on the study area was acquired from Mopani Copper Mines (MCM) technical department by issuing questionnaires to key personnel such as mine chief surveyor, geology superintendent and senior rock mechanics engineer.

3 .4 Sub-Objective 1: To review previous and existing mining methods in terms of development, stope dimensioning, extraction practices and sequences

The above objective was achieved through extensive review of the available literature on the mining methods at the mine and consultation of critical personnel from key mine sections such as mine planning, survey and rock mechanics. Additionally, field trips were conducted to physically confirm stope dimensions, stope blasting and mining sequencing techniques used. Stope dimensions were assessed using distometer gadgets, stope blasting sequence was confirmed by physically accompanying the mine blasters and observe how they were conducting the exercise and made sure that right quantities of explosives were used during stope charging to avoid stope overbreaks which can also trigger seismic activities. The mining sequence techniques were checked through underground trips to seismically active mining

blocks to confirm if seismic activities had any negative impacts on the mining sequences being used at the mine. Mine lay outs were also studied to check if any design changes were made to safely mine within the seismic active mining blocks.

Following the severe damage of the mining drive and the cross-cut at 1490 mL that occurred on 06th February 2020, a review on the mining method previously proposed to de-stress the historical remnants between 62 and 64 blocks (Figure 3.1) was done as shown in Figure 3.2 and the option to de-stress the remnant was arrived at.

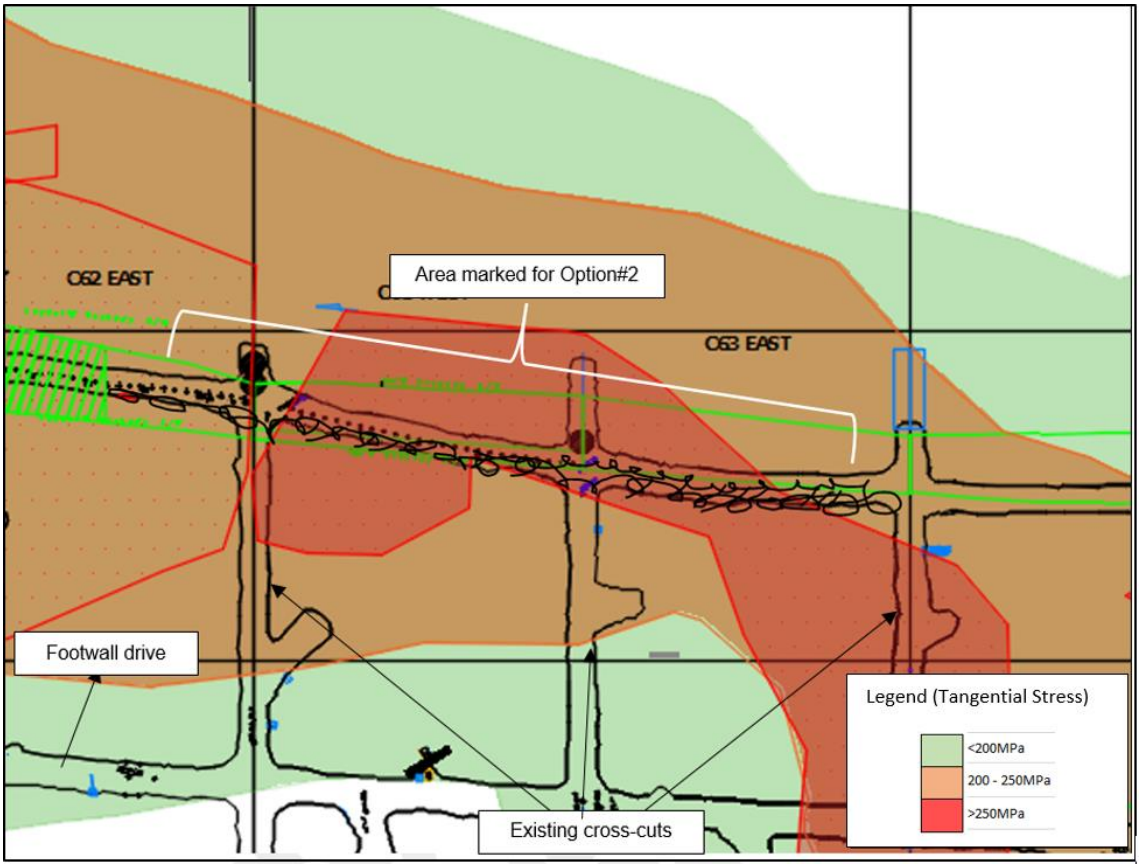

Figure 3.1 Shows 1473mL plan with location marked option 2 (Area located in high stress zones)

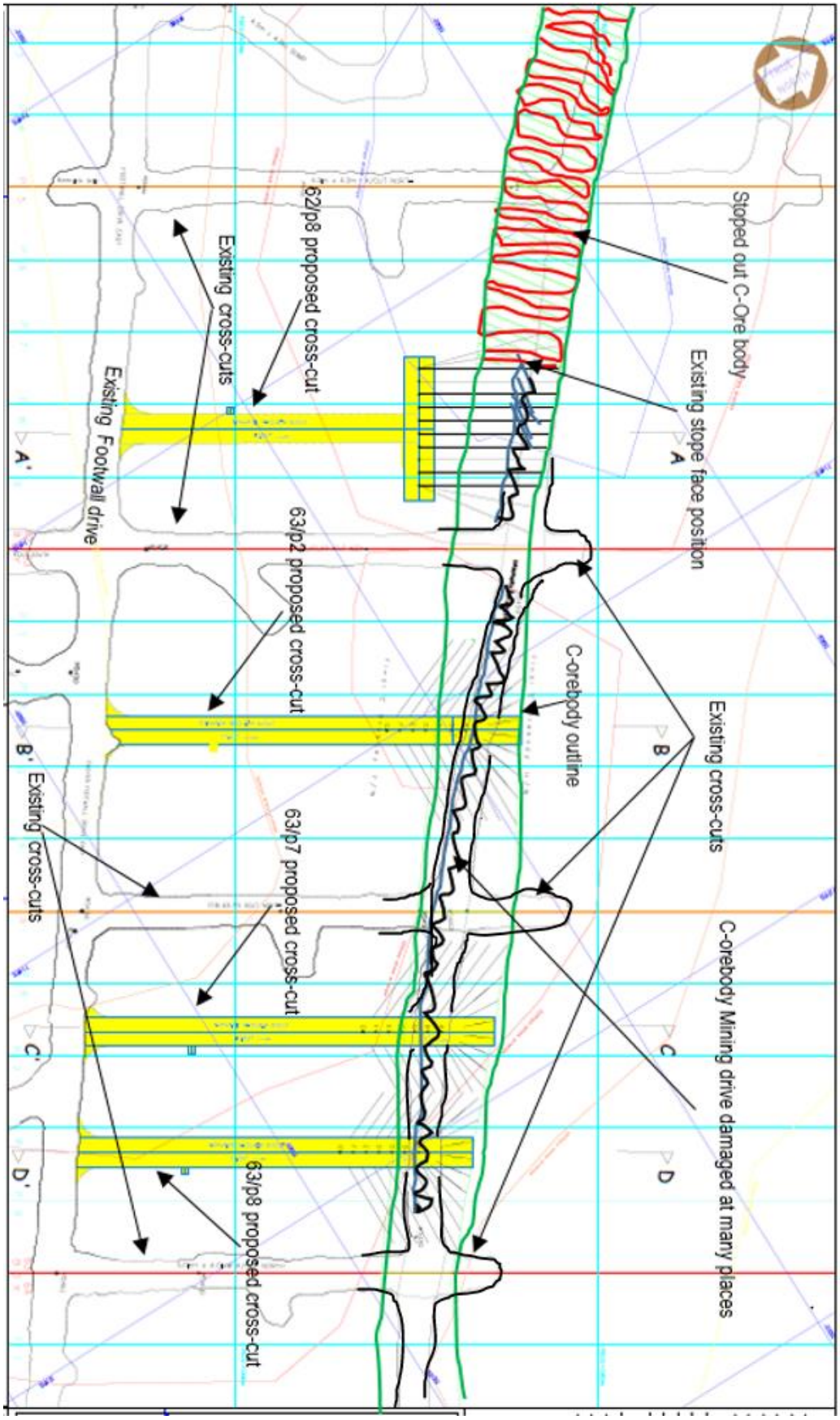

Figure 3.2 Showing 1473 mL plan on the lay-out (landscape)

3.5 Sub-Objective 2: To assess the ground condition in seismically active mining blocks.

Diamond drilled thirty four (34) NQ core samples were collected (Figure. 3.3), geotechnical core logging was conducted at the core yard, the core samples were collected and taken to the University of Zambia laboratory for geotechnical laboratory testing.

Figure 3.3 Showing (A) Core being drilled at an underground diamond drilling site, (B) Core samples packed for transportation, (C) Core samples being cut to 14 cm long size, (D) NQ size core samples and (E) Core samples packed in plastics for laboratory analysis

The following geomechanical tests were carried out;

(i) Brazillian test

(ii) Uniaxial Compressive Strength test

(iii) Triaxial Compressive Strength test

3.5.1 Brazillian test

Brazilian test was used to measure the indirect tensile strength of twenty-eight (28) NQ disc rock samples which were obtained by cutting a 14 cm core sample into small discs. A Digimax Compact line machine of 100 kN was used to carry out the test (Figure. 3.4) and pre-load was applied to all the specimens, average range was 80 – 90 N. Each 14 cm long NQ core size sample was divided into smaller discs of 27 mm long, half the diameter of the core sample which was 54 mm. Each disc was then weighed on the digital mass scale to get its mass, the digital vernier caliper was used to measure both the diameter and thickness of discs.

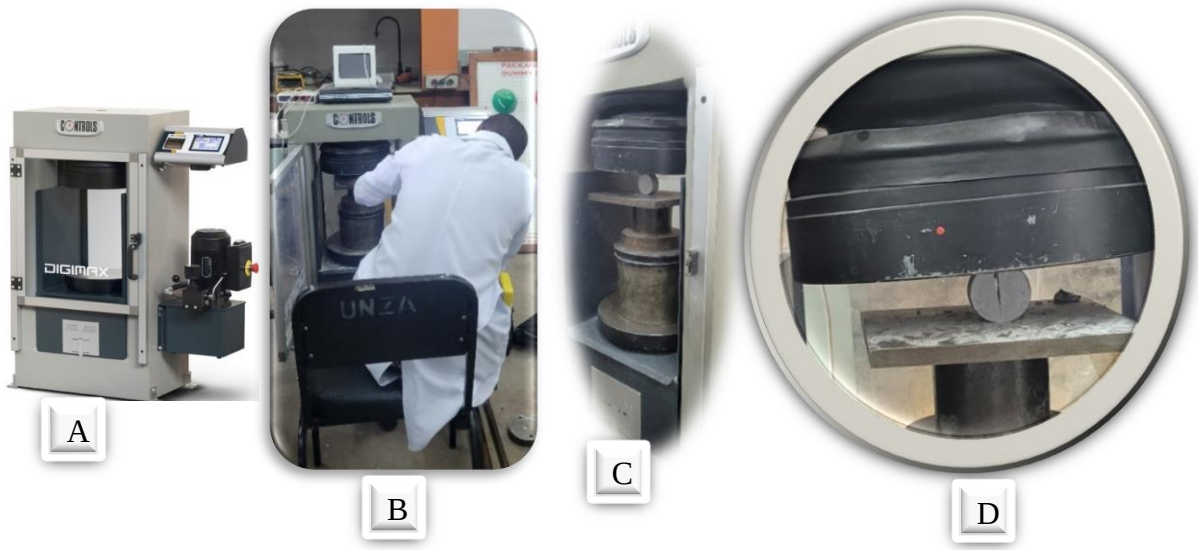

Figure 3.4: (A) Digimax Compact line machine, (B) Core disc placement between compression platens, (C) Core disc sample being subjected to constant load, (D) Core disc getting deformed.

Each disc was placed under the two platens and subjected to constant load as shown in Figure 3.4 (C), at a given maximum load, deformation of the disc occurs (Figure 3.4 (D)) and the tensile strength results were recorded.

Then the following formulae were used to find stress at failure;

$$\sigma_1 = \frac{6P}{\pi Dt}\ ;\ \sigma_2 = 0;\ \sigma_3 = -\frac{2P}{\pi Dt} \qquad (3.1)$$

The tensile strength, T_o, is given by the value of σ_3 (= $-T_o$) at failure

$$T_o = \frac{2P}{\pi Dt} \qquad (3.2)$$

Where

P is the applied load

D is the core diameter

t is the core thickness

3.5.2 Uniaxial Compressive Strength test

3.5.2.1 Sample preparations

Drilled core samples of diameter 47 mm (NQ) size were prepared according to the International Society of Rock Mechanics (ISRM) standard. The length of each sample was 140mm and 47 mm in diameter. The (L/D) ratio was 2.97 as per ISRM standard (1979). The cylindrical surfaces were prepared in order to be flat and smooth, leveled within 0.02 mm tolerance and made sure that not more than 0.06 degrees departure from perpendicularity occurred during the laboratory testing.

3.5.2.2 Apparatus

The apparatus used (Figure 3.5) to conduct the experiment consisted of the following:

1) Loading Device
2) Platens
3) Strain measurement devices (electrical resistance strain gauges).

3.5.2.3 Testing procedure

The two plates were carefully cleaned before the specimen was placed in the testing chamber. The load was continuously applied at a rate of 1.0 MPa/s and failures occurred in

Figure 3.5 (A) setting up of an experiment, (B) Placing the sample on the platens of the testing chamber, connecting strain gauges to the core sample (C-Axial strain gauge and D-Radial strain gauge)

approximately 10 minutes. Stress and deformation data were recorded through an electronic system that has the appropriate accuracy specifications. The maximum load was recorded in Newtons within a 1% accuracy and results were recorded.

The following formulae were used to find axial strain, diametric strain and compressive stress.

The axial strain is calculated as:

$$\varepsilon_a = \Delta l / L_0 \quad (3.3)$$

Where

ε_a is the axial strain

Δl is the change in measured axial length

L_0 is the initial length of the sample.

The diametric strain is calculated as:

$$\varepsilon_d = \Delta_d / D_0 \quad (3.4)$$

Where

ε_d is the Diametric strain

Δd is the change in diameter

D_0 is the initial diameter of the sample.

The compressive stress is calculated as:

$$\sigma = P / A_0 \quad (3.5)$$

Where

σ is the compressive Stress,

P is the load

$\mathbf{A_0}$ is the initial cross-section area of the specimen.

Therefore, the unconfined compressive strength was calculated for the maximum load applied:

$$\sigma_{UCS} = P_{max} / A_0 \quad (3.6)$$

The modulus of elasticity (Young's modulus) E which represents the ratio between axial stress and axial strain can be derived via several methods. It was calculated at stress-strain level of about 50% of the maximum load.

$$E = \Delta_\sigma / \Delta\varepsilon_a \text{ (At 50\% of maximum load)} \quad (3.7)$$

The *Poisson's ratio* that represents the ratio between diametric and axial strain, was calculated as:

$$n = - (\varepsilon_d / \varepsilon_a) \quad (3.8)$$

3.5.3 Triaxial Compressive Strength Test

3.5.3.1 Sample preparation

Drilled core samples were selected to be representative of the rock formation examined. The diameter of the samples was 47 mm and of 140 mm in length. The diameter was derived by taking measurements at the top, mid and the bottom parts of the specimen with a tolerance of 0.1 millimeters.

The height to diameter (H/D) ratio was 2.97 within the ISRM standard (1979) of between 2.0 to 3.0. The height was determined to the nearest millimeter. The ends of the samples were smoothed so that the top and bottom surfaces were flat with a tolerance of ±0.01 mm. This ensured that the applied loads are uniformly transmitted to the sample and there was no loading eccentricity. The lateral sides of the specimen were smooth and not present irregularities within 0.3 mm tolerance.

3.5.3.2 Testing procedure

A cylindrical rock specimen was placed in a specifically designed cell (Hoek cell) (Figure 3.6). A specially designed membrane was attached to the cell so that it remained airtight.

The lateral pressure is hydrostatic and was applied through a liquid (oil) which was pumped into the membrane. A hydraulic pump or a servomotor capable of regulating pressure within 1% accuracy was utilized. The specimen was axially enclosed by steel spherical seats. To derive the vertical and circumferential deformation of the sample, strain gauges were used and results were recorded.

Figure 3.6. (A) Hoek Cell containing core sample undergoing triaxial compressive test process (B) Deformed core sample after the test

3.6 Sub-Objective 3: To conduct rock and rock mass structural analysis using geological methods such as discontinuity and lithological mapping and drilled core logging in seismically active mining blocks

Field trips to seismically active mining blocks were carried out, detailed geological mapping, lithological core logging (Figure 3.7A), collection of hand-sized geological samples was done and thin sections prepared and microscopic analysis was carried out at the University of Zambia laboratory. During the mapping exercise structures such as folds (Figure 3.7C) and core discing (Figure 3.7B) were mapped. ArcGIS software was used to digitize the geological map of the study area. Mapping of structural discontinuities underground was also conducted, plotting and analysis of data was done using 3D Surpac modelling, Unwedge and Rick Allmendinger Stereonet software (Figure 3.7C).

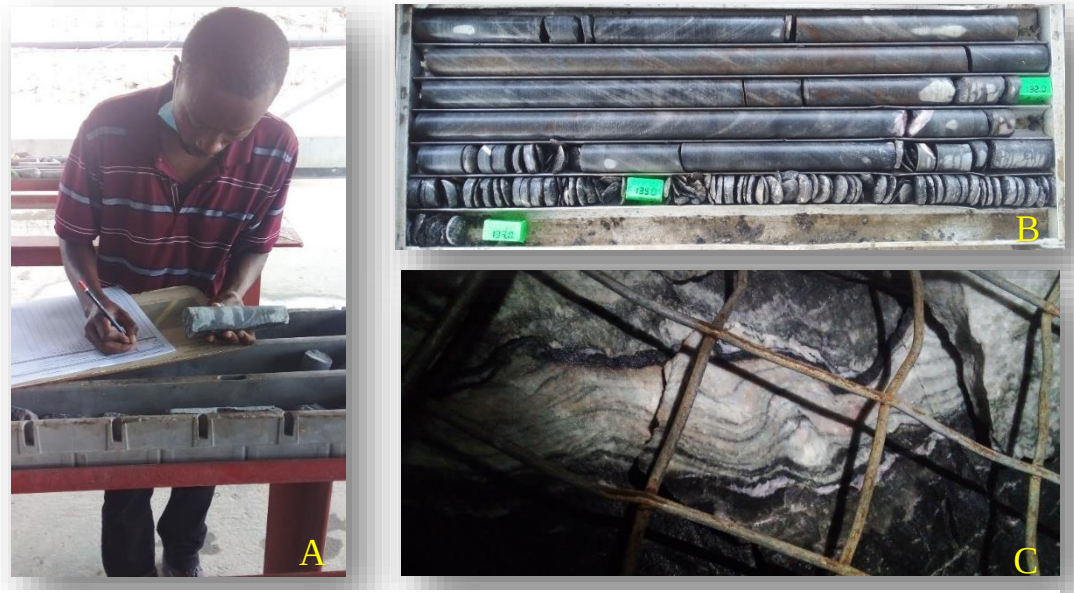

Figure 3.7. (A) Lithological core logging, (B) discing core samples drilled from highly stressed zone and (C) underground rock structural folding & jointing

3.7 Sub-Objective 4: To develop an early warning system that can predict rockbursts and rock induced displacements in seismically active mining blocks at Mufulira mine.

In order to develop an early warning system capable of predicting rock bursts and rock induced displacements, it is essential to understand the mechanical properties of the rocks found at Mufulira mine DEEPS section. The development of an early warning system will be done after addressing the sub-objectives 1, 2 and 3. In order to modify the already existing seismic monitoring system, two geophones will be installed at 1473 mL. The first one will be installed at 64P5 and the second one at 67P5. These geophones will be interconnect together using optical fibre junction box to the network switch and seismic events will be recorded.

3.7.1 Geophone Installation

At 1473 mL, geophone installation was conducted in the roof of the hanging wall (Figure 3.9) layout procedure and the following steps were followed;

(a) A hole of 10 metres deep and 76 millimetres diameter was drilled in the hanging wall see Figure 3.8

(b) The survey team picked the coordinates and marked the north/south directional line.

(c) The geophone was installed facing north/south direction.

(d) Grouting was done immediately after the installation was completed.

(e) The sensor cable from the geophone was connected to the seismometer box through the seismic sensor junction boxes.

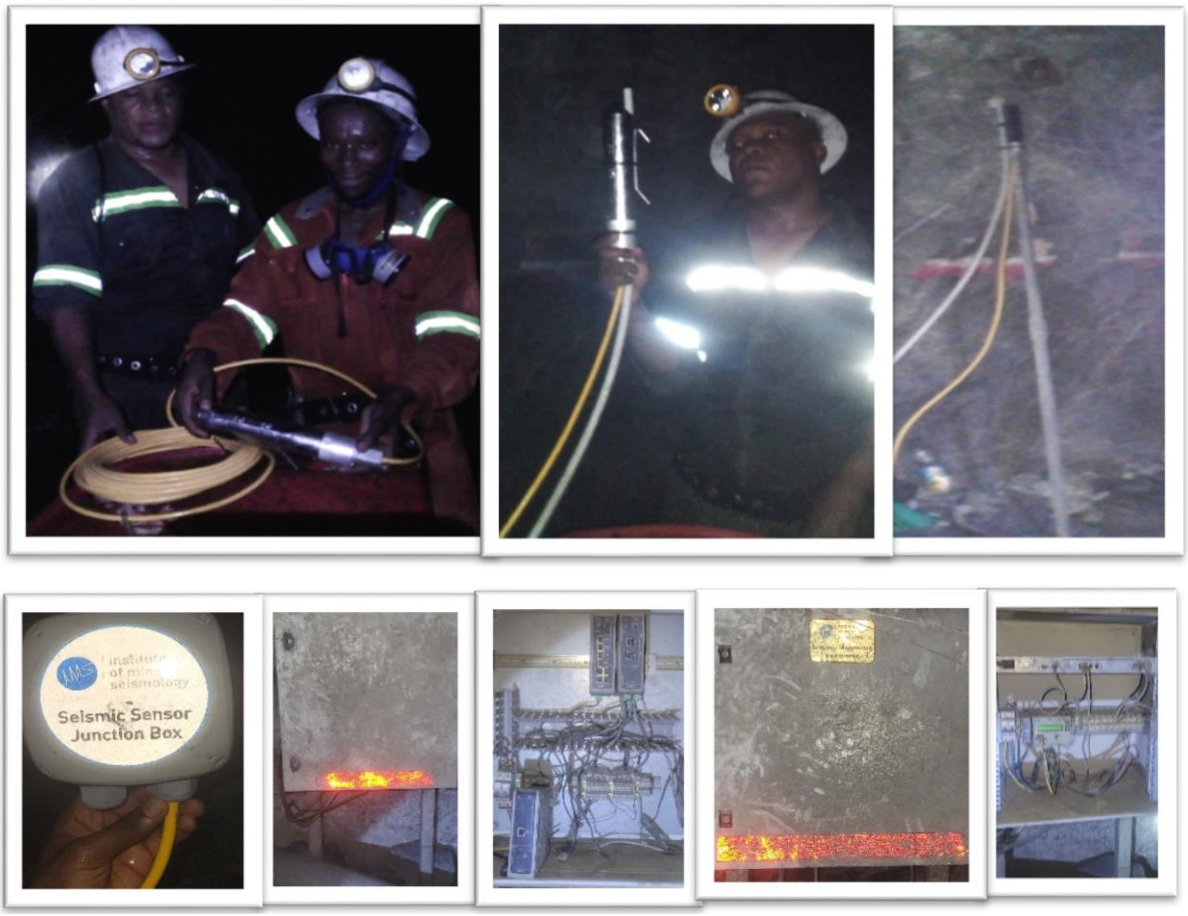

Figure 3.8 Showing the installation of the geophone at 67P5 south, 1473mL in the roof of hanging hall and the entire seismic boxes connections

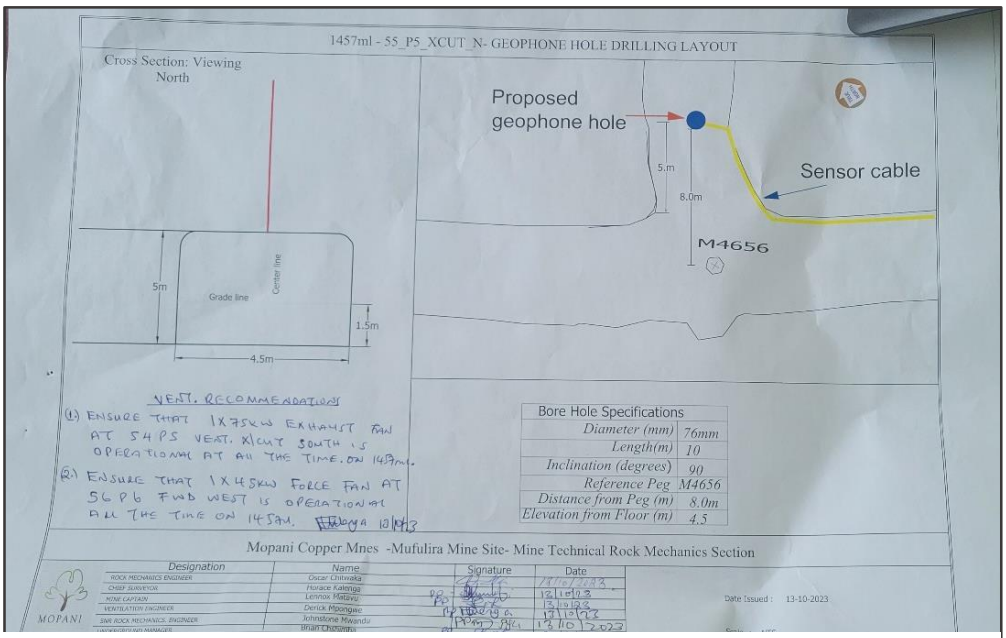

***Figure 3.9* Showing signed layout for geophone drill hole procedure at 1473 mL, 64P5**

3.8 Summary

This Chapter described the quantitative and qualitative methods that were used in carrying out the research. Careful effort was made to collect secondary data that is representative of the study area. Primary data was collected through sampling, mapping, geological and geotechnical logging. Interviews were also carried out in form of questionnaires that were given to critical mining head of departments with key informants, underground trips were undertaken and desktop research study conducted. The next chapter discusses the results obtained from the research using the methodology outlined in this chapter.

CHAPTER FOUR: RESULTS AND DISCUSSIONS

4.1 INTRODUCTION

In this chapter, results obtained by carrying out the objectives are presented, analysed and discussed. The results will be shown inform of tables, graphs, flow-charts as well as figures. This chapter documents the research findings from case study of Mufulira underground mine (DEEPS SECTION), during the quest for an early warning system capable of detecting rockbursts and rockfalls within the DEEPS SECTION. The characteristic properties of the rocks found at the mine are also discussed based on the Brazilian, Uniaxial and Triaxial test results obtained from laboratory experiments. The chapter further outlines the benefits of incorporating geomechanical properties of the rocks found at the mine so that their nature of deformation is well understood.

4.2 REVIEW ON PREVIOUS AND EXISTING MINING METHODS

Following the severe damage of the mining drive and the cross-cut on 1490 mL that occurred on 06th February 2020, a review on the mining method previously proposed to de-stress the historical remnants between 62 and 64 blocks was done. Additional cross cuts were developed to de-stress the area. Each cross-cut was designed and developed at 10 m apart. All the mining activities occurring in the seismically active mining blocks are employing sophisticated technology such as remote loaders to avoid loss of life or injuries and machine damage from rock bursts and rock falls.

The decision arrived at entails the development of additional cross-cuts inclined at 7% on average between existing cross-cuts to attempt to hole into the suspected void just above the existing mining drive where long blastholes for de-stress and production purposes will be drilled from as shown in Figure 4.1.

The initial plan to de-stress through long blastholes that would be drilled from the drive proposed to be placed on the hangingwall side of the C-orebody was therefore abandoned. The initial plan though presumed to be more effective and safer, could not be approved on time due to costs involved and required more mine development metres and consequently more ground support to be installed. Duration of implementation of the method to de-stress was a critical success factor of the de-stress plan as the targeted excavations were intended to be relieved of higher loading conditions quickly while they were still containing the existing rockmass

deformation. From the detailed reviews, it was presumed that the longer it took to implement the plan, the more severe the excavation damage got and the more vulnerable to collapse the excavation became. This contributed to the many factors that eventually resulted into the intensification of the damage of the 62E mining drive and the 62/P5 North cross-cut on 1490 mL. A method therefore, that would be quicker and consequently preserve the conditions of the existing excavations in the affected zone was found in option two and every excavation made was shotcreted.

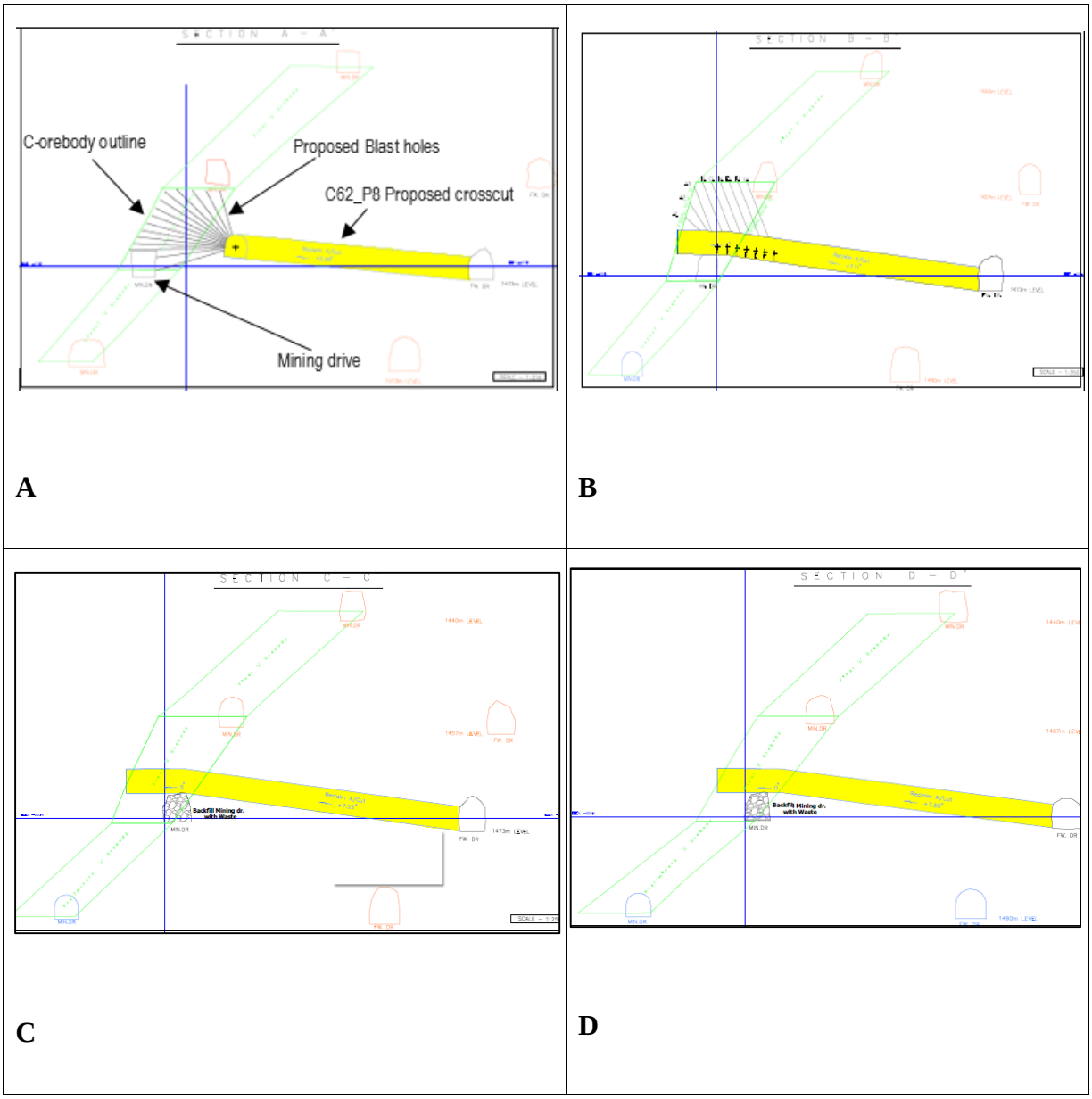

Figure 4. 1. ***(A) Cross-section 62P8 proposed cross-cut layout, (B) Cross-section 63P2 proposed cross-cut layout, (C) Cross-section 63P7 proposed cross-cut layout and (D) Cross-section 63P8 proposed cross-cut layout***

Results of the simulation of the expected field stress conditions Map3D stress model indicates potential extensive damage in the 62P8 cross cut and drive and damage of the 63P2 cross-cut after a few meters from the footwall drive (Figure 4.2). The conditions in 63P7 and 63P8 are expected to be fair (standard ground support) until about 30 m from the footwall drive.

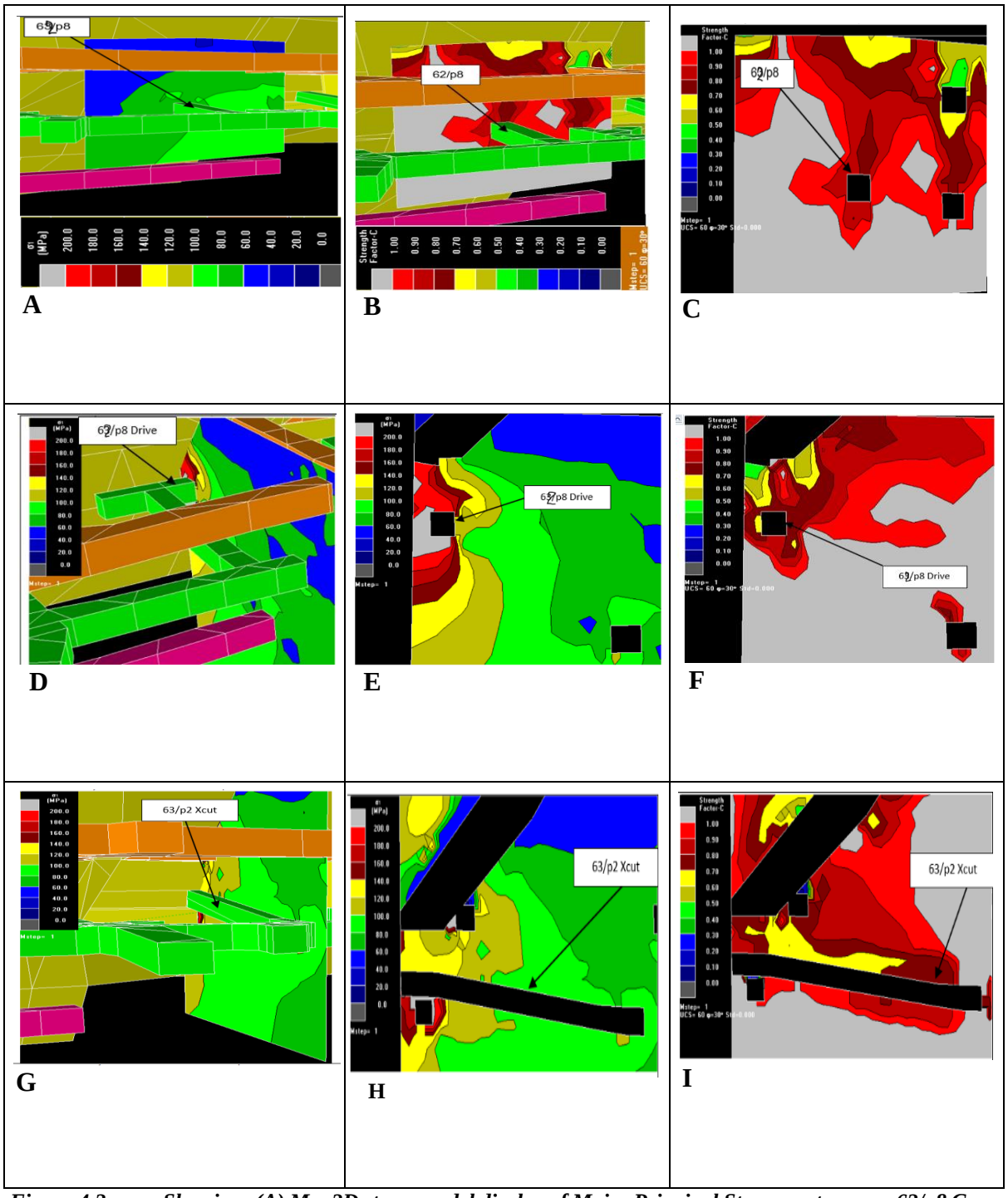

Figure 4.2 Showing; (A) Map3D stress model display of Major Principal Stress contours on 62/p8 Cross cut, (B) Map3D stress model display of strength factor contours on 62/p8 Cross cut (Potential damage- SF<1), (C) Map3D stress model display of strength factor contours on 62/p8 Cross cut (Potential damage- SF<1), (D) Map3D stress model display of Major principal stress contours on 62/p8 Drive, (E) Map3D stress model display

of Major principal stress contours on 62/p8 Drive, (F) Map3D stress model display of strength factor contours on 62/p8 Drive (Potential damage- SF<1), (G) Map3D stress model display of Major principal stress contours on 63/p2 Drive and (H) Map3D stress model display of strength factor contours on 63/p2 cross-cut (Potential damage- SF<1).

4.3 GEOMECHANICAL PROPERTIES OF THE ROCKS

4.3.1 Introduction

Geomechanical properties of rock mass are important to assist us understand the general behaviour of rocks. The rock's deformability response to stress levels such as brittleness and ductility must be understood to predict the level of stress a give rock mass will be subjected to before rock fall or rock burst can occur. Rock parameters such as Brazilian Tensile Strength, Uniaxial Compressive Strength and Triaxial Compressive Strength are important and should be known accurately.

4.3.2 Brazilian Tensile Test Results

The test was done on disc shaped thirty (30) specimens of 27 mm long each (Figure 4.3) and average results were obtained (Figure 4.3). The C-Quartzite had the highest average tensile strength of 11.5 MPa and Dolomite had the lowest average value of 6.2 MPa. During the test, all the rock samples showed brittle deformation with Quartzite being harder than Dolomite as can be seen in Figure 4.3 on the basis of tensile strength values. This means that one will require more tensional load to deform a Quartzite rock than required to deform Dolomite of the same rock mass size.

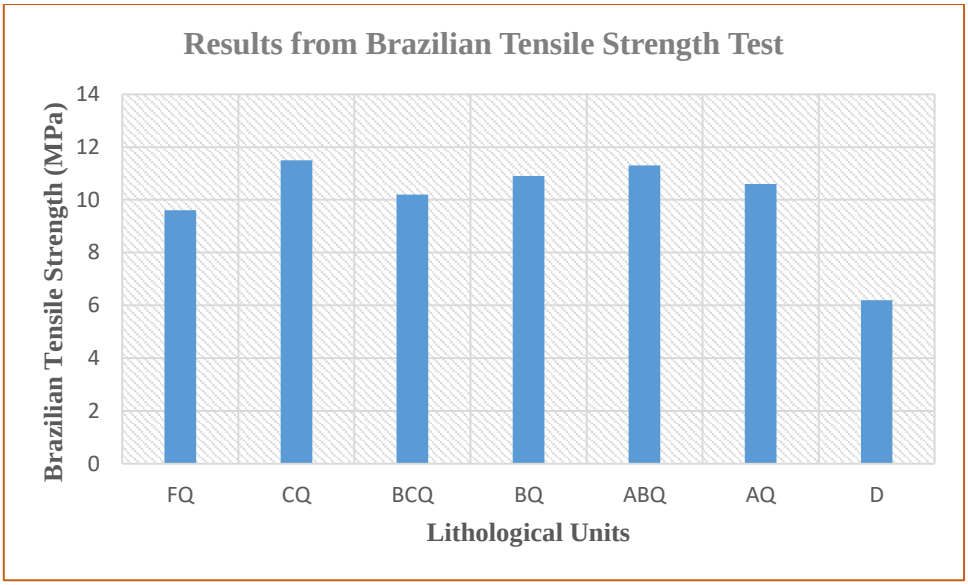

Figure 4.3 Results from Brazilian Tensile Strength test, C-Quartzite (CQ) with highest value & Dolomite (D) with lowest. FQ (Footwall Quartzite), CQ (C-Quartzite), BCQ (BC-Quartzite), BQ (B-Quartzite), ABQ (AB-Quartzite, AQ (A-Quartzite) and D (Dolomite).

4.3.3 Uniaxial Compressive Strength Results

The investigations of strains on rock specimens during uniaxial compression test were conducted and plotted graphically. Two components of strain in the cylindrical shape specimen, axial and radial components were studied. Strain gauges fixed on specimen surface were used in this study. Axial and radial components of strain were measured directly. Strain measurement was necessary for determination of Young's modulus and Poisson's ratio. Figures 4.5 to 4.22 show the plotted results.

The B-Quartzite had the highest average uniaxial compressive strength value and Dolomite had the lowest value (Figure 4.4). This shows that Quartzite will require more compressional load to deform than required by the Dolomite of the same rock mass size.

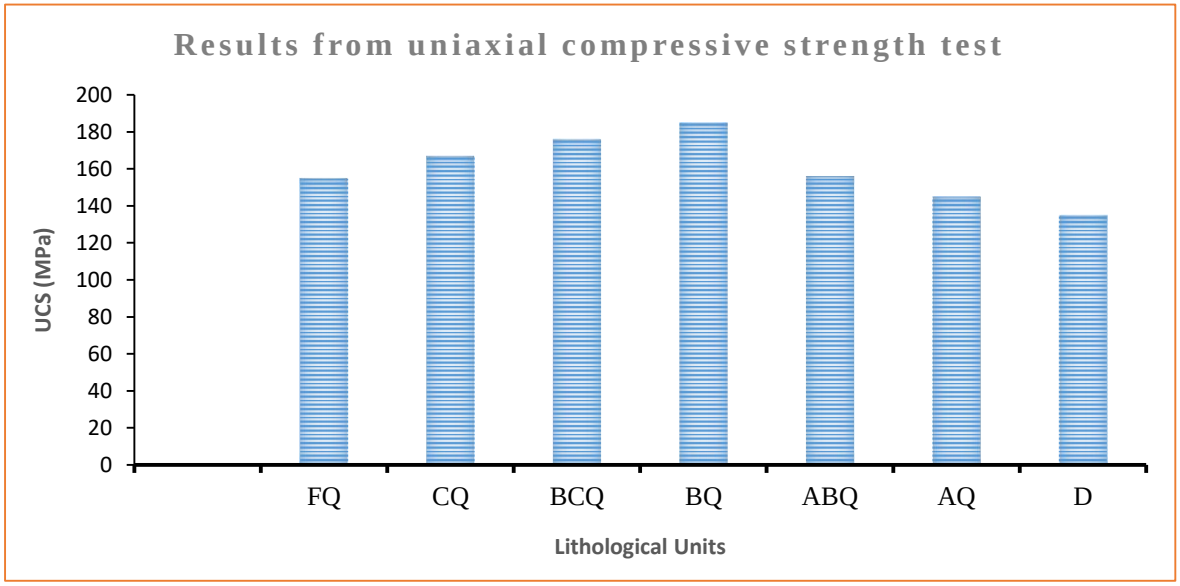

Figure 4.4 Average results for Uniaxial Compressive Strength (UCS) for Lithological units

4.3.4 Stress and Strain Curves

The typical behaviour of strain component curves of the rock samples during Uniaxial Compressive Strength tests are illustrated in Figures 4.5 to 4.22. Axial strain (red curves) performs the lowest sensitivity and the failure can be identified in relatively short advance only. Radial strain (blue curves) shows more nonlinear trend than axial one, thus, recognition of approaching failure is earlier.

Calculated Young's modulus is dependent on considered interval of axial load, as is shown in Figures 4.5 to 4.22. Precariousness can occur if there is no specified stress level for Young's modulus determination. Uncertainty of methodology proceeds constantly in determination of rock deformation characteristics. International Society for Rock Mechanics (ISRM) methods suggest three approaches for calculation of Young's modulus. Comparison of the approaches was carried out and variation of obtained results was discussed e.g. by study of Malkowski. European standard, established also in the Czech Republic, requires determination of the modulus from unloading-reloading loop at certain level of uniaxial compressive strength (UCS) of the tested rock. The last mentioned approach should overcome problem of nonlinearity of the axial strain, which was also recognized on the rock samples in this study.

Appropriate determination of Poisson's ratio is also an issue. Variability of Poisson's ratio along whole range of loading can be noticed on the data on Figures 4.5 to 4.22. The parameter dependent on the radial strain, which performed nonlinear trend. Poisson's ratio was calculated after reaching of stress at the minimal absolute volume of the specimen.

The failure load of 222.3 kN was applied on sample 01, with peak strength of 126.5 MPa and giving 3246 micro strain of axial strain at failure. Figure 4.5 shows three essential parameters that were determined; unconfined compressive strength (UCS), secant and tangent Young's Modulus (E Sec and E Tan), and secant and tangent Poisson's Ratio (ν Sec and ν Tan) from sample number 01.

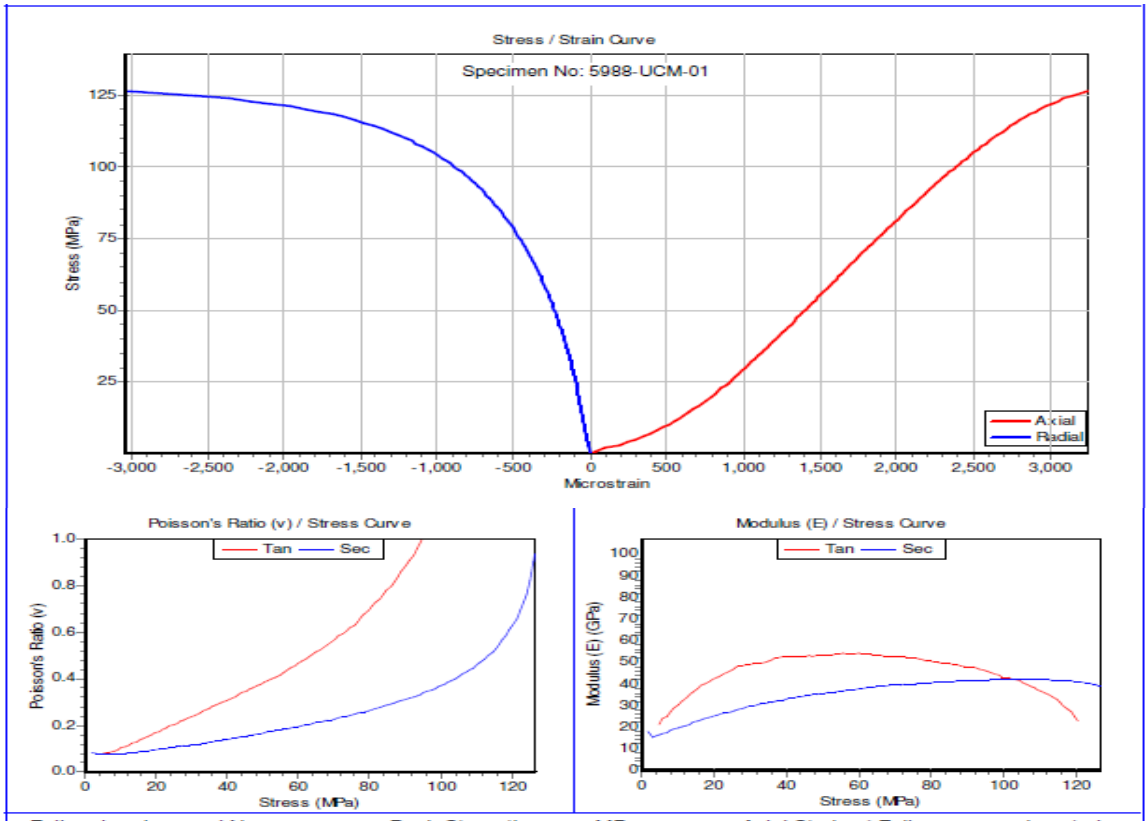

Failure Load: 222.3 kN | Peak Strength: 126.5 MPa | Axial Strain at Failure: 3246 microstrain

% Strength	Strength (MPa)	E Tan (GPa)	E Sec (GPa)	ν Tan	ν Sec
10	12.7	35	21.5	0.124	0.084
20	25.3	47.3	27.8	0.210	0.108
30	38	52.5	32.6	0.302	0.138
40	50.6	53.3	36	0.393	0.171
50	63.3	53.3	38.5	0.506	0.207
60	75.9	51.6	40.3	0.646	0.251
70	88.6	48	41.4	0.861	0.305
80	101	42.9	41.9	1.229	0.378
90	114	32.8	41.7	2.150	0.514

Figure 4.5 Uniaxial Compressive Test with elastic modulus and poisson's ratio measurements by means of strain gauges for sample-01

The failure load of 288.3 kN was applied on sample 02, with peak strength of 164.2 MPa and giving 3072 micro strain of axial strain at failure. Figure 4.6 shows three essential parameters that were determined; unconfined compressive strength (UCS), secant and tangent Young's Modulus (E Sec and E Tan), and secant and tangent Poisson's Ratio (ν Sec and ν Tan) from sample number 02.

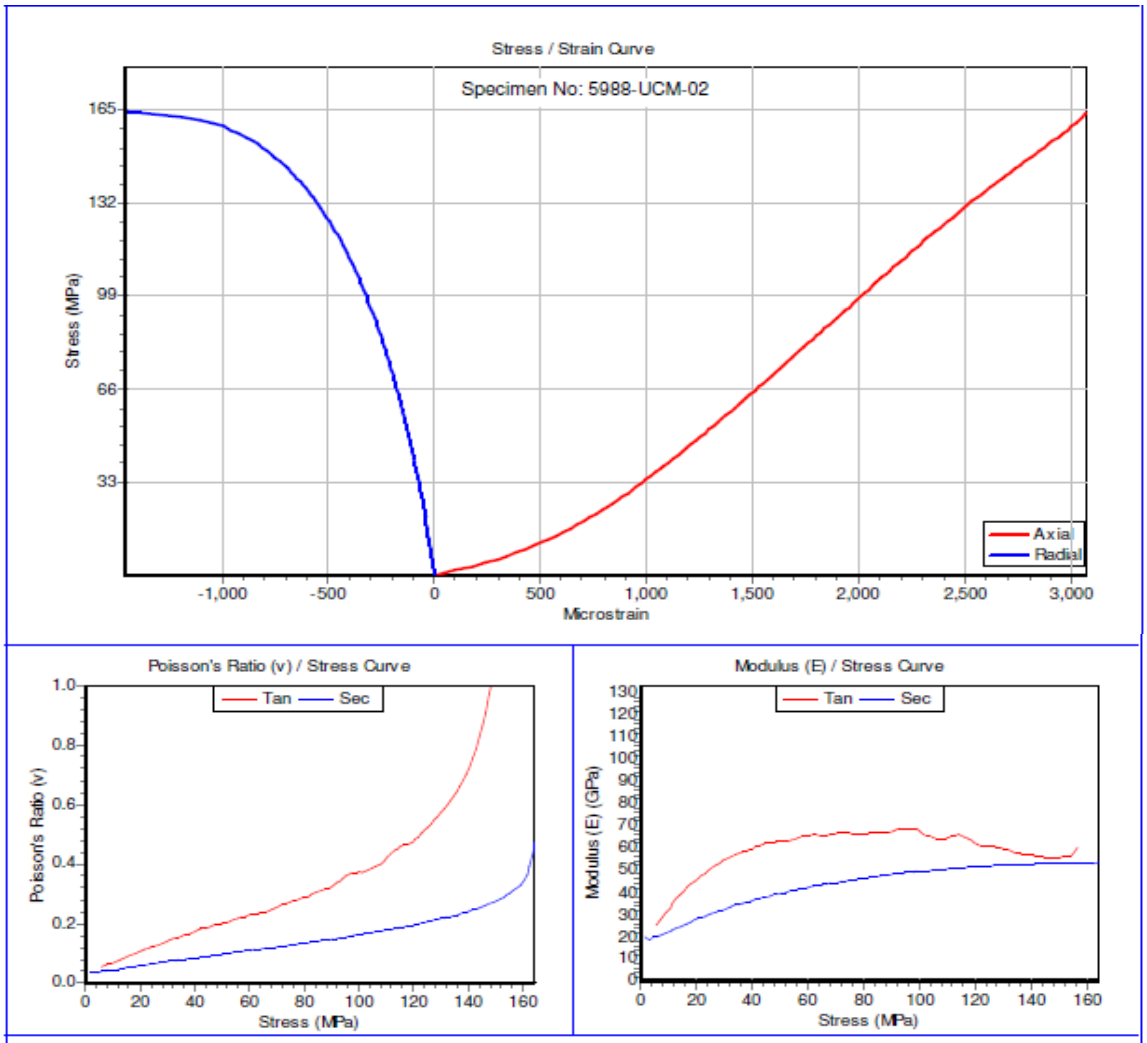

Failure Load: 288.2 kN | Peak Strength: 164.2 MPa | Axial Strain at Failure: 3072 microstrain

% Strength	Strength (MPa)	E Tan (GPa)	E Sec (GPa)	v Tan	v Sec
10	16.4	42.2	26.1	0.095	0.054
20	32.8	56.8	34.2	0.154	0.077
30	49.3	63	39.7	0.203	0.098
40	65.7	65.4	43.8	0.245	0.118
50	82.1	66.6	46.8	0.295	0.138
60	98.5	68.6	49.4	0.373	0.161
70	115	65.3	51.1	0.459	0.186
80	131	59.3	52.3	0.584	0.218
90	148	55.7	52.8	0.969	0.267

Figure 4.6 Uniaxial Compressive Test results with elastic modulus and poisson's ratio for sample-02

The failure load of 233.9 kN was applied on sample 03, with peak strength of 132.9 MPa and giving 3178 micro strain of axial strain at failure. Figure 4.7 shows three essential parameters that were determined; unconfined compressive strength (UCS), secant and tangent Young's Modulus (E Sec and E Tan), and secant and tangent Poisson's Ratio (ν Sec and ν Tan) from sample number 03.

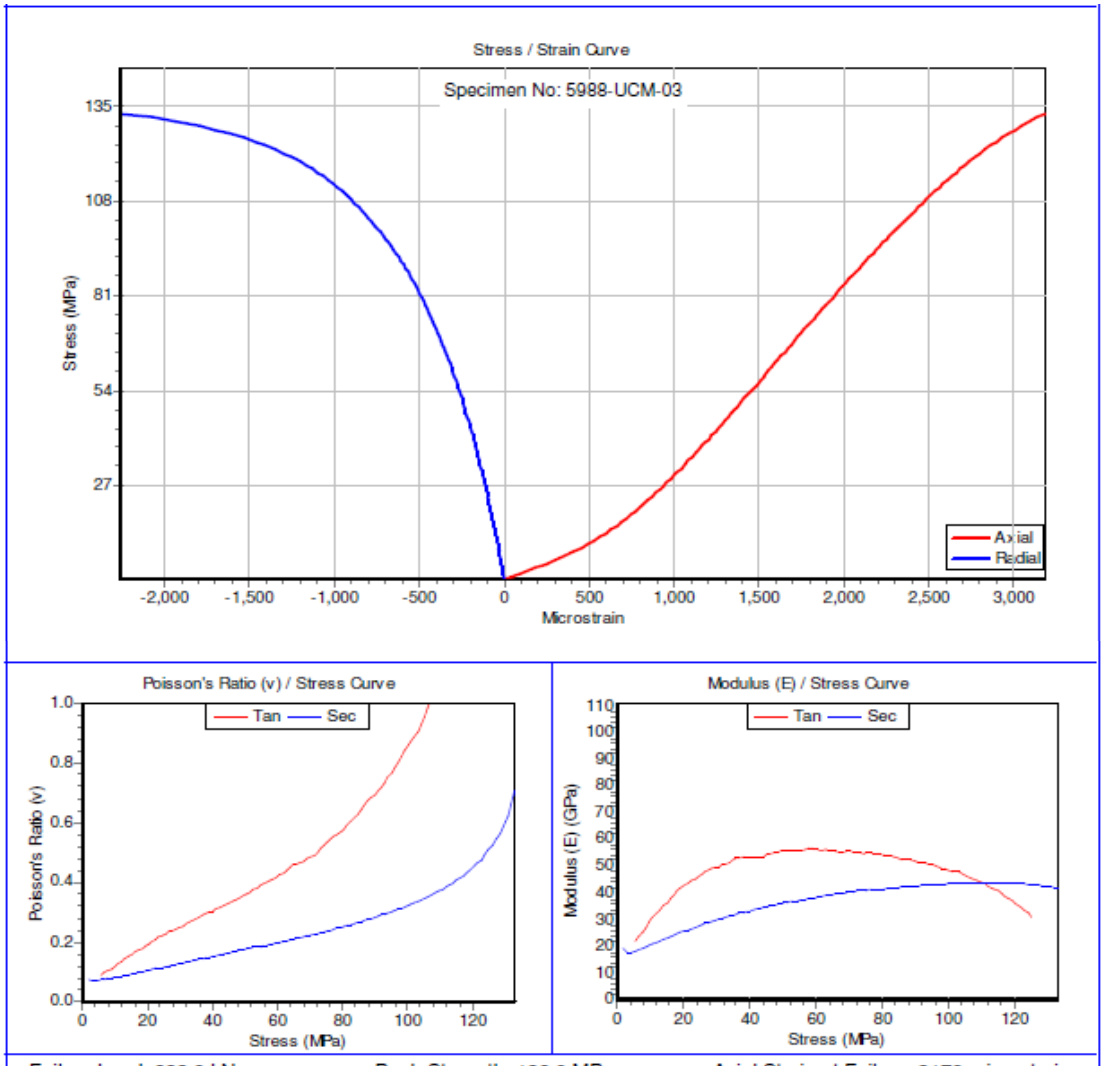

Failure Load: 233.9 kN | Peak Strength: 132.9 MPa | Axial Strain at Failure: 3178 microstrain

% Strength	Strength (MPa)	E Tan (GPa)	E Sec (GPa)	ν Tan	ν Sec
10	13.3	35.5	22.6	0.151	0.090
20	26.6	48.6	28.9	0.239	0.124
30	39.9	53.7	33.4	0.304	0.152
40	53.2	56	37.1	0.383	0.183
50	66.5	55.4	39.7	0.467	0.215
60	79.7	54.1	41.7	0.581	0.252
70	93	51	43	0.750	0.298
80	106	45.3	43.6	1.014	0.358
90	120	36.1	43.5	1.698	0.453

Figure 4.7 Uniaxial Compressive Test results with elastic modulus and poisson's ratio sample-03

The failure load of 235.8 kN was applied on sample 04, with peak strength of 134.7 MPa and giving 3232 micro strain of axial strain at failure. Figure 4.8 shows three essential parameters that were determined; unconfined compressive strength (UCS), secant and tangent Young's Modulus (E Sec and E Tan), and secant and tangent Poisson's Ratio (ν Sec and ν Tan) from sample number 04

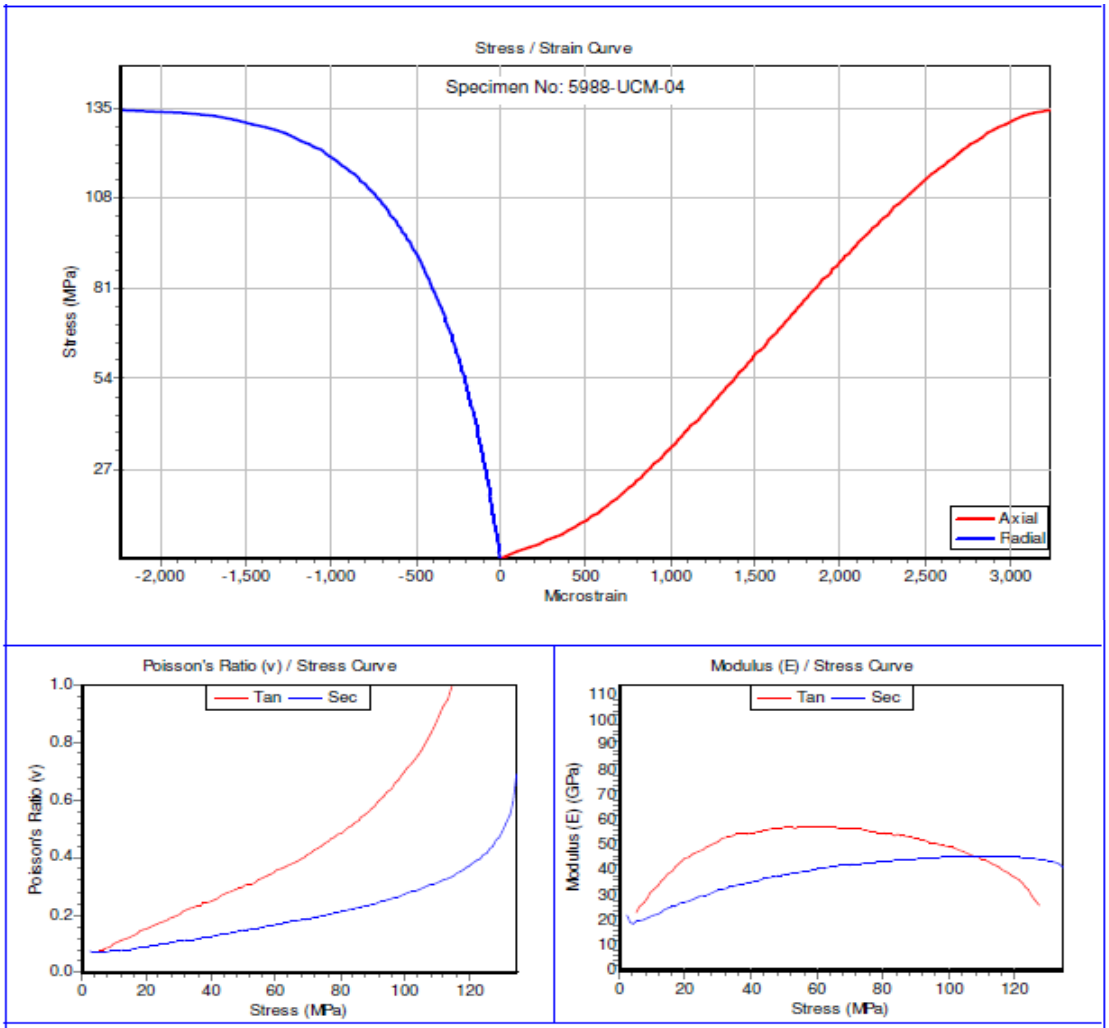

Failure Load: 235.8 kN | Peak Strength: 134.7 MPa | Axial Strain at Failure: 3232 microstrain

% Strength	Strength (MPa)	E Tan (GPa)	E Sec (GPa)	ν Tan	ν Sec
10	13.5	37.1	24.2	0.120	0.079
20	26.9	50	30.8	0.189	0.103
30	40.4	55.2	35.7	0.254	0.128
40	53.9	57	39.3	0.320	0.155
50	67.3	56.9	41.9	0.395	0.183
60	80.8	54.3	43.7	0.494	0.215
70	94.3	51.2	44.9	0.628	0.253
80	108	45.6	45.4	0.832	0.305
90	121	36.3	45.1	1.288	0.380

Figure 4.8 Uniaxial Compressive Strength test results with elastic modulus and poisson's ratio for sample-04

The failure load of 313.1 kN was applied on sample 05, with peak strength of 178 MPa and giving 3241 micro strain of axial strain at failure. Figure 4.9 shows three essential parameters that were determined; unconfined compressive strength (UCS), secant and tangent Young's Modulus (E Sec and E Tan), and secant and tangent Poisson's Ratio (ν Sec and ν Tan) from sample number 05.

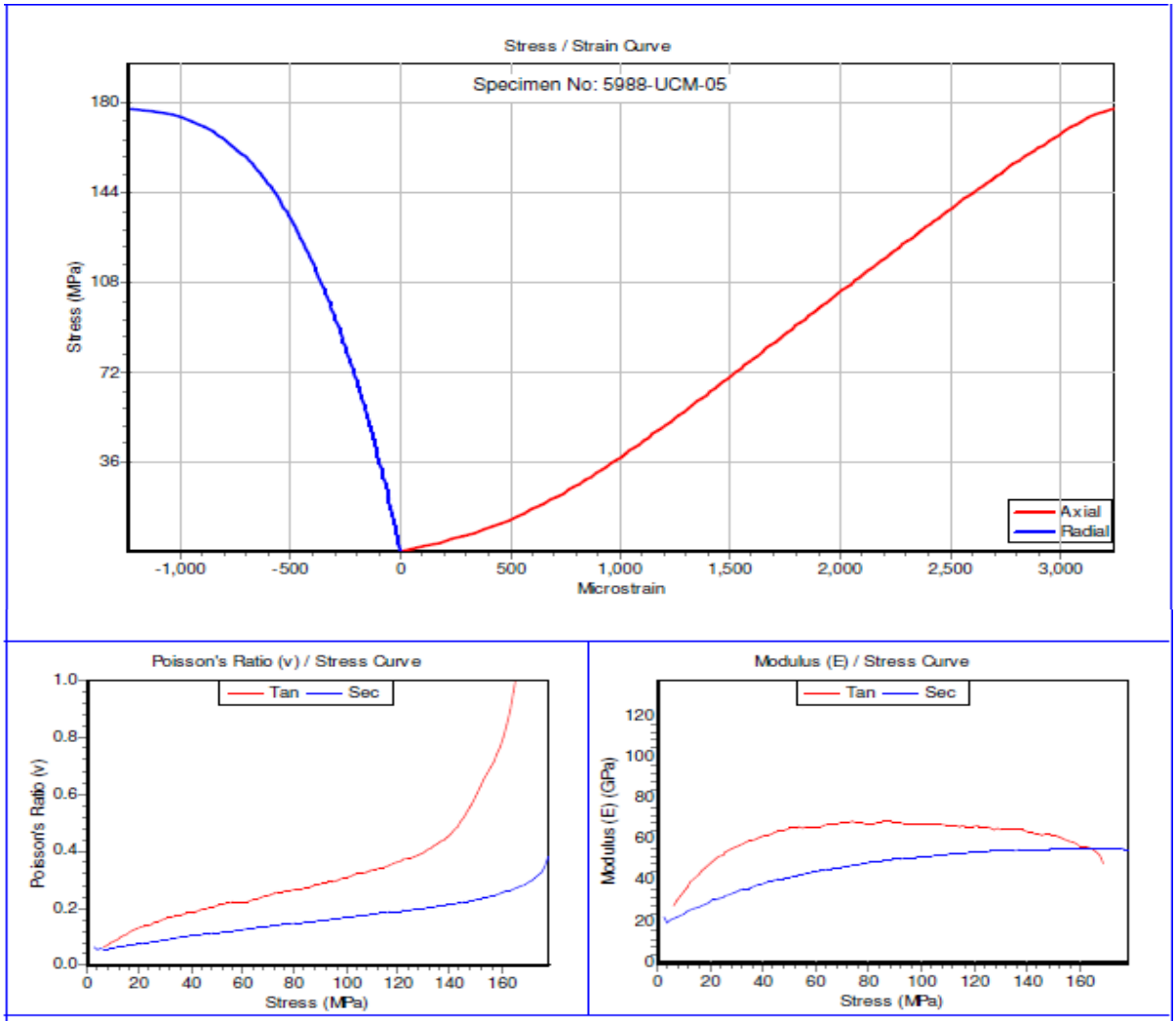

Failure Load: 313.1 kN | Peak Strength: 178 MPa | Axial Strain at Failure: 3241 microstrain

% Strength	Strength (MPa)	E Tan (GPa)	E Sec (GPa)	ν Tan	ν Sec
10	17.8	46.2	28.8	0.122	0.071
20	35.6	60.3	37.5	0.178	0.098
30	53.4	65.8	42.9	0.216	0.119
40	71.2	68.3	47.3	0.252	0.139
50	89	68.5	50.3	0.283	0.156
60	107	67.4	52.5	0.327	0.175
70	125	65.9	54.1	0.377	0.194
80	142	63	55.3	0.487	0.217
90	160	56.8	55.9	0.802	0.256

Figure 4.9 Uniaxial Compressive Strength test results with elastic modulus and poisson's ratio for sample-05

The failure load of 437.9 kN was applied on sample 06, with peak strength of 245 MPa and giving 4084 micro strain of axial strain at failure. Figure 4.10 shows three essential parameters that were determined; unconfined compressive strength (UCS), secant and tangent Young's Modulus (E Sec and E Tan), and secant and tangent Poisson's Ratio (ν Sec and ν Tan) from sample number 06.

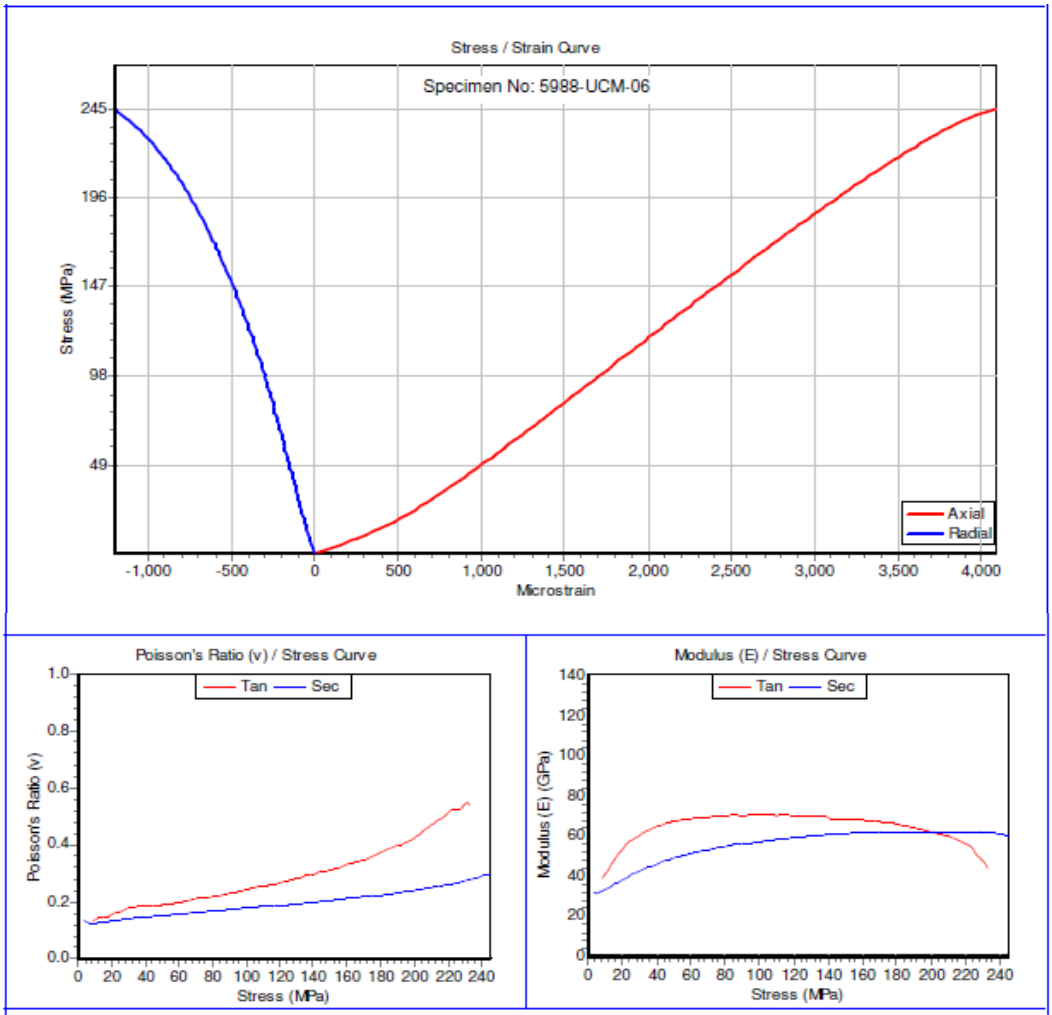

Failure Load: 437.9 kN | Peak Strength: 245 MPa | Axial Strain at Failure: 4084 microstrain

% Strength	Strength (MPa)	E Tan (GPa)	E Sec (GPa)	ν Tan	ν Sec
10	24.5	58.3	41.1	0.169	0.137
20	49	67	49	0.190	0.152
30	73.5	70.3	54.2	0.212	0.165
40	98	70.5	57.5	0.241	0.177
50	123	70.3	59.7	0.270	0.189
60	147	68.8	61.2	0.309	0.203
70	172	66.9	62.1	0.351	0.219
80	196	62.9	62.6	0.417	0.238
90	221	56.1	62.4	0.516	0.262

Figure 4.10 Uniaxial Compressive Strength test results with elastic modulus and poisson's ratio for sample-06

The failure load of 260.5 kN was applied on sample 07, with peak strength of 144.7 MPa and giving 3131 micro strain of axial strain at failure. Figure 4.11 shows three essential parameters that were determined; unconfined compressive strength (UCS), secant and tangent Young's Modulus (E Sec and E Tan), and secant and tangent Poisson's Ratio (ν Sec and ν Tan) from sample 07.

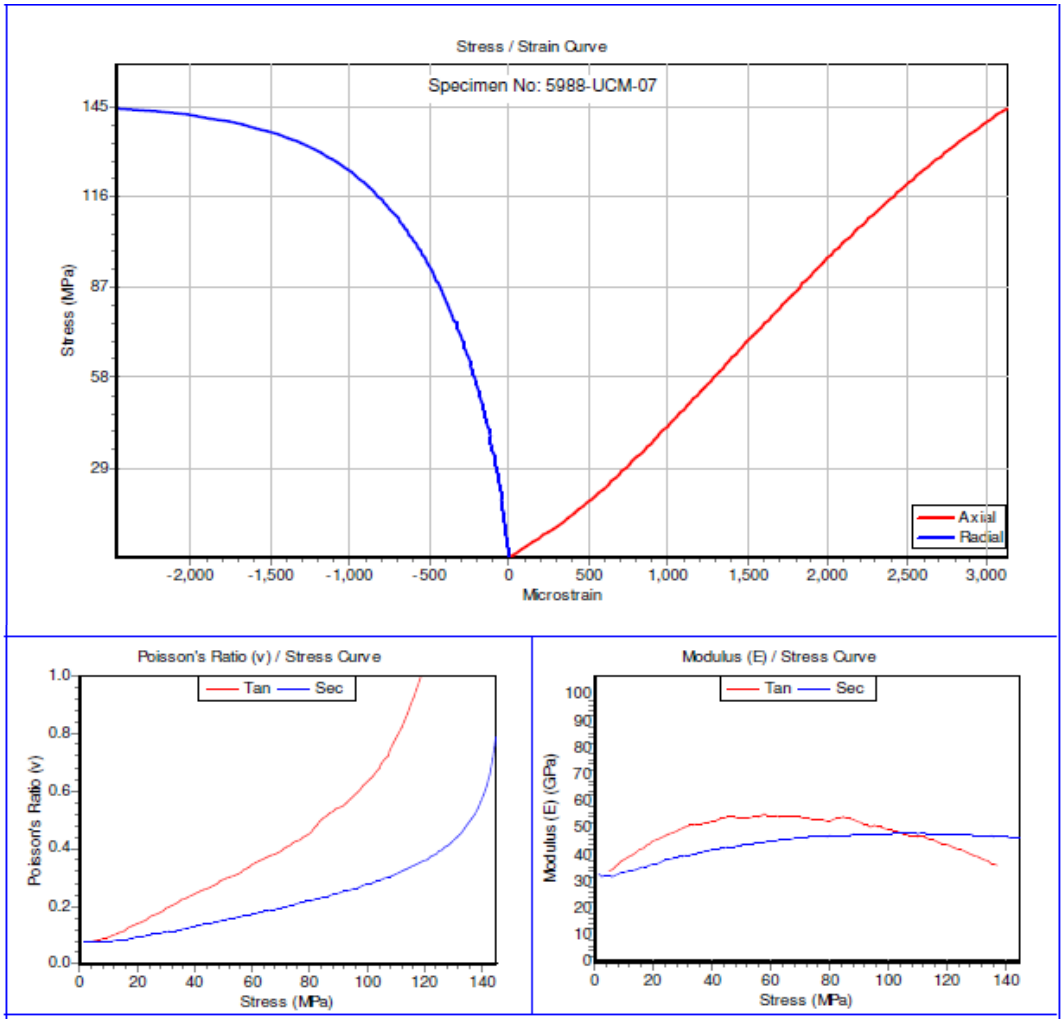

Failure Load: 260.5 kN | Peak Strength: 144.7 MPa | Axial Strain at Failure: 3131 microstrain

% Strength	Strength (MPa)	E Tan (GPa)	E Sec (GPa)	ν Tan	ν Sec
10	14.5	41.8	35.3	0.116	0.085
20	28.9	50.1	39.4	0.191	0.109
30	43.4	53.8	42.8	0.262	0.140
40	57.9	55.1	45	0.332	0.168
50	72.3	53.7	46.7	0.413	0.203
60	86.8	53.7	47.5	0.525	0.237
70	101	49.1	48.2	0.655	0.282
80	116	45.3	48.1	0.926	0.340
90	130	39.3	47.5	1.685	0.432

Figure 4.11 Uniaxial Compressive Strength test results with elastic modulus and poisson's ratio for sample-07

The failure load of 276.2 kN was applied on sample 08, with peak strength of 153.4 MPa and giving 3943 micro strain of axial strain at failure. Figure 4.12 shows three essential parameters that were determined; unconfined compressive strength (UCS), secant and tangent Young's Modulus (E Sec and E Tan), and secant and tangent Poisson's Ratio (ν Sec and ν Tan) from sample number 08.

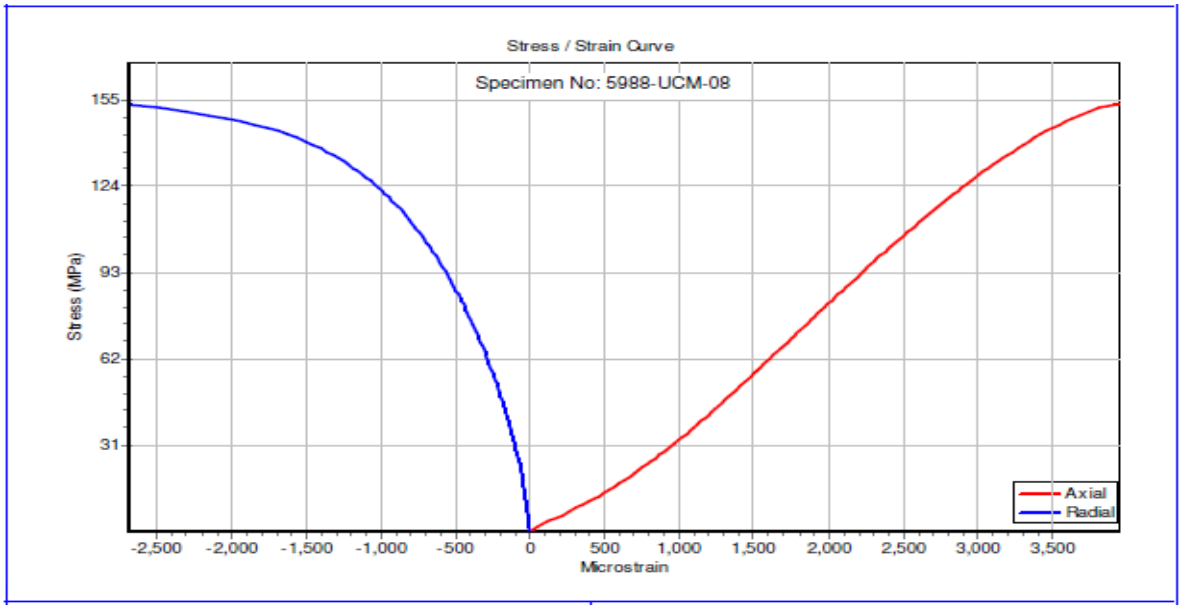

Failure Load: 276.2 kN | Peak Strength: 153.4 MPa | Axial Strain at Failure: 3943 microstrain

% Strength	Strength (MPa)	E Tan (GPa)	E Sec (GPa)	ν Tan	ν Sec
10	15.3	34.5	28.8	0.122	0.073
20	30.7	43.8	32.8	0.217	0.109
30	46	48.1	36	0.291	0.143
40	61.4	50.5	38.7	0.376	0.179
50	76.7	50.4	40.5	0.452	0.214
60	92	48.7	41.8	0.542	0.252
70	107	45.5	42.6	0.665	0.294
80	123	40.3	42.8	0.899	0.351
90	138	31.7	42.1	1.504	0.439

Figure 4.12 Uniaxial Compressive Strength test results with elastic modulus and poisson's ratio for sample-08

The failure load of 228.4 kN was applied on sample 09, with peak strength of 126.5 MPa and giving 3564 micro strain of axial strain at failure. Figure 4.13 shows three essential parameters that were determined; unconfined compressive strength (UCS), secant and tangent Young's Modulus (E Sec and E Tan), and secant and tangent Poisson's Ratio (ν Sec and ν Tan) from sample number 09.

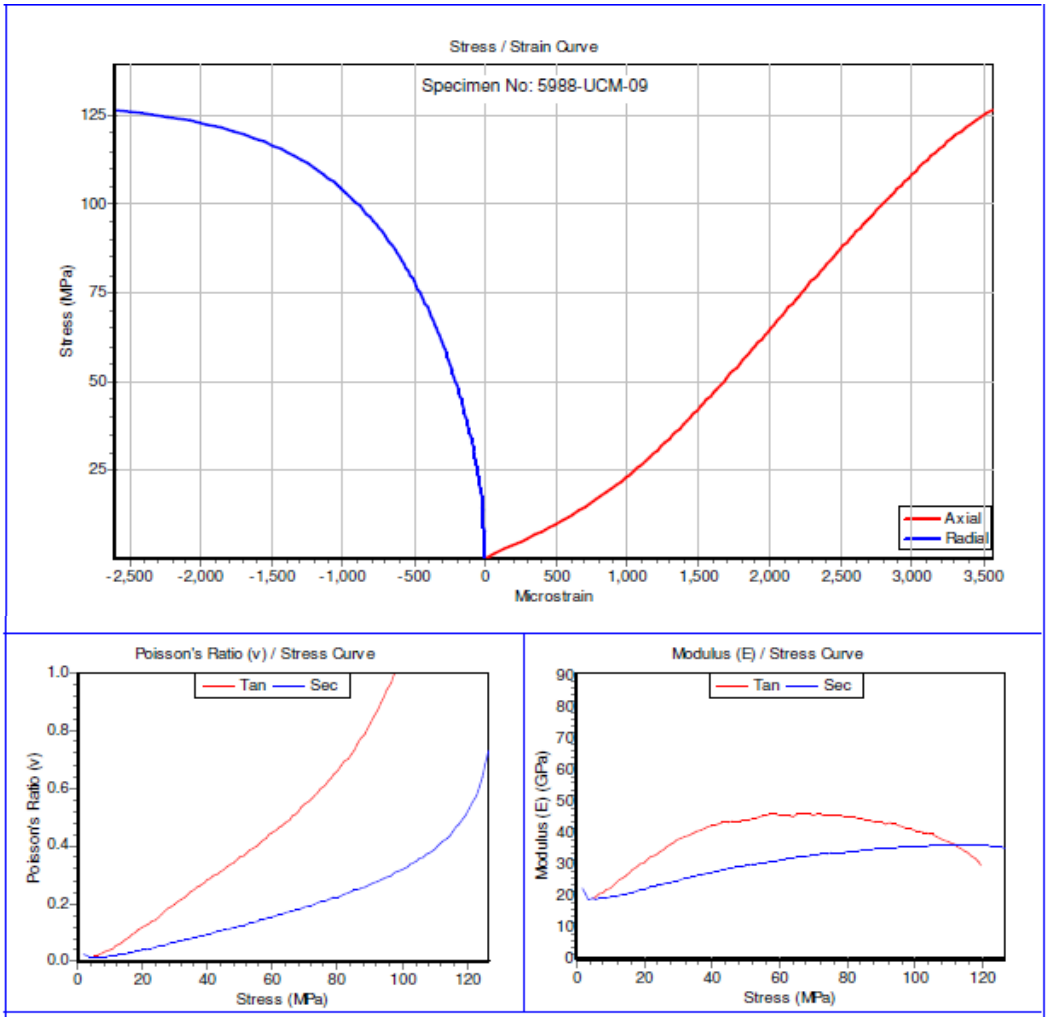

Failure Load: 228.4 kN | Peak Strength: 126.5 MPa | Axial Strain at Failure: 3564 microstrain

% Strength	Strength (MPa)	E Tan (GPa)	E Sec (GPa)	ν Tan	ν Sec
10	12.7	25.2	20.4	0.059	0.023
20	25.3	35	24	0.163	0.054
30	38	42	27.4	0.272	0.090
40	50.6	44.4	30.1	0.368	0.126
50	63.3	45.5	32.3	0.481	0.168
60	75.9	45.5	33.9	0.611	0.209
70	88.6	43.5	35.2	0.807	0.264
80	101	40.8	35.9	1.116	0.329
90	114	34.6	36.2	1.947	0.438

Figure 4.13 Showing Uniaxial Compressive Strength test results with elastic modulus and poisson's ratio for sample-09

The failure load of 213.3 kN was applied on sample 10, with peak strength of 118.9 MPa and giving 3051 micro strain of axial strain at failure. Figure 4.14 shows three essential parameters that were determined; unconfined compressive strength (UCS), secant and tangent Young's Modulus (E Sec and E Tan), and secant and tangent Poisson's Ratio (ν Sec and ν Tan) from sample number 10.

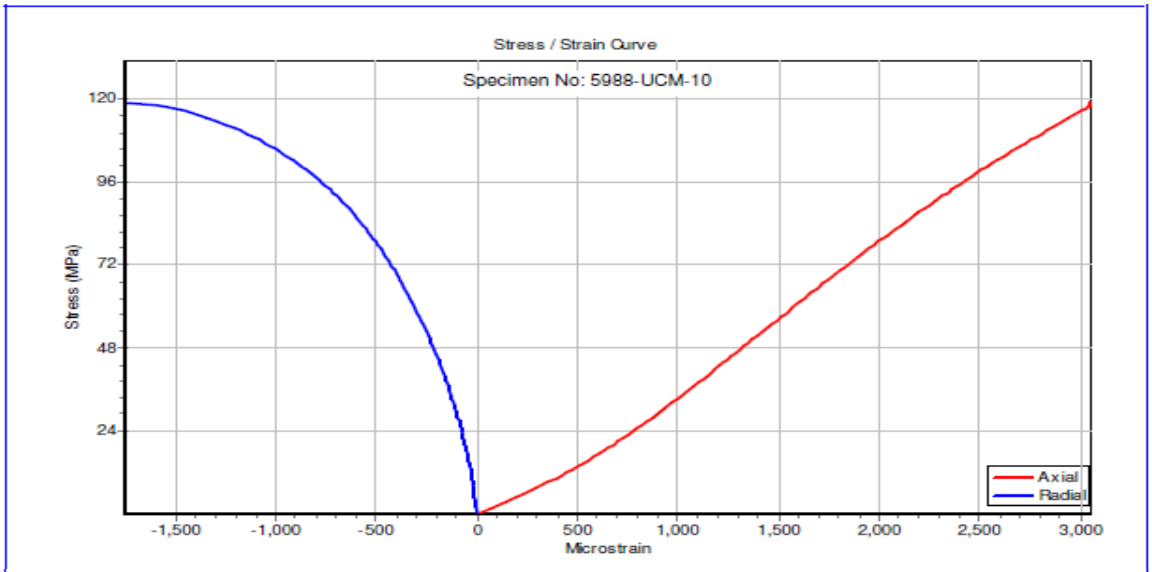

Failure Load: 213.3 kN | Peak Strength: 118.9 MPa | Axial Strain at Failure: 3051 microstrain

% Strength	Strength (MPa)	E Tan (GPa)	E Sec (GPa)	ν Tan	ν Sec
10	11.9	32.5	26.9	0.107	0.068
20	23.8	41.1	30.8	0.193	0.099
30	35.7	45.5	34.2	0.272	0.132
40	47.6	46.2	36.5	0.340	0.166
50	59.5	46.1	38	0.403	0.196
60	71.3	44.5	39	0.481	0.230
70	83.2	41.8	39.6	0.602	0.269
80	95.1	38.1	39.7	0.802	0.318
90	107	33.5	39.3	1.149	0.387

Figure 4.14 Showing Uniaxial Compressive Strength test results with elastic modulus and poisson's ratio for sample-10

The failure load of 199.6 kN was applied on sample 11, with peak strength of 112.4 MPa and giving 2581 micro strain of axial strain at failure. Figure 4.15 shows three essential parameters that were determined; unconfined compressive strength (UCS), secant and tangent Young's Modulus (E Sec and E Tan), and secant and tangent Poisson's Ratio (ν Sec and ν Tan) from sample number 11.

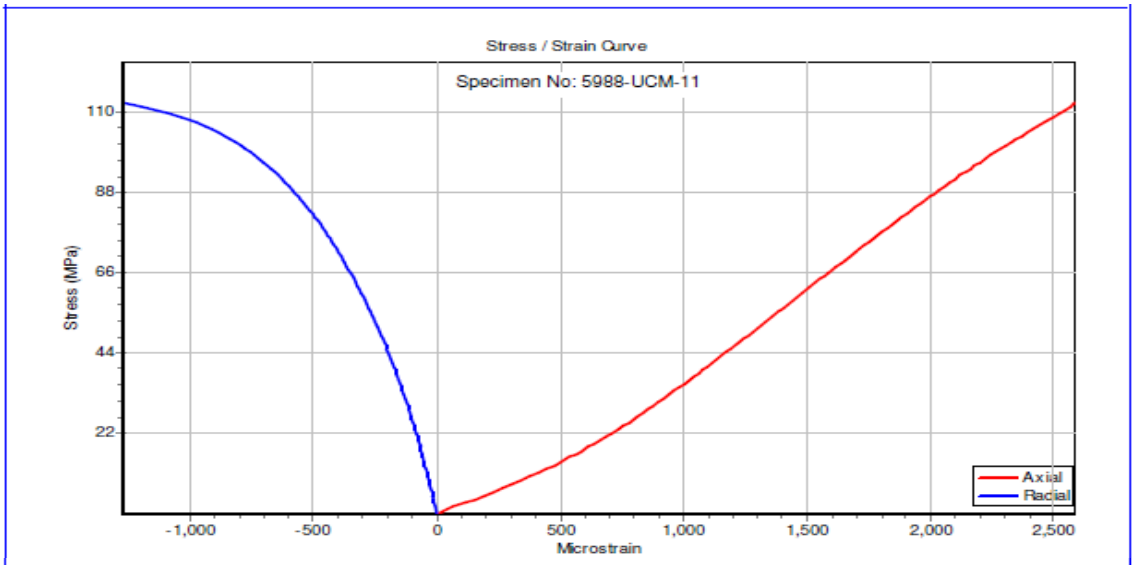

Failure Load: 199.6 kN | Peak Strength: 112.4 MPa | Axial Strain at Failure: 2581 microstrain

% Strength	Strength (MPa)	E Tan (GPa)	E Sec (GPa)	ν Tan	ν Sec
10	11.2	32.4	27.6	0.122	0.098
20	22.5	43.6	31.6	0.196	0.120
30	33.7	49.1	35.4	0.268	0.146
40	45	51.5	37.9	0.325	0.171
50	56.2	52.2	40.3	0.387	0.200
60	67.4	51.6	41.8	0.449	0.225
70	78.7	49.8	43	0.548	0.256
80	89.9	46.1	43.6	0.717	0.295
90	101	41	43.7	1.100	0.352

Figure 4.15 Uniaxial Compressive Strength test results with elastic modulus and poisson's ratio for sample-11

The failure load of 394 kN was applied on sample 19, with peak strength of 223.6 MPa and giving 3918 micro strain of axial strain at failure. Figure 4.16 shows three essential parameters that were determined; unconfined compressive strength (UCS), secant and tangent Young's Modulus (E Sec and E Tan), and secant and tangent Poisson's Ratio (ν Sec and ν Tan) from sample number 19.

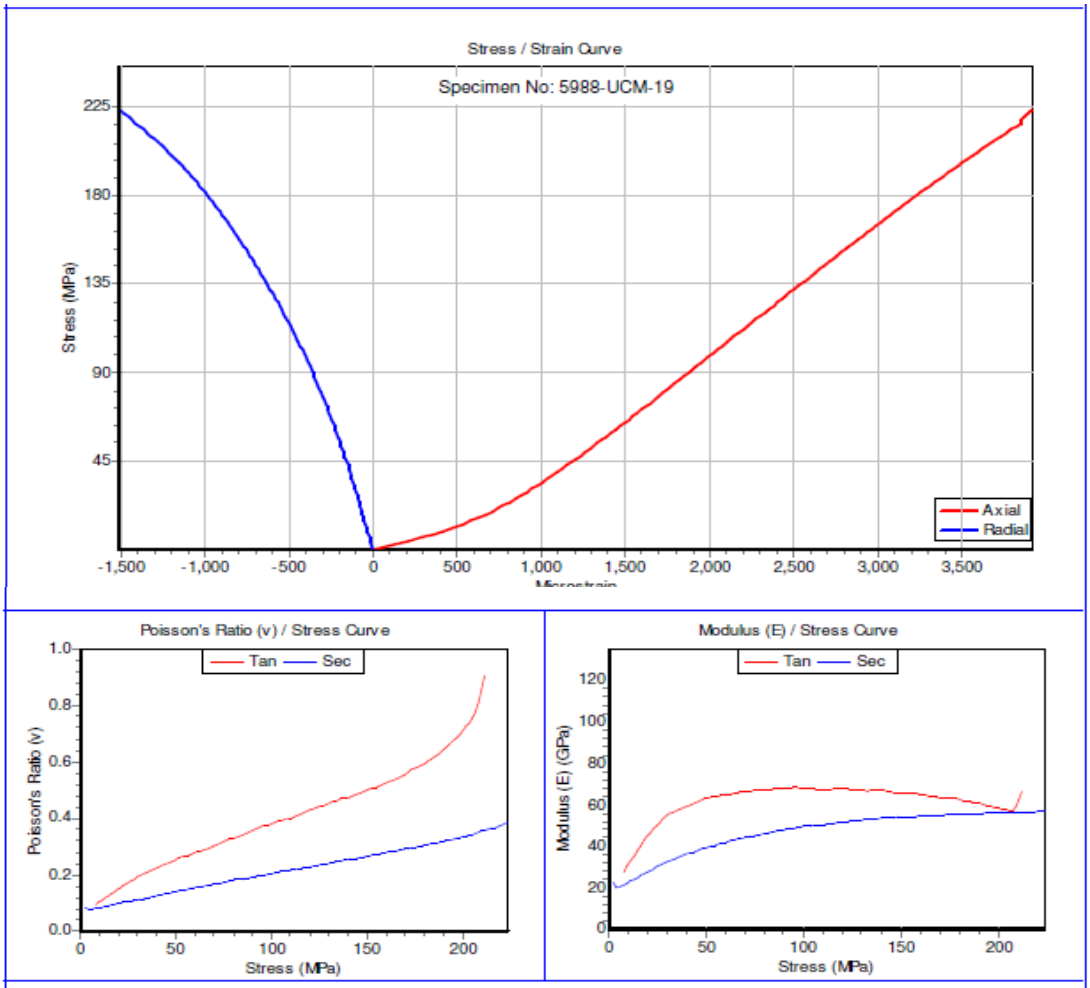

Failure Load: 394 kN | Peak Strength: 223.6 MPa | Axial Strain at Failure: 3918 microstrain

% Strength	Strength (MPa)	E Tan (GPa)	E Sec (GPa)	ν Tan	ν Sec
10	22.4	48.2	29.1	0.162	0.102
20	44.7	61.7	38.3	0.245	0.135
30	67.1	66.4	43.9	0.298	0.164
40	89.4	67.7	47.9	0.356	0.191
50	112	67.5	50.9	0.408	0.219
60	134	67	53	0.462	0.246
70	157	65.7	54.7	0.519	0.276
80	179	62.6	55.7	0.595	0.305
90	201	57.9	56.3	0.726	0.338

Figure 4.16 Uniaxial Compressive Strength test results with elastic modulus and poisson's ratio for sample-19

The failure load of 60.59 kN was applied on sample 24, with peak strength of 34.24 MPa and giving 1444 micro strain of axial strain at failure. Figure 4.17 shows three essential parameters that were determined; unconfined compressive strength (UCS), secant and tangent Young's Modulus (E Sec and E Tan), and secant and tangent Poisson's Ratio (ν Sec and ν Tan) from sample number 24.

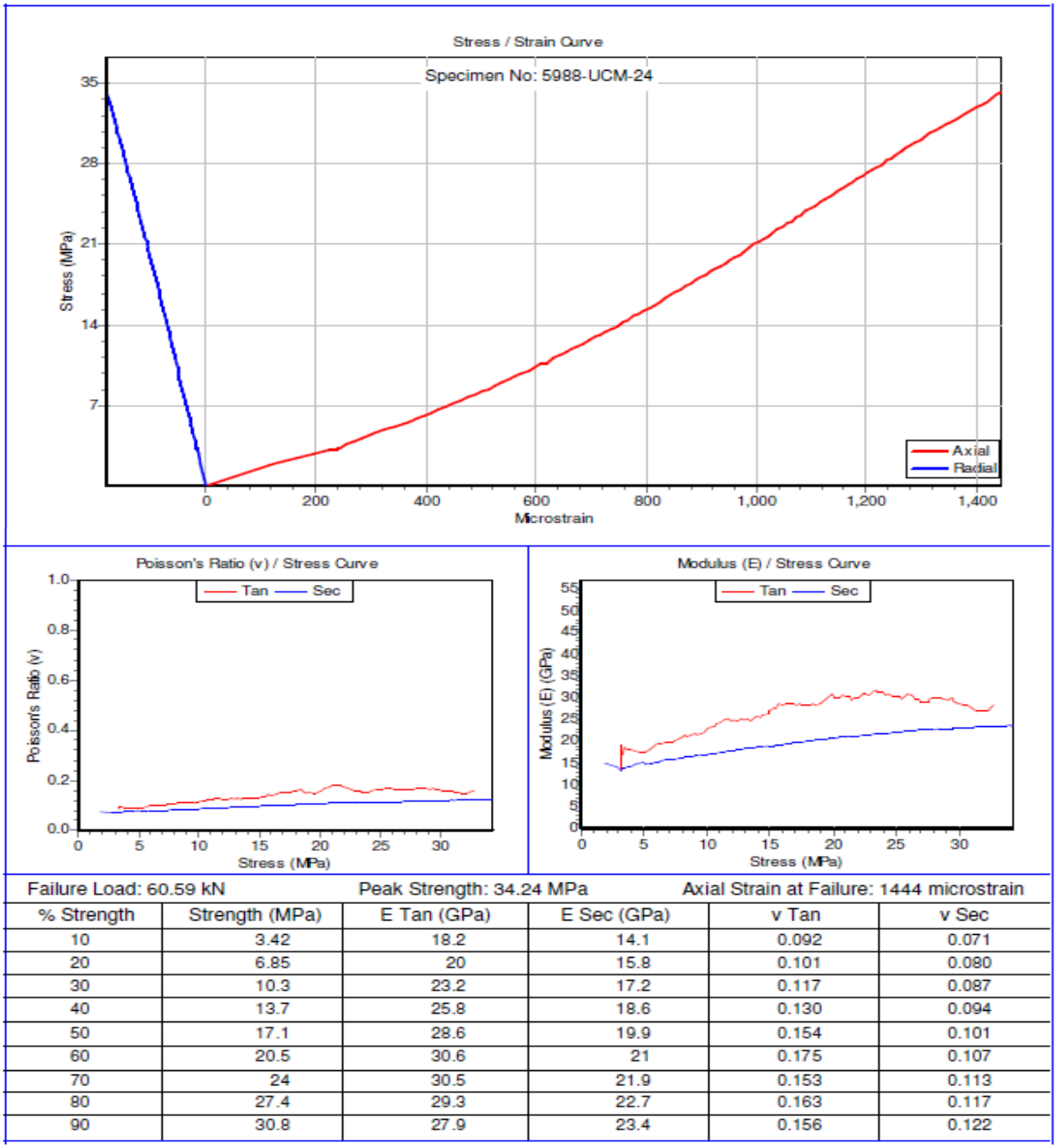

Failure Load: 60.59 kN | Peak Strength: 34.24 MPa | Axial Strain at Failure: 1444 microstrain

% Strength	Strength (MPa)	E Tan (GPa)	E Sec (GPa)	ν Tan	ν Sec
10	3.42	18.2	14.1	0.092	0.071
20	6.85	20	15.8	0.101	0.080
30	10.3	23.2	17.2	0.117	0.087
40	13.7	25.8	18.6	0.130	0.094
50	17.1	28.6	19.9	0.154	0.101
60	20.5	30.6	21	0.175	0.107
70	24	30.5	21.9	0.153	0.113
80	27.4	29.3	22.7	0.163	0.117
90	30.8	27.9	23.4	0.156	0.122

Figure 4.17 Uniaxial Compressive Strength test results with elastic modulus and poisson's ratio for sample-24

The failure load of 134.9 kN was applied on sample 25, with peak strength of 76.12 MPa and giving 2279 micro strain of axial strain at failure. Figure 4.18 shows three essential parameters that were determined; unconfined compressive strength (UCS), secant and tangent Young's Modulus (E Sec and E Tan), and secant and tangent Poisson's Ratio (ν Sec and ν Tan) from sample number 25.

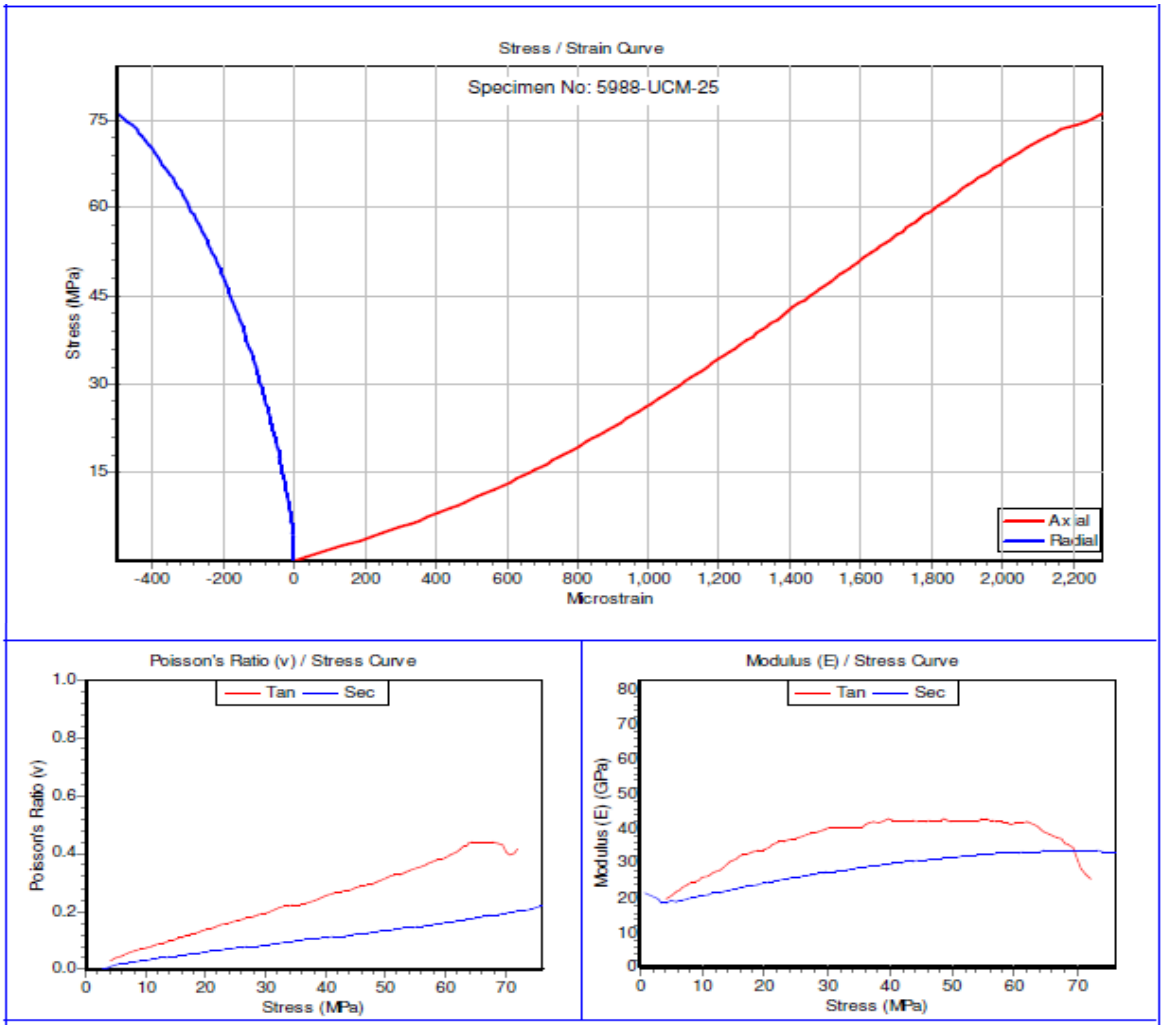

Failure Load: 134.9 kN | Peak Strength: 76.12 MPa | Axial Strain at Failure: 2279 microstrain

% Strength	Strength (MPa)	E Tan (GPa)	E Sec (GPa)	ν Tan	ν Sec
10	7.61	24.6	20.1	0.063	0.026
20	15.2	31.4	22.8	0.108	0.048
30	22.8	36.5	25.4	0.156	0.068
40	30.4	40.3	27.8	0.204	0.088
50	38.1	41.7	29.5	0.238	0.105
60	45.7	42.3	31.1	0.285	0.124
70	53.3	42.1	32.3	0.338	0.144
80	60.9	41.9	33.3	0.401	0.165
90	68.5	35.4	33.9	0.436	0.189

Figure 4.18 Uniaxial Compressive Strength test results with elastic modulus and poisson's ratio for sample-26

The failure load of 267.5 kN was applied on sample 26, with peak strength of 151.2 MPa and giving 3389 micro strain of axial strain at failure. Figure 4.19 shows three essential parameters that were determined; unconfined compressive strength (UCS), secant and tangent Young's Modulus (E Sec and E Tan), and secant and tangent Poisson's Ratio (ν Sec and ν Tan) from sample number 26.

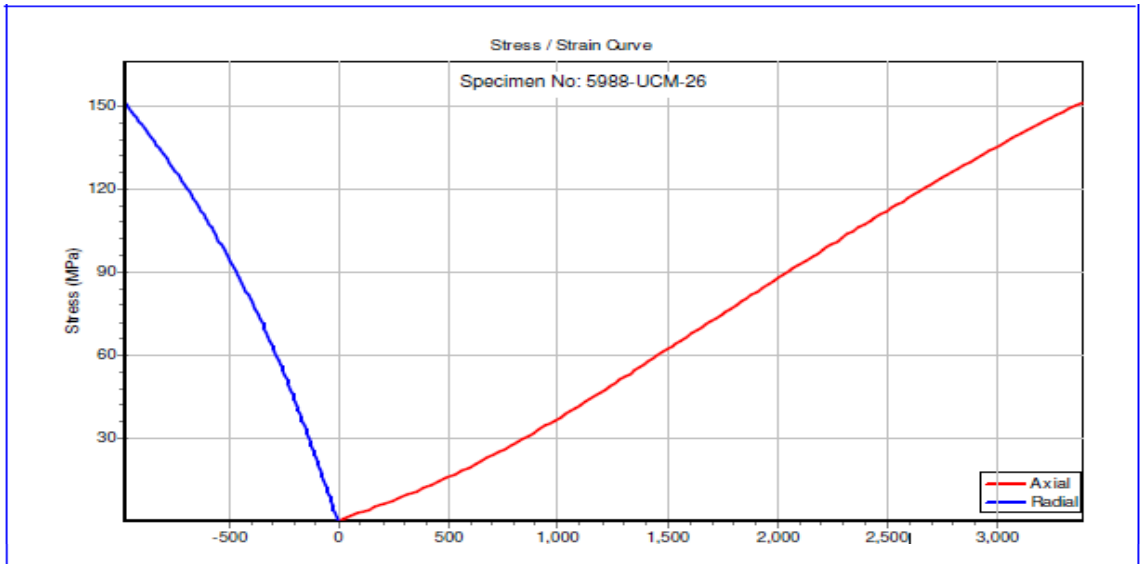

Failure Load: 267.5 kN | Peak Strength: 151.2 MPa | Axial Strain at Failure: 3389 microstrain

% Strength	Strength (MPa)	E Tan (GPa)	E Sec (GPa)	ν Tan	ν Sec
10	15.1	37.1	31.6	0.164	0.147
20	30.2	45.4	35.6	0.212	0.163
30	45.4	49.8	38.7	0.249	0.179
40	60.5	51.1	41.4	0.284	0.198
50	75.6	51	43	0.312	0.213
60	90.7	50	44.1	0.339	0.230
70	106	48.3	44.8	0.364	0.245
80	121	46.3	45.2	0.393	0.261
90	136	43.3	45.1	0.403	0.276

Figure 4.19 Uniaxial Compressive Strength test results with elastic modulus and poisson's ratio for sample-26

The failure load of 157 kN was applied on sample 27, with peak strength of 88.61 MPa and giving 3592 micro strain of axial strain at failure. Figure 4.20 shows three essential parameters that were determined; unconfined compressive strength (UCS), secant and tangent Young's Modulus (E Sec and E Tan), and secant and tangent Poisson's Ratio (ν Sec and ν Tan) from sample number 27.

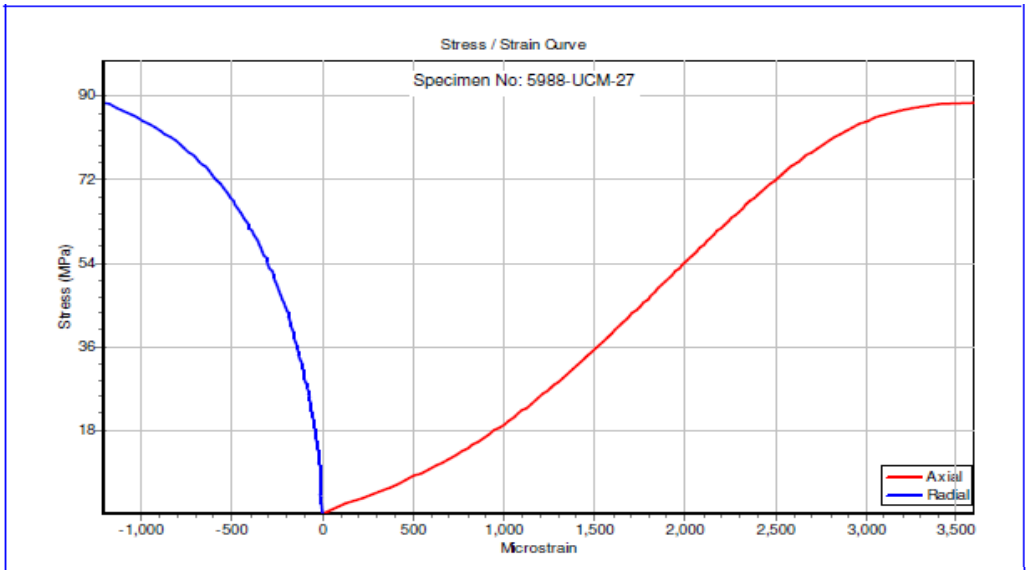

Failure Load: 157 kN | Peak Strength: 88.61 MPa | Axial Strain at Failure: 3592 microstrain

% Strength	Strength (MPa)	E Tan (GPa)	E Sec (GPa)	ν Tan	ν Sec
10	8.86	20.2	16.4	0.043	0.030
20	17.7	27.2	18.9	0.108	0.046
30	26.6	32.8	21.5	0.193	0.068
40	35.4	36.6	23.6	0.242	0.094
50	44.3	37.6	25.5	0.344	0.119
60	53.2	37.7	27	0.440	0.151
70	62	36.4	28.1	0.570	0.185
80	70.9	32.2	28.8	0.700	0.230
90	79.7	21.8	28.8	0.834	0.292

Figure 4.20 Uniaxial Compressive Strength test results with elastic modulus and poisson's ratio for sample-27

The failure load of 115.2 kN was applied on sample 28, with peak strength of 65.16 MPa and giving 2227 micro strain of axial strain at failure. Figure 4.21 shows three essential parameters that were determined; unconfined compressive strength (UCS), secant and tangent Young's Modulus (E Sec and E Tan), and secant and tangent Poisson's Ratio (ν Sec and ν Tan) from sample number 28.

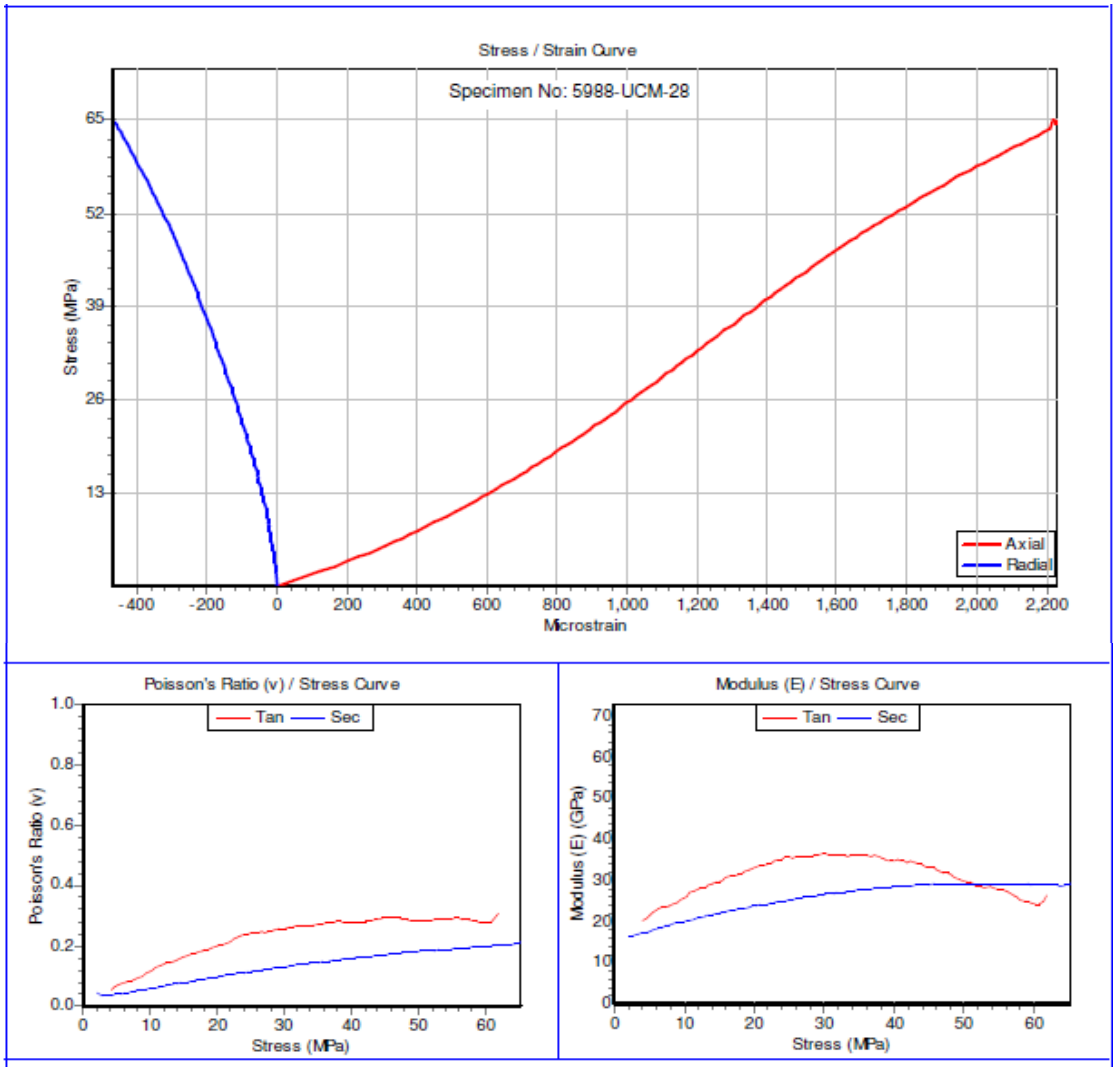

Failure Load: 115.2 kN | Peak Strength: 65.16 MPa | Axial Strain at Failure: 2227 microstrain

% Strength	Strength (MPa)	E Tan (GPa)	E Sec (GPa)	ν Tan	ν Sec
10	6.52	23.5	18.7	0.082	0.046
20	13	28.9	21.7	0.149	0.073
30	19.5	33.2	23.8	0.197	0.096
40	26.1	36	25.8	0.245	0.118
50	32.6	36.3	27.4	0.266	0.140
60	39.1	35	28.5	0.278	0.157
70	45.6	33.3	29.3	0.292	0.171
80	52.1	28.6	29.5	0.285	0.185
90	58.6	25.1	29.3	0.281	0.197

Figure 4.21 Uniaxial Compressive Strength test results with elastic modulus and poisson's ratio for sample-28

The failure load of 93.16 kN was applied on sample 29, with peak strength of 52.79 MPa and giving 2116 micro strain of axial strain at failure. Figure 4.22 shows three essential parameters that were determined; unconfined compressive strength (UCS), secant and tangent Young's Modulus (E Sec and E Tan), and secant and tangent Poisson's Ratio (ν Sec and ν Tan) from sample number 29.

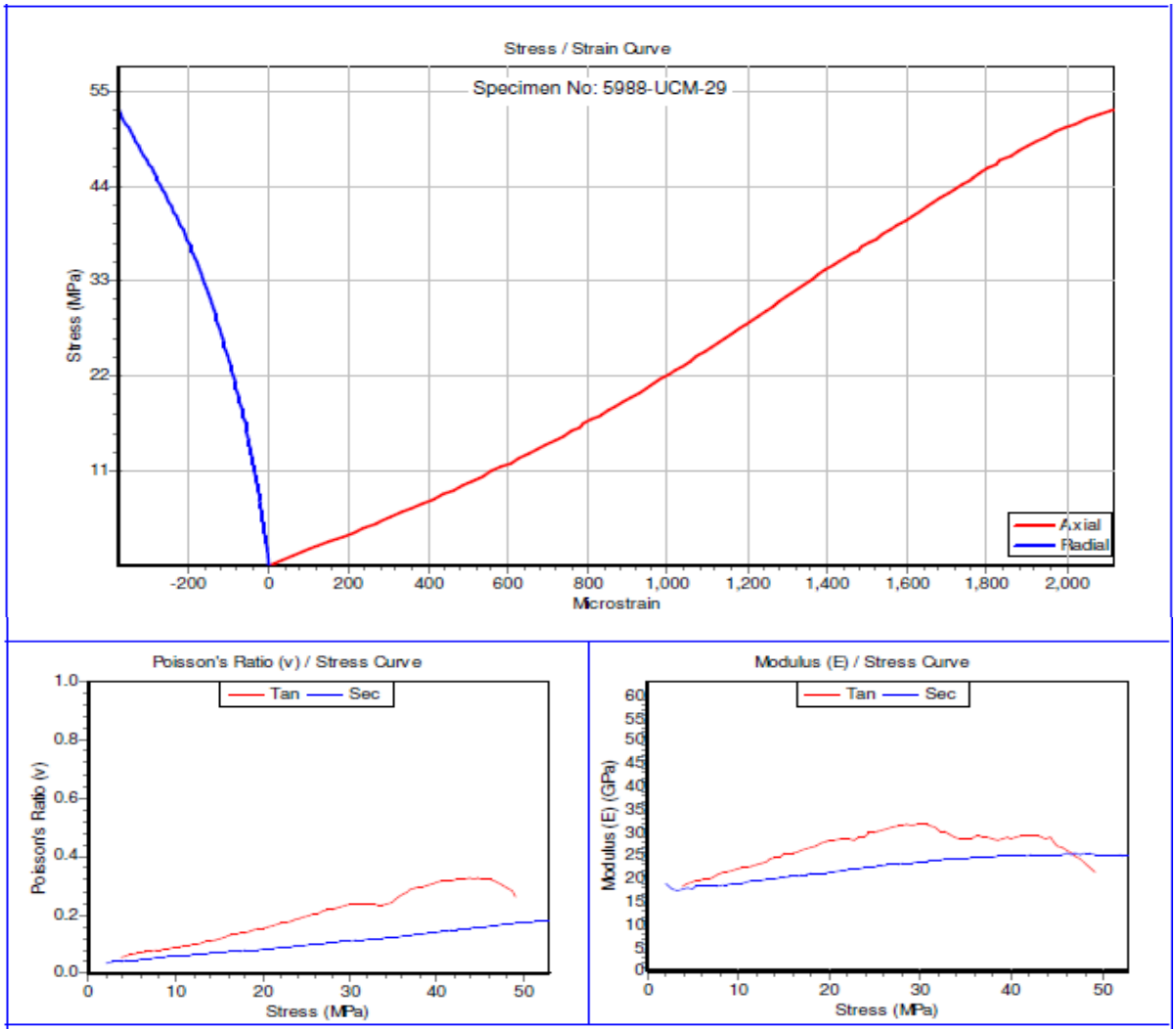

Failure Load: 93.16 kN | Peak Strength: 52.79 MPa | Axial Strain at Failure: 2116 microstrain

% Strength	Strength (MPa)	E Tan (GPa)	E Sec (GPa)	ν Tan	ν Sec
10	5.28	19.7	18.4	0.068	0.047
20	10.6	22.7	19.5	0.093	0.060
30	15.8	25.8	20.6	0.129	0.073
40	21.1	28.7	21.9	0.162	0.085
50	26.4	31.3	23.1	0.211	0.101
60	31.7	30.4	24.2	0.238	0.117
70	37	29.1	24.9	0.291	0.132
80	42.2	29.5	25.3	0.323	0.151
90	47.5	24.4	25.5	0.302	0.167

Figure 4.22 Uniaxial Compressive Strength test results with elastic modulus and poisson's ratio for sample-29

4.3.5 Triaxial Compressive Strength Test

When cylindrical rock specimen were placed in a specifically designed cell (Hoek cell) and subjected to different loads, each sample fail in accordance with its strength characteristics.On average, C quartzite gave the highest triaxial compressive strength (δ_1) value of 466 MPa and the dolomite with the lowest (δ_3) value of 173 MPa see Figure 4.23. A-Quartzite gave highest (δ_3) value of 30 MPa.

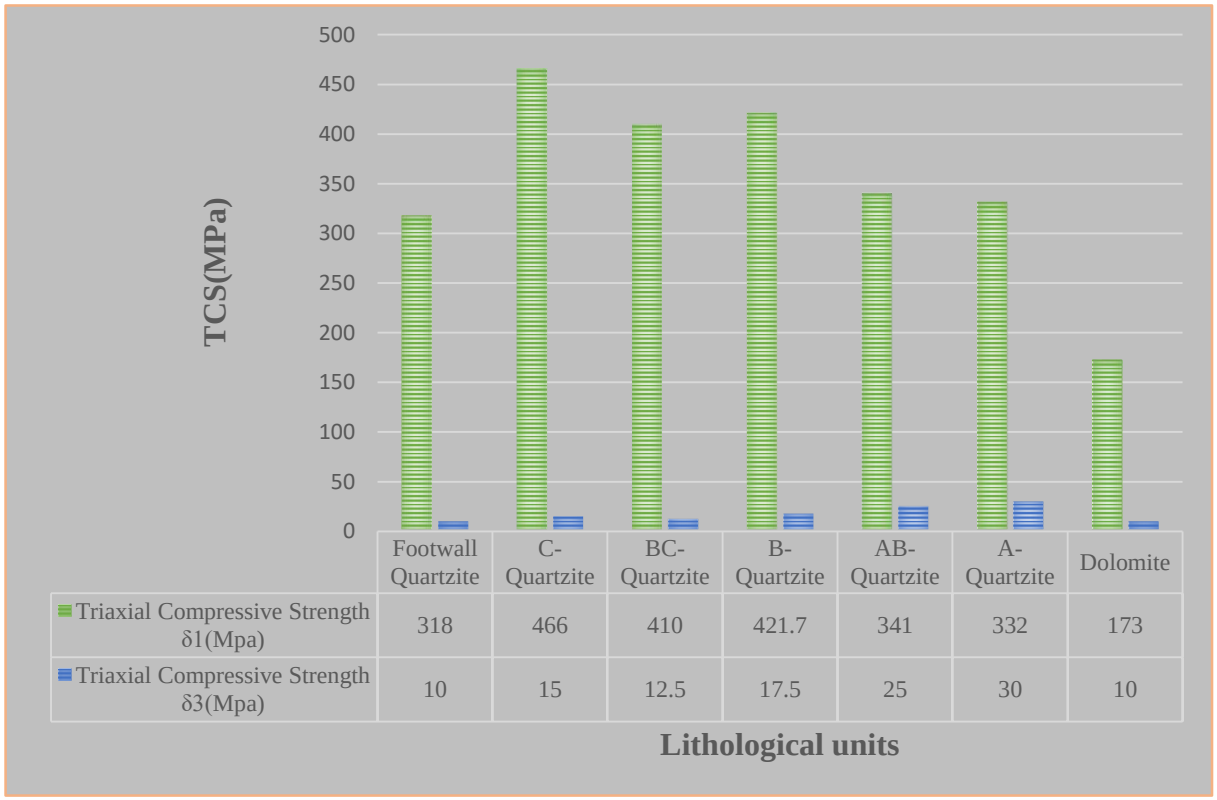

Figure 4.23 Average Triaxial Compressive Strength values (δ_1 and δ_3) (TCS) for Lithological units

4.4 DISCUSSION OF RESULTS

The behaviour and properties of the rock mass can be fundamentally assessed in three ways: laboratory testing, field observations and numerical modelling. The advantage of the laboratory tests is that there is a large amount of experimental control and it is relatively cheap.

The assumption made in the laboratory tests was that each rock specimen was the true representation of the rock mass from which it was taken.

The C Quartzite has the highest value of strength from all the three tests than other rock units because of higher levels of metamorphism which was enhanced during the mineralisation of this rock unit and it is about 85 percent made up of quartz mineral with hardness of 7 on the

Mohs hardness scale. Dolomite has the lowest strength value because of its soft carbonaceous mineral constituents.

The Uniaxial Compressive Strength (UCS) results show high Young's modulus values for Quartzite rock units than Dolomite showing that Quartzite has more tensile strength than Dolomite. This means that C Quartzite will require more stress for it to undergo failure than any other rock units at the mine and Dolomite is the weakest and will require minimal stress to experience failure.

The Rock Mass Rating (RMR) parameter for orebody and hangingwall rocks was determined according to Laubscher's (1990) Geomechanics classification (Table 4.1). RMR parameters were based on the measurement of discontinuity sets (Number and spacings) as well as the character of the discontinuity.

Table 4.1: Laubscher's Rock Mass Strength (RMS) rating of Mufulira rock formation

Rock type	(RMS) MPa	Class
Footwall quartzite	112	Good
C-quartzite	118	GIV Good
Inter B-C	94	Good
B-quartzite	89	GIV Good
Lower dolomite	15	FAIR
Inter A-B	126	Good
A-quartzite	164	GIV Good

According to the classification system used by the International Society for Rock Mechanics (ISRM — 1986 Rock Characterisation; Testing and Monitoring), the orebody quartzite are described as Extremely STRONG while the footwall and the hanging wall rocks are STRONG to Very STRONG. The exception is the Dolomite unit which forms the immediate hanging wall of the B orebody and is classified as Medium STRONG to STRONG as can be seen its low values of Brazilian test, UCS and TCS test results.

Due to high stress levels within 62 to 64 blocks, management at Mopani Copper mines has introduced additional cross-cuts termed as distressing cross-cuts. This idea is to develop more cross-cuts within reasonable proximities to reduce seismic activities within these zones.

This has increased the cost of production because more access areas are being developed to mine the same stope areas. Apart from that, additional support 'shortcreting' is being conducted

to enhance cross-cut and mining drive stability during stope blasting but at an additional cost too.

4.5 SUMMARY

This chapter outlined the research findings and discussed the results. The results were shown inform of tables, graphs, flow-charts as well as figures. The chapter also documented the research findings from case study of Mufulira underground mine (DEEPS SECTION). The characteristic properties of the rocks found at the mine were discussed based on the Brazilian, Uniaxial and Triaxial test results obtained from laboratory experiments. The chapter further outlined the benefits of incorporating geomechanical properties of the rocks found at the mine so that their nature of deformation was well understood.

The next chapter discusses the development of an early warning system that can predict rockbursts and rock induced displacements at Mufulira mine through modification of the earlier existing system.

CHAPTER FIVE: DEVELOPMENT OF AN EARLY WARNING SYSTEM TO PREDICT ROCKBURSTS AND ROCK INDUCED DISPLACEMENTS AT MUFULIRA MINE (DEEPS SECTION)

5.1 INTRODUCTION

This chapter discusses the results obtained after the establishment of an early warning monitoring system. The system's efficient or effectiveness will also be analysed. The effects of rock bursts and rock falls to the sequencing of mining development will also be discussed. Since the beginning of 1970s, Mufulira mine has been recording incidents of rockbursts and applying various efforts to find mitigation measures for rockbursts. For instance, an M2.8 rockburst occurred in the mining drive at 1440 meter level underground on 16 January, 2018. A severe damage of the mining drive and the cross-cut on 1490 mL occurred on 6th February 2020 and on 21st November, 2022, another rock burst incident occurred at 1490mL along C63 mining drive where the supporting machine belonging to mining contracting company Reliant Mining was buried. This section presents the current microseismic monitoring system used at the mine and its outputs, as well as discussing its effectiveness as the mine deepens.

In order to understand the mechanism of the rockburst, geotechnical steps must be taken (Aleksander et al., 2010). These include field geotechnical investigations which involves the installation of microseismic system (geophones) capable of detecting any slight movement in the rock mass, and stress analysis. Under field investigations, scan-line mapping of joints indicated six (6) major joint sets in the surrounding rock mass to the rockburst locations. Stress analysis showed high stresses of 200 MPa in the chain pillars and low stress concentration of 20 MPa at the rockburst sites during initial stages of mining.

5.2 EFFECTS OF ROCKBURSTS AND ROCKFALLS ON MINING SEQUENCE.

A review of the previously proposal to de-stress the historical remnants between 62 and 64 blocks was made and another one to de-stress the remnant pillars.

The area targeted for de-stress plan is located on 1473mL between 62 and 63 blocks. The stretch has a strike length of approximately 120 m (Figure 5.1 AB). Four (4) "De-stress" cross-cuts have been proposed to be mined off the footwall drive at an incline to attempt to reach the top boundary of the void created after the mining drive excavation damage. The void into which the cross-cuts are intended to hole is estimated not to be higher than 2.5 m above the

roof of the damaged mining drive (Figure 5.1) one of the scanned FoG area, the 1473 mL plan and sections showing the layout of the proposed option.

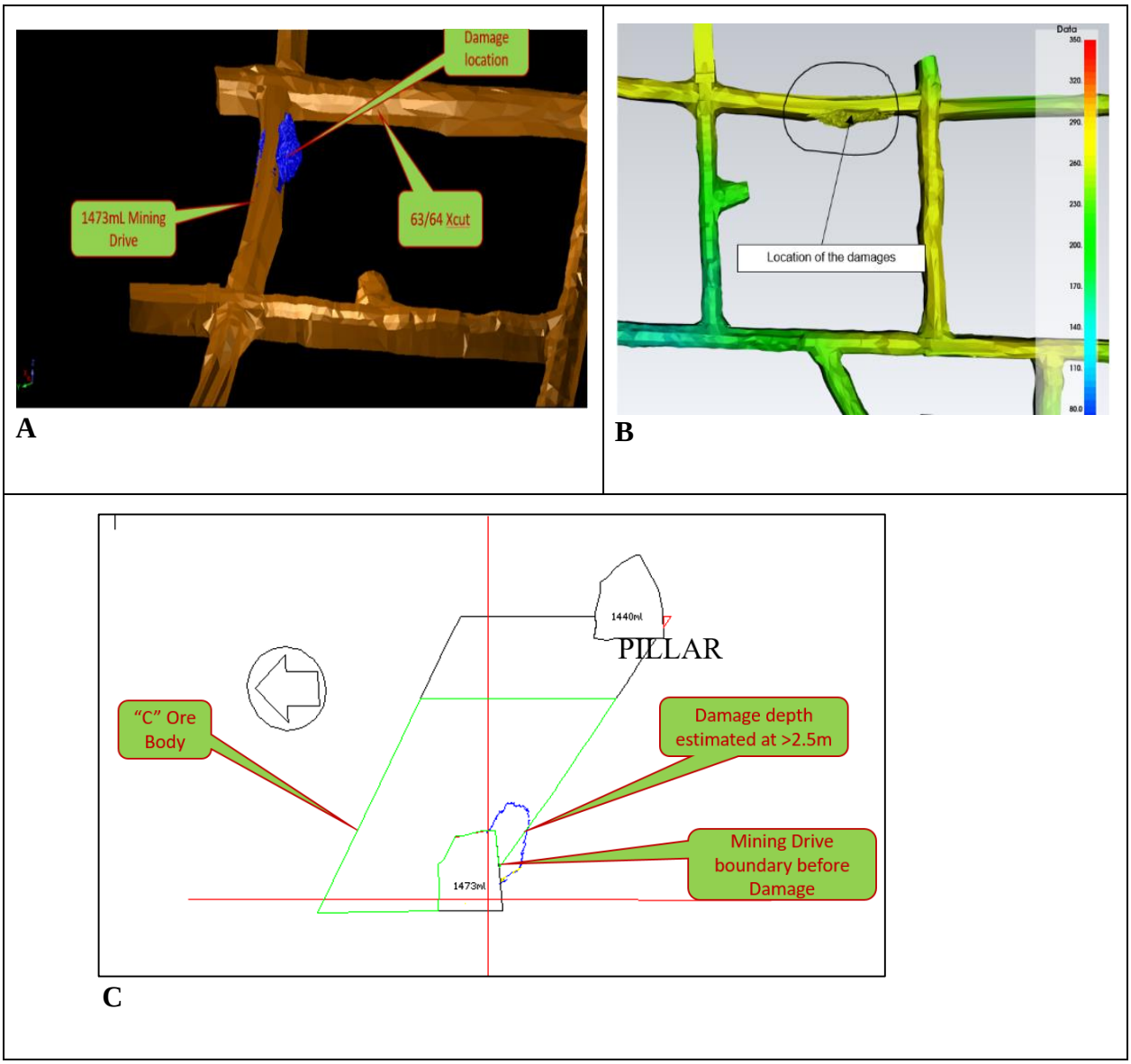

Figure 5.1: (A) 1473mL plan 3D scanned FoG area, (B) plan 3D tangential stress legend on scanned FoG area and (C) section boundary of the void

5.3 STRESS ANALYSIS ON ROCKMASS

The north cross-cuts was developed off the footwall drive located in relatively better footwall quartzite rockmass conditions and advance towards the orebody quartzite where adverse and potentially burst-prone conditions will be intercepted (Figure 5.2). Similar to the conditions in the existing cross-cuts, adverse ground conditions are anticipated at about 20 m before footwall contact of the C-orebody. The targeted area for de-stress was located in extremely high stress environment with major principal stress exceeding 100 MPa in many places. Figure 5.2 shows

snapshots of Map3D display of major principal stress results contours. The existing remains of the mining drive show that severe damage concentrated more on the southern side than the north and the roof. That made the method of holing into the void more practical as the fall-out depth into the roof does not exceed 3 m.

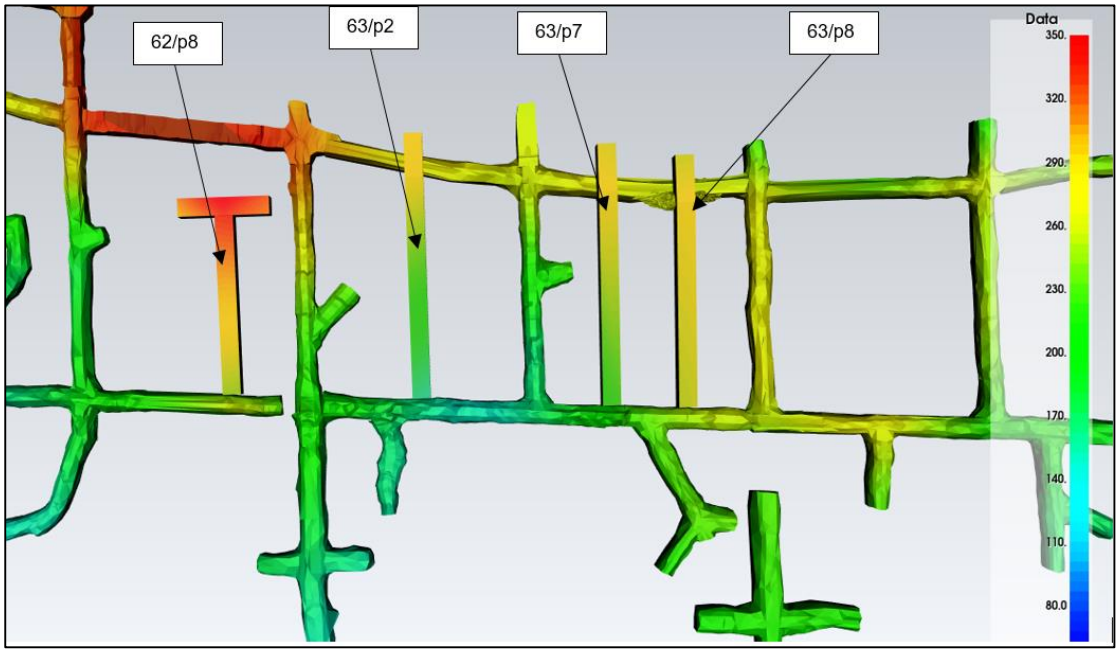

Figure 5.2 Display of the tangential stress (cross-cuts were mined from fair to adverse rockmass conditions-Tangential stress greater than 250 MPa

Precautions were taken to ensure that the blastholes were preserved from potential collapse/shearing. Efforts were made to ensure that only recommended maximum stable spans are excavated. The proposed cross-cuts were also expected to significantly interact with the existing cross-cuts when in the near field and cause increased excavation boundary stress. Well controlled blasting with application of smooth blastholes to expose undamaged excavation surface evidenced by half-hole barrel marks were strictly recommended. Special rock mechanics recommendations to ensure that the activities were undertaken under strict rock mechanics control were given.

5.4 DEVELOPMENT SEQUENCE AND GROUND SUPPORT

To continuously preserve the integrity of the rockmass surrounding the heading, fully reinforced and supported blast advances not exceeding 2 m are recommended within 20 m from the footwall contact. The headings are recommended to advance with in-cycle shotcrete application for every advance followed by welded mesh and splitsets and later cable anchors and/or shotcrete arches when they reach 10 m from the footwall contact. Standard ground

support for north cross-cuts and normal blast advance of 3 m are recommended only for the first 30 m in each cross-cut.

The headings are only recommended to advance after recommended full ground support is installed and inspected. The standard splitset installation installed in cross-cuts shall be applicable in the proposed cross-cuts after shotcrete application in the near field of stope influence (10 m from footwall contact)

At the stage where the headings reach an estimated distance of 10 m before the projected damage/collapse, a sufficient number of probe holes must be drilled to establish the actual boundaries of the void so that the next blasts can be guided. Depending on the conditions, blast advance may reduce further to allow safe holing and brow support. All excavation intersections will be supported with 6 m cable anchors at 1.5 m by 1.5 m. After holing, the intersection of the cross-cut with the existing damaged mining drive was filled with waste rock to create a new floor/platform where further development continued from.

5.5 MICROSEISMIC MONITORING SYSTEM AT MUFULIRA MINE

5.5.1 Introduction

The Microseismic monitoring system used at Mufulira mine just like in other mines, enables the quantification of exposure to seismicity and provides a logistical tool to guide the effort into the prevention and control of, and alerts to, potential rock mass instabilities that could result in rock bursts. Mendecki, et al., 2010 defined the following five specific objectives of monitoring the seismic response of the rock mass to mining: rescue of personnel, prevention, seismic hazard rating, alerts - including short term response to unexpected strong changes in certain parameters and back analysis to improve the efficiency of both the mine layout design and the monitoring process. A quantitative description of seismic events and of seismicity are necessary, but not sufficient, in achieving the above objectives.

In view of this, a more accurate and active early warning system must be developed to detect rockbursts and rockfalls earlier before they occur. The current microseismic monitoring system has been expanded through installation of geophones within reasonable proximity to mining blocks affected by seismic activities. Daily seismicity values were plotted on checklists and hotspot areas identified.

5.5.2 Microseismic Monitoring Checklist

The checklist Table 5.1 shows the multi-day seismometer status of the seismic network at Mufulira mine according to Institute of mining seismology of South Africa as of June 23rd to 29th, 2023. The green tick shows that the system was above 90% powered reference to the key below. Additionally, two more geophones have been installed at 1457 mL, 55P5 and another one at 1473 mL, 67P5.

Table 5.1: Multi-day seismometer status of the seismic network in June, 2023

Key

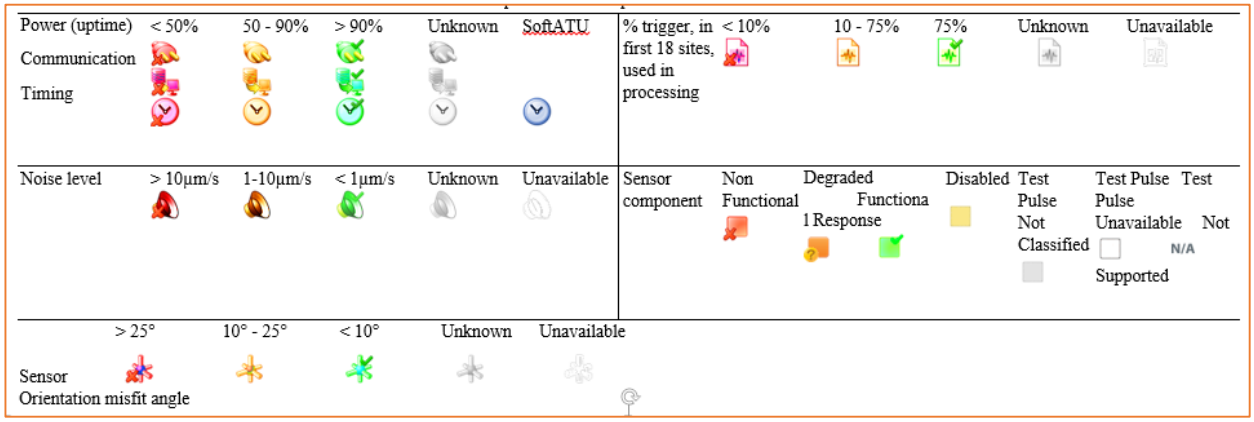

5.5.3 Location of microseismic events

The location of a seismic event is assumed to be a point within the seismic source that triggered the set of seismic sites used to locate it (Figure 5.3). The complexity of processes at the source,

however, may complicate the location of a seismic event. If a slow or weak rupture starts at a certain point, the closest site(s) may record waves radiated from that very point while others may only record waves generated later in the rupture process by a higher stress drop patch of the same source. One needs to be specific in determining the arrival times of different phases if the location of rupture initiation is sought, otherwise the location will be a statistical average of different parts of the same source. A reasonably accurate location is important for the following reasons:

a) To indicate the location of potential rock bursts.
b) All subsequent seismological processing, e.g. quantification of seismic sources, attenuation or velocity inversion, depends on location.
c) All subsequent interpretation of individual events depends on location, e.g. events far from active mining, close to a shaft or, in general, in places not predicted by numerical modelling, may raise concerns.
d) All subsequent interpretation of seismicity, e.g. clustering and specifically localization around planes, migration, spatio-temporal gradients of seismic parameters and other patterns are judged by their location and timing.

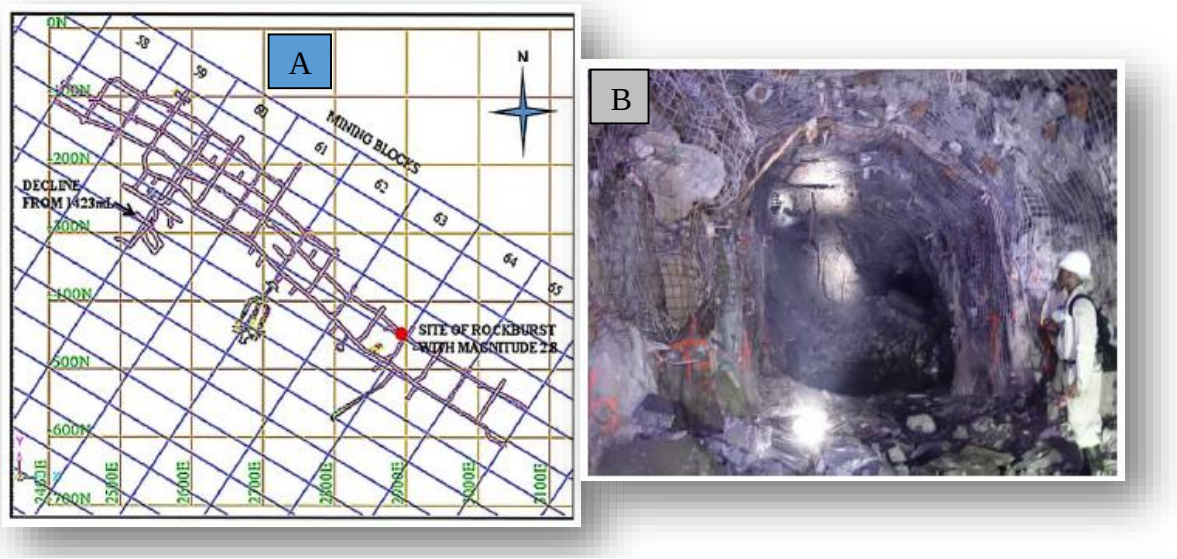

Figure 5.3: ***(A) site layout and (B) location of rockburst at 1440 mL (Sinkala, et al 2018)***

5.5.4 Seismic event plots

The peak ground velocity (PGV) which is the greatest speed of shaking recorded during a seismic event, are shown in Figures 5.4 and 5.6. Those events plot of the seismic activities occurred between 18th and 21st November, 2022 at Mufulira mine (DEEPS section) within seismically active mining blocks 61 to 64 and within the DEEPS section central blocks, according to the Institute of mine seismology of South Africa. The work places were coloured orange and red.

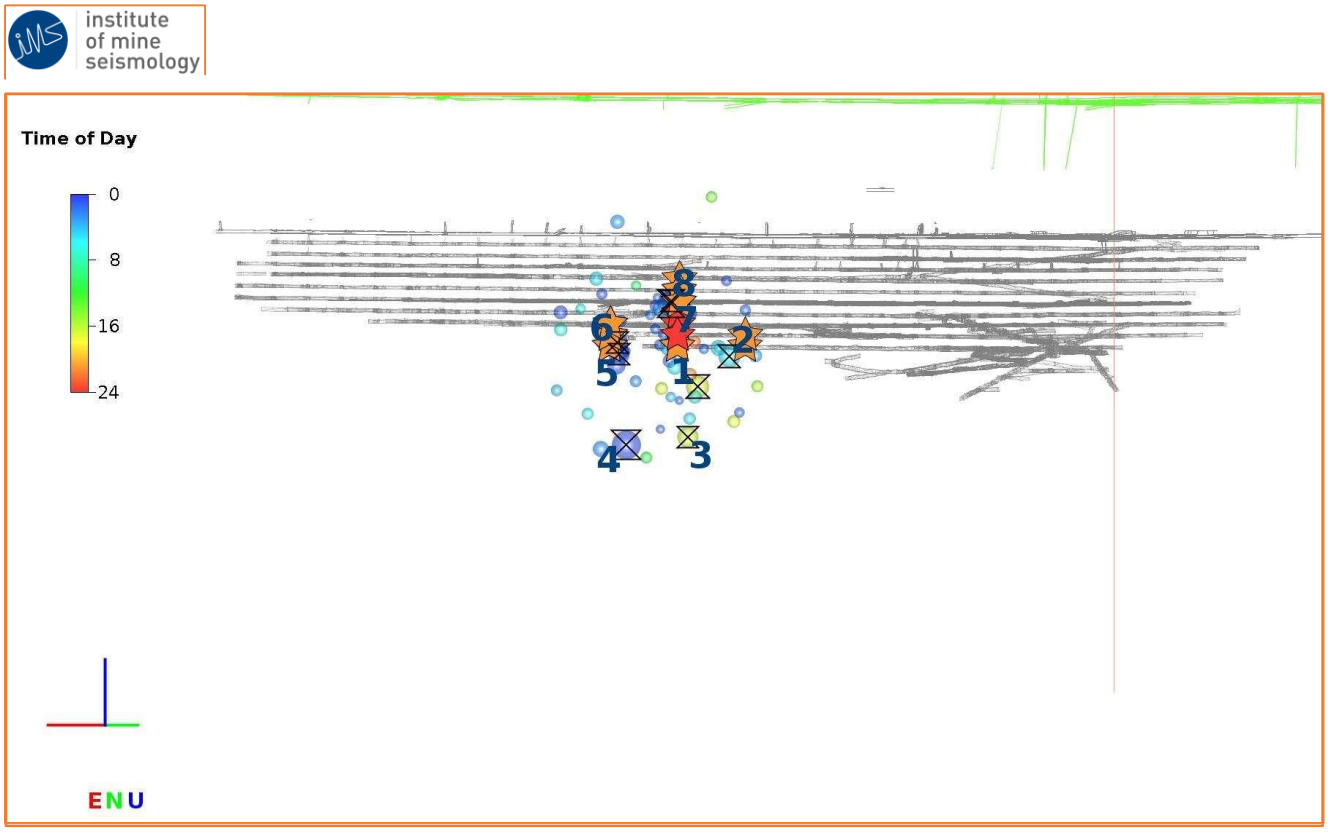

Figure 5.4. Showing PGV calculated using: logPGV = 0.3294 logP + 0.2196 logE - 1.0000 logR - 0.6439 for events from 18th to 21st November, 2022. Orange (50.0<=PGV [mm/s] <150.0) and Red (PGV [mm/s]>=150.0

5.5.5 Seismograms and Sensors

Some typical seismograms from micro-seismicity event recorded at the mine on 29th June, 2023 by the ISS system are shown in Figure 5.5. The large range of amplitude that must be recorded for these seismic events is evident: the small magnitude -2.0 event generates peak ground motions of about 10^{-6} m/s at 170 m from the source, while the magnitude +1.8 event generates

10^{-2} m/s at approximately the same sensor-source distance. For small events, the seismic signals are both high frequency and low in amplitude.

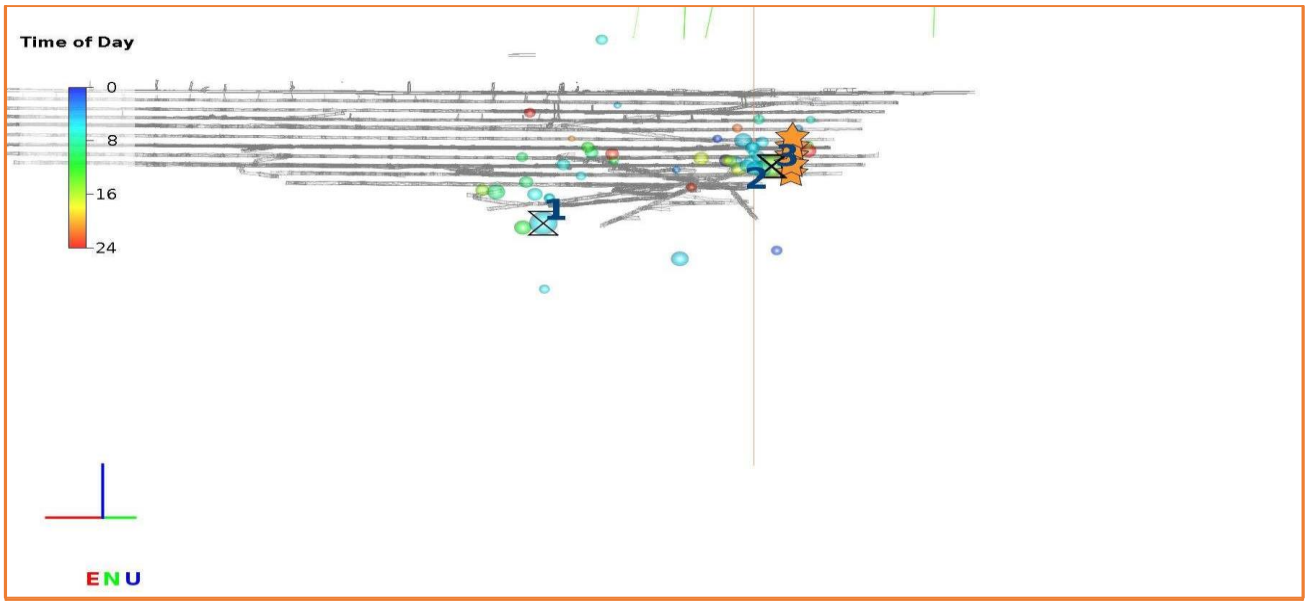

Figure 5.5 Showing PGV calculate using: logPGV = 0.3294 logP + 0.2196 logE - 1.0000 logR - 0.6439 for central blocks recorded between 18th and 21st November, 2023. Orange (50.0<=PGV[mm/s]<150.0) and Red (PGV [mm/s]>=150.0)

Borehole seismic sensors (geophones) are preferred at the mine, the sensors are grouted into holes 10 m in depth and of diameter of 76 mm. Figure 5.6 shows an IMS tri-axial 4.5 Hz borehole geophone. Such geophones have a linear response from 4 Hz to at least 2500 Hz. Passive electronics are fitted to the sensor after installation to provide a frequency dependent amplification. This results in an effective lower frequency response of about 3 Hz, and does not introduce any noise or distortion of the signals at higher frequencies.

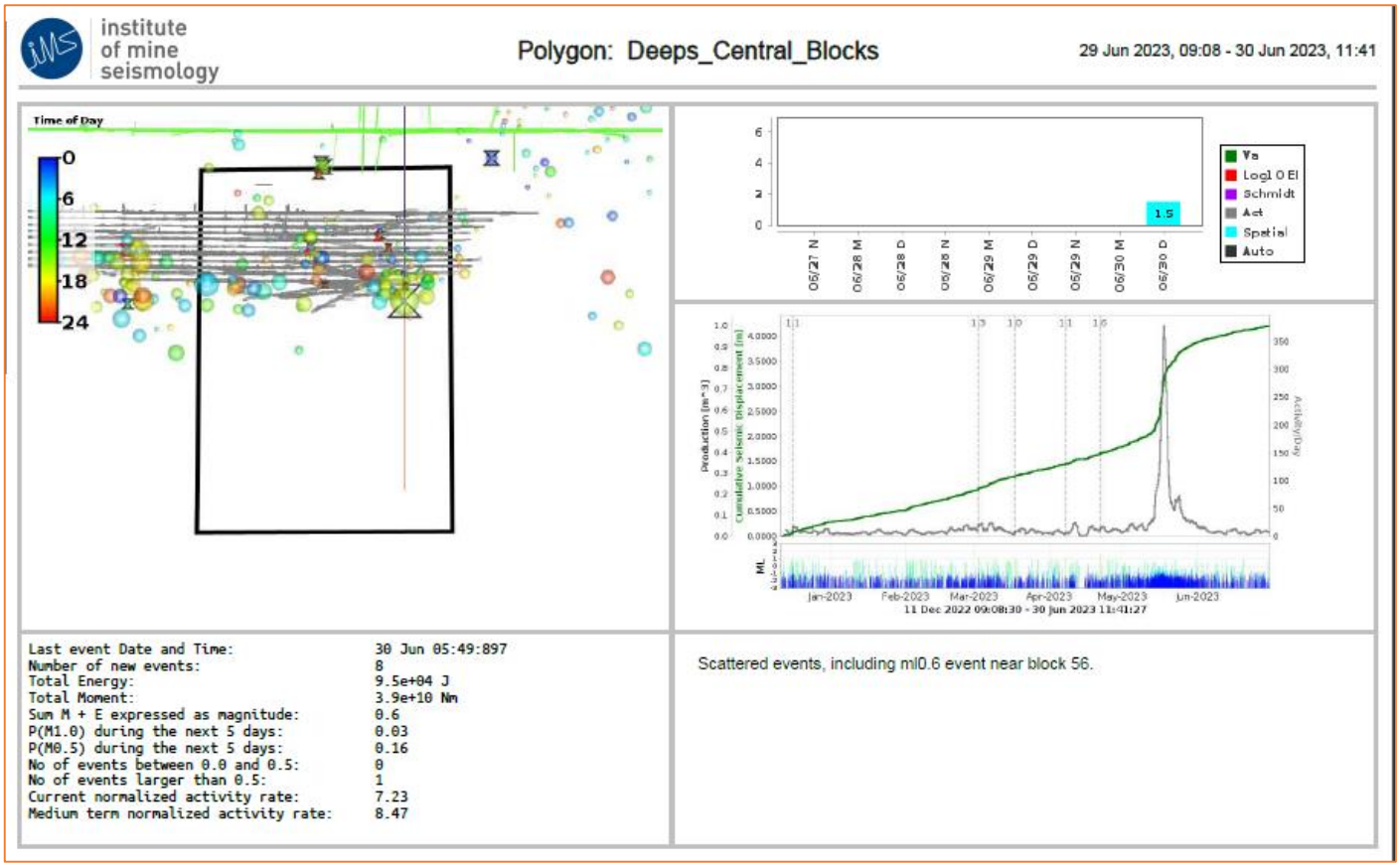

Figure 5.6 Showing seismograms from micro-seismicity event recorded at the mine by the mine by the ISS system courtesy of Institute of mine seismology

5.5.6 Developed Flow Chart of Modified Seismic Monitoring System for Predicting and Monitoring Rock Bursts and Rock Displacements

Figure 5.7 shows a modified installation of Microseismic Monitoring System from underground the mine to surface station. The previous Microseismic Monitoring System had geophones installed very far from the seismically active mining blocks. This resulted in delays to pick up rock vibrations by seismic sensors (geophones) from the active mining blocks In view of this, a well modified monitoring system has been installed and tested at 1457 mL, 55P5 and 1473 mL, 67P5 which is closer to seismically active mining blocks of 62 to 64 blocks within 1457 mL, 1473 mL, 1490 mL and 1507 mL levels where mining activities are taking place. The addition of these sensors to the already existing ones located in far areas will reduce travel distance for rock vibrations before being picked up by the geophones. The accuracy in determining seismic activity locations has also improved (Table 5.1). On 19 March, 2023 an

event of M1.0 was recorded at 1473 mL block 55 by the new system. The location of the modified flow chart is supported by laboratory findings that indicate that high values of Brazilian (Tensile strength) ranging from 7 MPa to 12.1 MPa, Uniaxial Compressive Strength

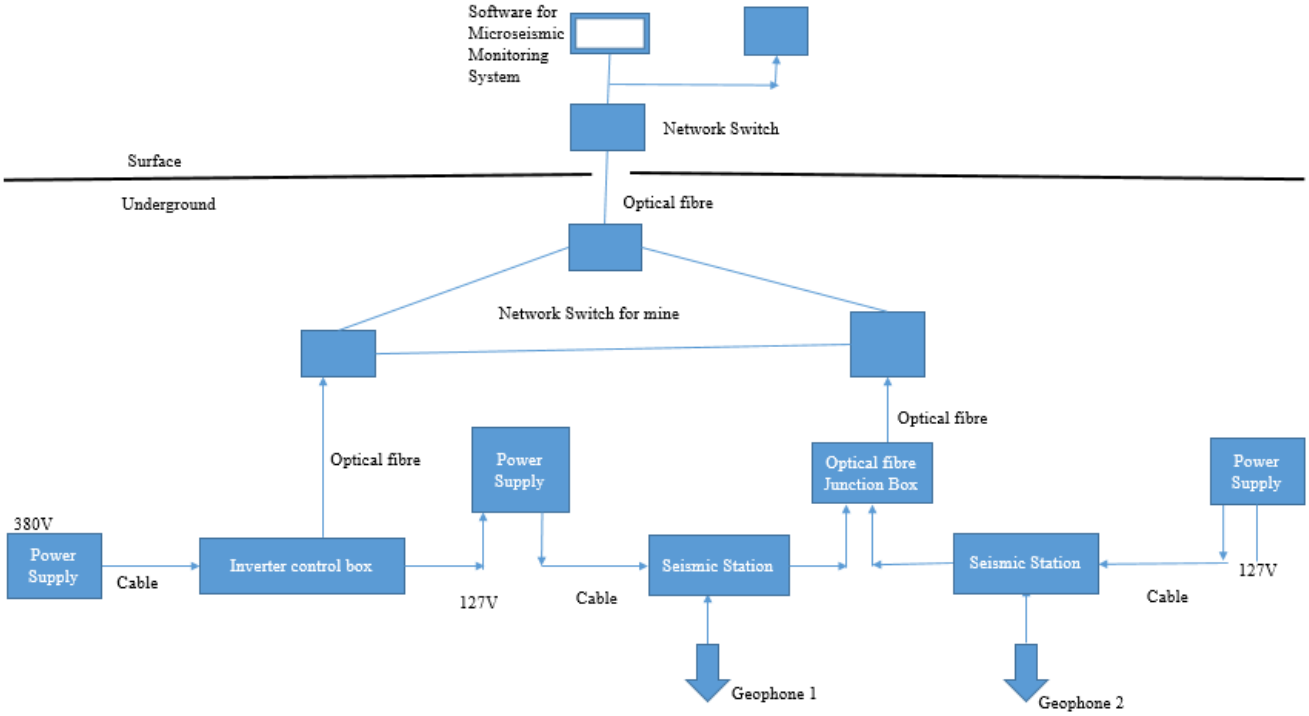

Figure 5.7: Developed flow chart of modified micro-seismic monitoring system for predicting and monitoring rock bursts and rock displacements.

(UCS) ranging from 126 MPa to 226 MPa and Triaxial Compressive Strength ranging from 124 MPa to 466 MPa were obtained. The laboratory results show that rocks in these seismically active blocks have high tensile strengths and undergoes brittle type of deformation, hence any rock burst or rock fall will be detected to enhance safe mining in these blocks based on the modified Micro-seismic Monitoring System. Based on the earlier obtained results from geological and geotechnical mapping, the rocks found in the seismically active mining blocks are highly brittle. Therefore, by bringing geophones closer to these blocks will allow any rock sliding along the secondary structures to be picked and recorded as seismic activities.

5.6 SUMMARY

The chapter discussed development of an early warning monitoring system through modification of the already existing micro-seismic monitoring system by installation of two geophones in series within seismically active mining blocks and connected to the network system via optical fibre junction box. The geomechanical properties of rocks within the 62 to

64 blocks were used to determine actual placement of geophones within the blocks and improved on the pick-up time for any given seismic event.

The next chapter seeks to conclude and provide recommendations based on the research.

CHAPTER SIX: CONCLUSION AND RECOMMENDATIONS

6.1 CONCLUSION

This study was aimed at developing an early warning system to predict and monitor rock bursts and rock displacements in seismically active mining blocks using geomechanical properties of rocks. The development of distressing cross-cuts accompanied by additional support technics such as shotcreting have also improved the safety levels around the seismically active mining blocks.

1. The three sub-objectives were achieved through conducting geotechnical and geological mapping within 62 to 64 blocks. The discing observed in the drilled core also shows that stress levels have increased as the mine deepens. This increase in stress can affect the meta-sediment footwall Quartzite and orebody Quartzite allowing them to undergo brittle deformation.

2. Based on laboratory findings, it has been established that the high values of Brazilian (Tensile strength) ranging from 7 MPa to 12.1 MPa, uniaxial compressive strength (UCS) ranging from 126 MPa to 226 MPa and triaxial compressive strength ranging from 124 MPa to 466 MPa have the potential to induce premature failure and rock bursts. The high values of Young's modulus also show that the rocks have high tensile strength (25 GPa) because of 80% quartz mineral present in them, except Dolomites which are not present in mine haulages but found in stope areas where they are found as hanging of the B orebody.

3. The study has developed a modified micro-seismic monitoring system at Mufulira Mine (DEEPS) section using geomechanical properties of rocks to suitably position the geophones is the affected mining blocks to record seismic events. The additional installed geophones in more proximity areas to the seismically active mining blocks will enhance the system's efficiency in recording rock bursts and rock falls by quickly picking up of any slight vibration, thereby making mining within the 62 to 64 blocks safer than before. This modified micro-seismic monitoring system is susceptible to change if mining locations change due to changes in geotechnical and geological parameters such as rock types, jointing and fracturing.

6.2 RECOMMENDATIONS

1. An acoustic emission intelligent real-time monitoring system must also be installed at Mufulira mine (DEEPS section) to assist the current micro-seismic monitoring system as an early warning system.
2. The current micro-seismic monitoring system information must be processed locally to reduce costs for the mine.
3. All the mining activities occurring in the seismically active mining blocks must employ sophisticated technology such as remote loaders to avoid loss of life or injuries and machine damage from rock bursts and rock falls.

6.3 LIMITATIONS OF STUDY

The limitations of laboratory tests wer the small size of the specimen and the consequent overestimation of the rock mass properties.

The locations of geophone installation sites could have been closer to the development faces as possible. However, limitations are that seismic sensors (geophones) should be away from active blasting faces such as stopes and other active mining ends to avoid damaging the seismic monitoring equipment during blasting.

The establishment of seismic stations are also limited to funk holes to avoid possible damage by underground heavy mobile equipment such as loaders and dump trucks.

REFERENCES

A Cichowicz, SM Spottiswoode, LM Linzer, D Drent, PS Heyns, and MF Handley. (2005). Improved seismic locations and location techniques. University of Pretoria, South Africa.

Aki. K, and Paul G. R. (2009). Quantitative seismology, 2nd ed. University Science Books Mill Valley, California, USA.

Aki, K. (1966), Generation and propagation of G waves from the Niigata earthquake of June 16, 1964. Part 2: Estimation of earthquake moment, released energy, and stress strain drop from the G-wave spectrum, Bulletin Earthquake Research Institute Tokyo University, 44, 73–88.

Aki, K., and P. G. Richards (2002), Quantitative seismology, 2nd ed., University Science Books, California.

Alam, B. A. K. M., M. Niioka, Y. Fujii, D. Fukuda and J. Kodama (2014). Effects of confining pressure on the permeability of three rock types under compression. *International Journal of Rock Mechanics and Mining Science.* 65: 49-61.

Aleksander J. M., Richard A. L. and Dmitriy A. M. 2010. Routine micro-Seismic Monitoring in Mines Institute of Mine Seismology, Australian Earthquake Engineering Society 2010 Conference Perth, Western Australia.

Backus, G. E., and M. Mulcahy (1976), Moment tensor and other phenomenological descriptions of seismic sources. 1. Continuous displacements, Geophysics. J. R. Astron. Soc., 46, 301–329.

Ben-Menahem, A., and S. J. Singh (1981), Seismic Waves and Sources, Springer-Verlag, New York.

Ben-Guo H., Z. Ravit, H.H. Yossef and F. Xia-Ting. 2015. Rockburst Generation in Discontinuous Rock Masses. *Rock Mech Rock Eng*. DOI 10.1007/s00603-015-0906-8.

Brandit, R. T. (1962). Relationship of mineralization to sedimentation at Mufulira, Northern Rhodesia. *Institution of mining and metallurgy.* Vol. 71, 459-479.

Brune, J. N. (1968), Seismic moment, seismicity and rate of slip along major fault zones, Journal of Geophysical Research, 73, 777–784.

Chloe A. 2020. Theoretical geomechanics. Georgia Institute of Technology, 53-108.

Crouch, S. L. and C. Fairhurst (1973). The Mechanics of Coal Mine Bumps and the Interaction between Coal Pillars, Mine Roof and Floor, U.S.B.M. *Contract report*, H0101778.

Crouch, S.L. (1976). Analysis of stress and displacements around underground excavations: an application of the displacement discontinuity method. *Tech. Rep., Department of Civil and Mineral Engineering, University of Minnesota, 89-150.*

Dubinski, J., and K. Stec (2001), Relationship between focal mechanism parameters of mine tremors and local strata tectonics, in Proceedings of the 5th international symposium on rockbursts and seismicity in mines, edited by G. van Aswegen, R. J. Durrheim, and W. D Ortlepp, pp. 113–118, South African Institute of Mining and Metallurgy.

Fei, L., M. Tianhui, T. Chun'an and C. Feng. (2018). Prediction of rockburst in tunnels at the Jinping II hydropower station using microseismic monitoring technique. *Journal of Tunnelling and Underground* Space Technology. 81:480–493.

Fujii, Y., Y. Ishijima and G. Deguchi (1997). Prediction of coal face rockbursts and microseismicity in deep longwall coal mining. *International Journal of Rock Mechanics and Mining Science*. Vol. 34, No. 1, 85-96.

Fujii, Y., R. Balusu, G. Deguchi and Y. Ishijima (2001). Numerical simulation on microseismicity due to mining at one of the Collieries in Australia. *20th Int. Conference on Ground Control in Mining*, 9 Aug 2001.

Hoek, E. and E.T. Brown (1980). Underground excavations in rock. *The Institute of Mining and Metallurgy, London, pp. 527.*

Hudson, J. A. and J. P. Harrison (2000). *Engineering rock mechanics: part 2 illustrative worked examples*. Elsevier Science Ltd: Oxford, 95-109.

Hu J., Li J. G., Long Q. M., et al. (2015). Research on relevance of acoustic emission characteristic parameters based on R-Type clustering analyses. Mining safety and environmental protection, 42(4):52-55.

ISRM, (1979). Suggested Methods for Determining the Uniaxial Compressive Strength and Deformability of Rock Materials. International Journal of Rock Mechanics and Mining Sciences & Geomechanics Abstracts. 16-26.

Jiangong L. (2020). Research on the application of acoustic emission intelligent monitoring and early warning technology for the coal-rock dynamic disasters in underground mining faces. *IOP Conf. Ser.: Earth Environ. Sci.*

Kaiser, P.K. and M. Cai. (2012). Design of rock support system under rockburst condition. Journal of Rock Mechanics and Geotechnical Engineering. 4 (3): 215– 227.

Kristoffer B. & Daniel G. (2014), 'Challenges with deep mining, Case studies at Mindola and Mufulira underground mines, Zambia' pp. 15-50.

Long An, Changyu Jin, Dong Liu, Chenggong Ding & Xinghang Dai (2018) Mechanism of core discing in the relaxation zone around an underground opening under high in situ stresses. Bull Eng Geol Environ 77, 1179–1189.

Lynch, R., and A. Mendecki (2004), Gap601a: Experimental and theoretical investigations of fundamental processes in mining induced fracturing and rock instability close to excavations - research project for safety in mines research advisory council, Tech. rep., ISS International Limited.

Lynch, R., and A. J. Mendecki (2001), High-resolution seismic monitoring in mines, in Proceedings of the 5th International Symposium on rockbursts and seismicity in mines, Johannesburg, South Africa, edited by G. van Aswegen, R. J. Durrheim, and W. D. Ortlepp, pp. 19–24, South African Institute of Mining and Metallurgy.

Lynch, R., R.A..and Wuite, B. Smith, and A. Cichowicz (2005), Microseismic monitoring of open pit slopes, in Rockbursts and Seismicity in MInes 6, Perth, edited by Y. Potvin and M. Hudyma, Australian Centre for Geomechanics.

Lynch, R. A. (2010), Keynote address: Passive and active microseismic monitoring in mines, in Proceedings of the 5th Deep and High Stress Mining Seminar, Santiago, Chile.

Manchao, H., X. Hongman, J. Xuena, G. Weili, Z. Fei and L. Kangyuan. 2012. Studies on classification, criteria and control of rockbursts. Journal of Rock Mechanics and Geotechnical Engineering. 4(2): 97– 114.

Mikula, P. A. (2005), The practice of seismic management in mines – how to love your seismic monitoring system, in Rockbursts and seismicity in mines: Proceedings of the 6th International Symposium, edited by Y. Potvin and M. Hudyma, Australian Centre for Geomechanics.

Mountfort, P., and A. J. Mendecki (1997), Seismic transducers, in seismic monitoring in mines, edited by A. J. Mendecki, 1 ed., chap. 1, pp. 1–20, Chapman and Hall, London.

Muller, W. (1991). Numerical simulation of rock bursts. *Mining Science Technology*. 12(1):27–42.

Ng'ambi, I and Mutambo, V. (2016). Optimization of stope recovery and dilution at Mufulira mine through application of appropriate designs and practices. *International Journal of Applied Research.* 2(9). 397-402.

Ortlepp W.D. and T.R. Stacey. (1994). Rockburst mechanisms in tunnels and shafts. *Journal of Tunnelling and Underground Space Technology*. 9(1):59–65.

Seyed M. D., Neil B., Ákos T., Abolfazl T. and Balázs V., 2020. Australian Geomechanics, volume 55. Budapest University of Technology and Economics, Budapest, Hungary 2 Gecko Geotechnics Pty Ltd, Perth, Australia

Sheng-Jun, M., C. Mei-Feng, G. Qi-Feng and H. Zheng-Jun. 2016. Rock burst prediction based on in-situ stress and energy accumulation theory. International Journal of Rock Mechanics and Mining Science. 83:86–94

Sinkala, P., Nishihara, M., Fujii, Y., Fukuda, D. and Kodama, J. & Chanda E. (2019) Investigation of rockburst in deep underground mines, A case study of Mufulira mine, Copperbelt, Zambia. ARMA, American Rock Mechanics Association. 3:6-10

Siyanda B. (2015). Integrated petrographic, geomechanical and seismological studies of rockmass behaviour during the extraction of the Cooke 4 shaft pillar. PP. 29-67

Suorineni F. T. (2013), “Geomechanics Challenges and its Future Direction – Food for Thought”, Ghana Mining Journal, pp. 14 - 20.

Tian-Hui, M., T. Chun-An, T. Shi-Bin, K. Liang, Y. Qun, K. De-Qing and Z. Xu. (2018). Rockburst mechanism and prediction based on microseismic monitoring. International Journal of Rock Mechanics and Mining Science. 110:177–188.

Voinov, K. A., and V. G. Selivonik (1998), Estimation of stresses and mobility of structural blocks according to processing of mechanisms of seismic event sources, in Mining Geophysics, pp. 86–91, VNIMI.

Wen G.C, Li J.G, Zou Y.H, et al. 2011. Preliminary study on the application conditions of acoustic emission monitoring dynamic disasters in coal and rock. Journal of China Coal Society, 36(2):278-282.

Wen .G.C, Li J. G., Yang .H.M, et al. 2010. Theory analysis and experimental study on propagation laws of acoustic emission in coal and rock. In: 2010 International Conference on Mine Hazards Prevention and Control. Qingdao. Pp.757-763.

Wyss, M., and J. N. Brune (1968), Seismic moment, stress and source dimensions for earthquakes in the California-Nevada region, Journal of Geophysical Research, 73, 4681–4694.

Younga, S. L., and Y. V. Fedotova (2000), Study of source mechanisms of low energy seismic events in khibiny massif, in Proceedings of the All-Russian Geodynamics and Technogenesis meeting, pp. 171–174

Zhang, L. and H. H. Einstein (2004). Using RQD to estimate the deformation modulus of rock mass. International Journal of Rock Mechanics and Mining Science. Vol. 36, No. 5, 337-342.

Zou Y. H., Wen G.C, Hu Q.T., et al. 2004. Theory analysis and experimental study of the spread and attenuation of acoustic emission in rock body. Journal of China Coal Society, 29(6):663-667.

Zou Y. H. 2007. Study of AE signal propagation mechanism of rock and coal. Qingdao: Shandong University of Science and Technology, Pp.1-133.

APPENDIX

Table A.0-1 Results of uniaxial compressive strength tests with modulus & poisson's ratio measurements by means of strain gauges

					SPECIMEN DIMENSIONS					SPECIMEN TEST RESULTS							
Sampl #.	Borehole No	Depth		Lithology Unit	Diameter mm	Height mm	Ratio of Height to Diameter	Mass g	Density g/cm³	Failure Load kN	Strength (UCS) MPa	Tangent Elastic Modulus @ 50% UCS GPa	Secant Elastic Modulus @ 50% UCS GPa	Poisson's Ratio Tangent @ 50% UCS	Poisson's Ratio Secant @ 50% UCS	Linear Axial Strain at Failure mm/mm	Failure Code
		From(m)	To(m)														
UCM-01	NSX005	7.1	7.32	FWQ	47.31	131.5	2.8	622.82	2.69	222.3	126.5	53.3	38.5	0.51	0.21	0.0032	XB
UCM-02		7.83	7.7	FWQ	47.27	124	2.6	579.54	2.66	288.2	164.2	66.6	46.8	0.3	0.14	0.0031	XB
UCM-03		8	8.31	FWQ	47.33	128	2.7	604.5	2.68	233.9	132.9	55.4	39.7	0.47	0.22	0.0032	XB
UCM-04		8.31	8.63	FWQ	47.21	128.5	2.7	603.4	2.68	235.8	134.7	56.9	41.9	0.4	0.18	0.0032	XB
UCM-05		10.2	10.66	FWQ	47.33	122.5	2.6	571.64	2.65	313.1	178	68.5	50.3	0.28	0.16	0.0032	XA
UCM-06		18.55	18.88	CQ	47.7	128.3	2.7	602.16	2.63	437.9	245	70.3	59.7	0.27	0.19	0.0041	XB
UCM-07		24.15	24.43	CQ	47.87	128.6	2.7	625.69	2.7	260.5	144.7	53.7	46.7	0.41	0.2	0.0031	XA
UCM-08		24.43	24.74	CQ	47.87	134	2.8	652.29	2.7	276.2	153.5	50.4	40.5	0.45	0.21	0.0039	XA
UCM-09		28.1	28.41	BCQ	47.96	127.7	2.7	620.5	2.69	228.4	126.4	45.5	32.3	0.48	0.17	0.0036	XB
UCM-10		28.41	28.67	BCQ	47.79	129.6	2.7	635.13	2.73	213.3	118.9	46.1	38	0.4	0.2	0.0031	XA
UCM-11		40.15	40.5	BCQ	47.55	122.6	2.6	604.11	2.77	199.6	112.4	52.2	40.3	0.39	0.2	0.0026	XA
UCM-19		85.65	85.88	BQ	47.37	124.7	2.6	581.57	2.65	394	223.6	67.5	50.9	0.41	0.22	0.0039	XA

UCM-24		157.2	157.47	LDOL	47.47	126.4	2.7	615.82	2.75	60.6	34.2	28.6	19.9	0.15	0.1	0.0014	4B
UCM-25		163.1	163.39	ABQ	47.5	123	2.6	592.07	2.72	134.9	76.1	41.7	29.5	0.24	0.11	0.0023	3B
UCM-26		164.12	164.54	AQ	47.46	122.6	2.6	582.06	2.68	267.5	151.2	51	43	0.31	0.21	0.0034	YA
UCM-27		164.98	164.33	AQ	47.49	126.1	2.7	608.91	2.73	157	88.6	37.6	25.5	0.34	0.12	0.0036	2B
UCM-28		165.5	165.83	DOL	47.45	128.7	2.7	617.84	2.71	115.2	65.1	36.3	27.4	0.27	0.14	0.0022	3B
UCM-29		165.83	166.1	DOL	47.4	122.3	2.6	587.23	2.72	93.2	52.8	31.3	23.1	0.21	0.1	0.0021	4B

Table A.0-2 Results of Brazilian tensile strength tests

SPECIMEN PARTICULARS					SPECIMEN DIMENSIONS				SPECIMEN TEST RESULT		
Sampl#	Borehole number	Depth		Lithology	Diameter	Height	Mass	Density	Failure Load	Brazilian Tensile Strength	Note
		From.. m	o.. m	Unit	mm	mm	gram	g/cm³	kN	MPa	
UTB-12A	NSX005	41.15	41.55	BSS	47.60	24.84	118.6	2.68	18.89	10.2	
UTB-12B					47.54	24.85	117.8	2.67	21.66	11.7	
UTB-13A	NSX005	55	55.38	BSS	47.44	25.21	117.2	2.63	15.91	8.5	
UTB-13B					47.33	24.74	116.5	2.68	16.84	9.2	
UTB-14A	NSX005	60.57	60.96	BSS	47.40	24.65	116.8	2.69	16.76	9.1	

UTB-14B					47.45	24.68	116.9	2.68	17.10	9.3	
UTB-15A	NSX005	62.97	63.25	BSS	47.26	24.50	114.1	2.65	16.89	9.3	
UTB-15B					47.36	24.46	113.6	2.64	17.90	9.8	
UTB-20A	NSX005	91.96	92.28	BQ	47.63	25.14	115.6	2.58	19.68	10.5	
UTB-20B					47.57	24.75	114.6	2.60	20.32	11.0	
UTB-21A	NSX005	97.2	97.5	BQ	47.24	24.88	115.6	2.65	22.93	12.4	
UTB-21B					47.24	24.84	115.9	2.66	22.00	11.9	
UTB-22A	NSX005	110.97	111.25	BQ	47.32	24.97	116.2	2.65	21.76	11.7	
UTB-22B					47.28	24.75	113.1	2.60	20.59	11.2	
UTB-23A	NSX005	111.25	111.54	BQ	47.18	24.93	115.8	2.66	20.56	11.1	
UTB-23B					47.05	24.85	114.4	2.65	22.14	12.1	
UTB-38A	NSX007	35.65	36.00	LCON	47.13	24.61	114.7	2.67	14.59	8.0	
UTB-38B					47.09	24.71	117.8	2.74	14.11	7.7	
UTB-38C					47.08	24.95	117.1	2.70	16.85	9.1	
UTB-39A	NSX007	39.5	39.8	LCON	47.07	24.75	115.2	2.68	17.00	9.3	
UTB-39B					47.17	24.41	116.0	2.72	16.58	9.2	

Table A.0-3 Results of Triaxial compressive strength tests

SPECIMEN PARTICULARS					SPECIMEN DIMENSIONS					SPECIMEN TEST RESULTS				
Samp#	Borehole Number	Depth		Lithology Unit	Diameter mm	Height mm	Ratio of Height to Diameter	Mass g	Density g/cm³	Confining Pressure δ3 MPa	Failure Load P kN	Strength (TCS) δ1 MPa	Failure Mode	Note
		From.. m	To.. m											
TCS-16-A	NSX005	63.25	63.51	BQ	47.46	93.4	2.0	448.3	2.71	5.0	227.18	128.4	5B	
TCS-16-B					47.29	90.0	1.9	431.3	2.73	10.0	305.34	173.8	XA	
TCS-17-A		74.23	74.56	BQ	47.31	89.6	1.9	425.5	2.70	15.0	448.92	255.4	XA	
TCS-17-B					47.30	94.7	2.0	446.9	2.69	20.0	600.37	341.7	XA	
TCS-18-A		74.56	74.90	BQ	47.36	94.0	2.0	446.6	2.70	25.0	527.46	299.4	XA	
TCS-18-B					47.41	93.1	2.0	442.5	2.69	30.0	586.32	332.1	XA	
TCS-30A	NSX007	8.00	8.30	BQ	47.32	101.1	2.1	472.8	2.66	2.5	367.95	209.2	XA	
TCS-30B					47.38	101.0	2.1	471.8	2.65	5.0	432.05	245.0	XA	
TCS-31A		8.70	9.00	BQ	47.30	101.3	2.1	471.9	2.65	7.5	519.40	295.6	XA	
TCS-31B					47.42	100.6	2.1	469.7	2.64	10.0	562.14	318.3	XA	
TCS-32A		12.00	12.30	BQ	47.22	99.3	2.1	459.7	2.64	10.0	638.80	364.8	XA	
TCS-32B					47.32	100.4	2.1	464.2	2.63	12.5	722.21	410.7	XA	
TCS-32C					47.21	99.0	2.1	456.9	2.64	15.0	815.74	466.0	XA	
TCS-33A		12.30	12.70	BQ	47.18	101.0	2.1	466.0	2.64	15.0	764.76	437.4	XA	
TCS-33B					47.19	100.9	2.1	466.4	2.64	17.5	736.65	421.2	XA	

TCS-33C					47.20	101.3	2.1	468.2	2.64	20.0	675.35	386.0	3B	
TCS-34A		13.00	13.35	BQ	47.19	101.5	2.2	471.4	2.66	20.0	725.39	414.7	XA	
TCS-34B					47.28	100.9	2.1	470.6	2.66	25.0	808.43	460.5	XA	
TCS-35A		14.70	14.90	BQ	47.19	101.7	2.2	478.5	2.69	27.5	659.23	376.9	XA	
TCS-35B					47.13	100.7	2.1	472.8	2.69	30.0	727.08	416.8	XA	
TCS-36A		24.40	24.80	BSS	47.25	101.1	2.1	485.2	2.74	5.0	313.40	178.7	XA	
TCS-36B					47.26	100.6	2.1	482.4	2.73	10.0	439.36	250.5	XA	
TCS-37A	NSX007	32.40	32.75	BSS	46.87	99.2	2.1	467.6	2.73	15.0	426.80	247.4	XA	
TCS-37B					47.09	101.9	2.2	486.1	2.74	20.0	422.50	242.6	4B	
TCS-37C					47.11	101.2	2.1	473.4	2.68	30.0	682.48	391.5	XA	
TCS-40A		49.00	49.30	LCON	47.52	99.9	2.1	481.0	2.71	2.5	111.15	62.7	5B	
TCS-40B					47.56	100.3	2.1	491.9	2.76	5.0	141.14	79.4	4B	
TCS-41		54.30	54.70	LCON	47.19	101.9	2.2	484.4	2.72	7.5	347.33	198.6	XA	
TCS-42A		54.70	55.00	LCON	47.33	102.4	2.2	490.0	2.72	10.0	212.93	121.0	4B	
TCS-42B					47.35	101.9	2.2	483.3	2.69	10.0	224.36	127.4	4B	
TCS-43A	NSX007	81.30	84.50	LCON	47.38	100.7	2.1	484.5	2.73	12.5	231.87	131.5	XA	
TCS-43B					47.40	98.7	2.1	475.4	2.73	15.0	313.21	177.5	4B	
TCS-44		84.50	81.80	LCON	47.37	100.9	2.1	481.8	2.71	15.0	322.03	182.7	4B	
TCS-45A		84.00	84.30	LCON	47.35	101.8	2.1	483.0	2.70	17.5	632.99	359.5	XA	
TCS-45B					47.39	101.7	2.1	481.6	2.68	20.0	659.23	373.7	XA	
TCS-45C					47.41	99.5	2.1	472.2	2.69	20.0	427.55	242.2	4B	

TCS-46A		98.30	98.70	LCON	47.39	95.4	2.0	457.7	2.72	25.0	600.94	340.7	XA	
TCS-46B					47.37	91.3	1.9	438.3	2.73	27.5	494.85	280.8	3B	
TCS-46C					47.40	95.8	2.0	462.4	2.73	30.0	628.49	356.2	XA	
TCS-47A		110.40	110.75	LCON	47.62	98.9	2.1	478.1	2.71	5.0	354.45	199.0	XA	
TCS-47B					47.62	100.2	2.1	482.5	2.70	10.0	384.63	216.0	3B	
TCS-48A		112.00	112.40	LCON	47.40	101.4	2.1	483.7	2.70	15.0	422.49	239.4	3B	
TCS-48B					47.32	100.4	2.1	476.3	2.70	20.0	512.09	291.2	3B	
TCS-48C					47.39	100.6	2.1	477.1	2.69	25.0	573.20	325.0	XA	
TCS-49		132.20	132.50	LCON	47.29	102.0	2.2	504.0	2.81	30.0	199.07	113.3	6B	
TCS-50A	5.90		6.20	BQ	47.48	102.1	2.1	492.9	2.73	5.0	289.79	163.7	XA	
TCS-50B					47.54	102.3	2.2	491.1	2.71	10.0	382.94	215.7	XA	
TCS-51A	NSX007 6.20		6.50	BQ	47.54	102.0	2.1	490.3	2.71	15.0	411.43	231.8	XA	
TCS-51B					47.48	102.3	2.2	489.5	2.70	20.0	503.65	284.5	XA	
TCS-52A	7.50		7.80	BQ	47.43	102.8	2.2	485.2	2.67	25.0	597.38	338.1	XA	
TCS-52B					47.42	102.6	2.2	486.5	2.69	30.0	637.30	360.9	XA	
TCS-53A	NSX007	18.50	18.80	BSS	47.20	88.4	1.9	420.1	2.72	2.5	228.11	130.4	XA	
TCS-53B					47.14	88.2	1.9	415.2	2.70	5.0	224.56	128.7	4B	
TCS-54A		19.30	19.50	BSS	47.25	101.9	2.2	480.9	2.69	7.5	382.75	218.3	XA	
TCS-54B					47.26	102.6	2.2	484.9	2.70	10.0	439.93	250.8	XA	
TCS-54C					47.26	100.0	2.1	476.3	2.72	12.5	496.72	283.2	XA	

TCS-55A		20.20	20.50	BSS	47.12	102.2	2.2	482.4	2.71	15.0	480.04	275.3	XA	
TCS-55B					47.15	101.9	2.2	479.9	2.70	17.5	504.97	289.2	XA	
TCS-56A		20.50	20.90	BSS	47.19	101.6	2.2	479.8	2.70	20.0	594.94	340.2	XA	
TCS-56B					47.09	101.8	2.2	480.8	2.71	22.5	603.75	346.7	XA	
TCS-57A		25.80	26.10	BSS	47.15	100.6	2.1	474.4	2.70	25.0	644.24	369.0	XA	
TCS-57B					47.07	101.4	2.2	481.1	2.73	30.0	360.08	206.9	2B	

Note: All tests were conducted according to the ISRM's suggested method.

Table A.0-4 Micro Seismic event register database

Jan-23	Time of Occurance	Location (mL)	Nearest working level	Block name	Co-ordinates			Magnitude	logEs/Ep	logP	logM	logE	AppVol	Hypo-PPV(mm/s)	Hypo-EPPI(m)	Rockmass Damage Report	Surface Observation	IMS Correspondence
					X	Y	Z											
4-Jan-23	04:45	1523	1457ml	55	2425	-170	-250	1.1	3.5	0.4	10.9	5.9		24	67	No damage recorded	–	–
4-Jan-23	05:08	1530	1507ml	56	2586	-164	-257	0.2	1.1	-0.6	10	4.7		18	36	–	–	–
5-Jan-23	17:00	1510	1507ml	61	3021	-426	-237	0.6	0.6	0.1	10.6	4.9		17	41	–	–	–
10-Jan-23	16:58	1500	1490ml	56	2513	-133	-227	0.6	0.3	0.2	10.7	4.7		11	50	–	–	–
11-Jan-23	05:03	1535	1507ml	56	2596	-159	-262	0.6	7.2	-0.3	10.2	5.5		38	38	–	–	–
11-Jan-23	16:57	1532	1507ml	56	2586	-161	-259	0.9	4	0.2	10.7	5.8		58	34	–	–	–
12-Jan-23	05:07	1540	1507ml	57	2572	-136	-267	0.7	1.6	0	10.5	5.2		545	5	–	–	–
12-Jan-23	17:00	1563	1507ml	56	2581	-163	-290	0.6	5.4	-0.3	10.3	5		43	34	–	–	–
13-Jan-23	05:12	1542	1507ml	56	2573	-127	-269	0.7	1.9	0.1	10.6	5.3		1158	4	–	–	–

14-Jan-23	05:06	1540	1507ml	56	2546	-129	-267	0.9	0.4	0.6	11.1	5.2		50	25	–	–	–
14-Jan-23	18:17	1571	1507ml	56	2553	-133	-298	0.4	0.8	-0.1	10.4	4.8		53	19	–	–	–
16-Jan-23	05:12	1519	1507ml	56	2579	-163	-246	0.8	3.2	0.1	10.6	5.6		52	33	–	–	–
16-Jan-23	17:05	1532	1507ml	56	2569	-127	-259	0.3	1.2	-0.3	10.2	4.7		622	4	–	–	–
17-Jan-23	05:12	1534	1507ml	56	2579	-156	-261	0.7	3.7	-0.1	10.4	5.4		62	26	–	–	–
19-Jan-23	16:59	1502	1490ml	56	2533	-134	-229	0.9	0.3	0.5	11	5		31	32	–	–	–
22-Jan-23	06:04	1569	1507ml	56	2546	-128	-296	0.6	0.8	0	10.5	4.9		40	25	–	–	–
22-Jan-23	17:04	1509	1490ml	56	2517	-147	-236	0.4	0.3	0	10.5	4.5		11	45	–	–	–
23-Jan-23	05:27	1542	1507ml	56	2543	-132	-269	0.6	1.8	-0.1	10.4	5.1		41	28	–	–	–
25-Jan-23	05:18	1561	1507ml	56	2553	-116	-288	0.6	0.9	0	10.5	5		46	23	–	–	–
25-Jan-23	17:07	1534	1507ml	56	2584	-141	-261	0.9	1.9	0.2	10.7	5.5		144	16	–	–	–
26-Jan-23	00:31	889	1340ml	51	1668	-334	384	0.5	0.2	0.1	10.6	4.5		–	698	–	–	–
27-Jan-23	06:59	1432	1407ml	62	3024	-615	-159	0.1	0.1	-0.1	10.4	3.8		–	61	–	–	–
28-Jan-23	05:03	1504	1507ml	56	2532	-121	-231	0.8	0.2	0.5	11	4.8		17	40	–	–	–
28-Jan-23	17:13	1546	1507ml	56	2559	-148	-273	0.8	2.5	0.1	10.6	5.5		92	21	–	–	–
28-Jan-23	21:09	1379	1373ml	61	2948	-546	-106	0.6	0.2	0.4	10.9	4.6		14	41	–	–	–
29-Jan-23	04:59	1514	1507ml	56	2578	-127	-241	0.6	2.3	-0.1	10.4	5.3		337	8		–	–
29-Jan-23	17:00	1530	1507ml	56	2567	-134	-257	0.8	3.1	0	10.6	5.5		889	5	–	–	–
30-Jan-23	17:38	1524	1490ml	56	2533	-157	-251	0.7	2.7	-0.1	10.5	5.4		42	32	–	–	–
Feb-23	**Time of Occurance**	**Location (mL)**	**Nearest working level**	**Block name**	**Co-ordinates**			**Magnitude**	**logEs/Ep**	**logP**	**logM**	**logE**	**AppVol**	**Hypo-PPV(mm/s)**	**Hypo-EPPI(m)**	**Rockmass Damage Report**	**Surface Observation**	**IMS Correspondence**
					X	**Y**	**Z**											

1-Feb-23	05:02	1504	1507ml	56	2551	-102	-231	0.9	0.4	0.5	11	5.1		27	35	–	–	–
1-Feb-23	17:13	1527	1507ml	56	2555	-139	-254	0.7	1.2	0.1	10.7	5.2		88	18	–	–	–
2-Feb-23	05:00	1489	1490ml	56	2539	-124	-216	0.2	0.2	-0.2	10.3	4.2		3	31	–	–	–
2-Feb-23	08:38	1486	1490ml	55	2493	-86	-213	1	1.1	0.5	11	5.5		235	12	–	–	–
2-Feb-23	17:03	1471	1473ml	56	2511	-142	-198	0.7	0.2	0.4	10.9	4.7		12	46	–	–	–
3-Feb-23	16:58	1521	1507ml	56	2578	-90	-248	0.1	0.5	-0.5	10	4.3		–	44	–	–	–
3-Feb-23	18:02	1504	1490ml	55	2487	-120	-231	0.3	0.5	-0.2	10.3	4.6		17	34	–	–	–
4-Feb-23	04:58	1494	1490ml	55	2522	-114	-221	0.9	0.4	0.5	11	5.1		17	50	–	–	–
4-Feb-23	17:03	1555	1507ml	56	2529	-125	-282	0.3	1.8	-0.4	10.1	4.8		16	42	–	–	–
5-Feb-23	04:57	1457	1473ml	56	2526	-117	-184	0.6	0.3	0.3	10.8	4.7		11	50	–	–	–
6-Feb-23	23:33	1445	1407ml	63	3069	-657	-172	0.9	0.2	0.7	11.2	5		18	43	–	–	–
7-Feb-23	04:53	1500	1473ml	55	2506	-136	-227	0.9	0.3	0.6	11.1	5.1		18	49	–	–	–
7-Feb-23	17:02	1483	1473ml	55	2507	-131	-210	0.7	0.3	0.3	10.8	4.8		13	46	–	–	–
8-Feb-23	17:01	1492	1490ml	55	2513	-113	-219	0.9	0.6	0.4	10.9	5.2		24	42	–	–	–
9-Feb-23	17:20	1508	1490ml	59	2827	-363	-235	0.9	0.2	0.6	11.1	4.9		14	49	–	–	–
9-Feb-23	17:20	1572	1507ml	59	2811	-375	-299	0.8	0.2	0.6	11.1	4.9		14	50	–	–	–
10-Feb-23	05:11	1479	1473ml	56	2511	-139	-206	0.9	0.9	0.4	10.9	5.4		23	47	–	–	–
11-Feb-23	05:31	1574	1507ml	56	2530	-102	-301	0.7	1.3	0.2	10.7	5.3		20	50	–	–	–
11-Feb-23	17:01	1489	1473ml	55	2498	-129	-216	0.7	0.3	0.4	10.9	4.9		20	39	–	–	–
12-Feb-23	05:25	1521	1507ml	56	2544	-111	-248	0.6	1.8	0	10.5	5.2		35	33	–	–	–
12-Feb-23	17:06	1567	1507ml	56	2533	-113	-294	0.4	0.5	-0.1	10.4	4.6		12	42	–	–	–
15-Feb-23	05:16	1515	1507ml	56	2541	-99	-242	0.4	0.6	-0.1	10.4	4.7		13	44	–	–	–

16-Feb-23	05:10	1547	1507ml	60	2898	-324	-274	0	0.1	-0.3	10.3	3.7		–	56	–	–	–
17-Feb-23	17:20	1530	1507ml	56	2526	-117	-257	0.8	1	0.3	10.8	5.3		21	47	–	–	–
19-Feb-23	05:00	2620	1507ml	63	3334	-200	-1347	0.8	1.4	0.2	10.8	5.4		–	1179	–	–	–
19-Feb-23	16:58	1492	1473ml	55	2494	-137	-219	0.8	0.5	0.4	11	5.1		21	42	–	–	–
20-Feb-23	05:13	1589	1507ml	60	2927	-299	-316	0.5	0.6	0	10.5	4.8		–	108	–	–	–
20-Feb-23	17:02	1505	1457ml	55	2437	-145	-232	0.8	12.9	-0.2	10.3	5.9		55	40	–	–	–
21-Feb-23	17:01	1547	1507ml	56	2521	-123	-274	0.6	0.8	0.1	10.6	5		14	51	–	–	–
22-Feb-23	05:05	1518	1473ml	55	2488	-146	-245	0.9	1.8	0.3	10.8	5.5		28	48	–	–	–
23-Feb-23	04:59	1479	1473ml	55	2490	-135	-206	0.7	0.9	0.1	10.6	5.1		24	38	–	–	–
24-Feb-23	05:09	1516	1507ml	56	2532	-113	-243	0.8	1.4	0.2	10.7	5.4		28	43	–	–	–
25-Feb-23	05:20	1538	1507ml	55	2526	-90	-265	0.7	1.1	0.1	10.7	5.2		25	40	–	–	–
26-Feb-23	05:23	1580	1507ml	55	2508	-99	-307	0.8	1	0.3	10.8	5.3		38	32	–	–	–
28-Feb-23	05:03	1469	1457ml	55	2448	-126	-196	0.9	2.4	0.2	10.7	5.6		122	19	–	–	–
Mar-23	**Time of Occurance**	**Location (mL)**	**Nearest working level**	**Block name**	**Co-ordinates**			**Magnitude**	**logEs/Ep**	**logP**	**logM**	**logE**	**AppVol**	**Hypo-PPV(mm/s)**	**Hypo-EPPI(m)**	**Rockmass Damage Report**	**Surface Observation**	**IMS Correspondence**
					X	**Y**	**Z**											
1-Mar-23	00:33	-10791	1340ml	70	9208	-27921	12064	1.5	32.1	0.5	11	7		–	29976	No damage recorded	–	–
1-Mar-23	05:01	1496	1457ml	55	2444	-130	-223	1.1	6.4	0.3	10.8	6.1		134	25	No damage recorded	–	–
1-Mar-23	17:20	1575	1507ml	60	2895	-298	-302	0.6	0.8	0.1	10.6	5		10	64	–	–	–
2-Mar-23	00:08	924	1340ml	58	2326	-771	349	0.6	0.1	0.5	11	4.3		–	648	–	–	–
2-Mar-23	16:58	1493	1490ml	55	2489	-90	-220	1.3	0.6	0.9	11.5	5.7		475	9	No damage recorded	–	–

3-Mar-23	05:03	1488	1457ml	55	2425	-144	-215	1	2.3	0.3	10.8	5.7		31	48	No damage recorded	–	–
3-Mar-23	17:53	1537	1507ml	55	2524	-91	-264	0.4	0.8	-0.2	10.3	4.7		16	39			
3-Mar-23	18:04	1513	1340ml	57	2215	-827	-240	0.5	71.3	-0.8	9.7	6.1		–	630			
4-Mar-23	05:05	1134	1340ml	52	2030	-292	139	0.1	0.2	-0.2	10.3	4.1		–	346			
4-Mar-23	21:27	770	1340ml	60	2442	-1054	503	0.4	0.1	0.2	10.7	4.2		–	871			
5-Mar-23	05:00	1486	1457ml	55	2441	-123	-213	1.1	4.5	0.3	10.9	6		129	24	No damage recorded	–	–
5-Mar-23	08:44	927	1340ml	57	2291	-718	346	1.3	0.4	1	11.5	5.6		–	627	No damage recorded		
5-Mar-23	17:33	1491	1507ml	59	2912	-256	-218	0.7	0.5	0.3	10.8	5		–	107			
6-Mar-23	05:03	1505	1490ml	56	2525	-129	-232	0.5	0.5	0	10.5	4.7		15	41			
6-Mar-23	05:06	1496	1473ml	56	2521	-177	-223	0.1	8.3	-0.9	9.6	5		22	38			
6-Mar-23	22:13	1615	1507ml	59	2856	-330	-342	0.3	0.1	0.1	10.6	4.1		–	119			
7-Mar-23	05:07	1529	1490ml	56	2513	-174	-256	1	0.3	0.7	11.2	5.2		15	58	No damage recorded	–	–
7-Mar-23	17:28	1468	1457ml	55	2439	-114	-195	0.9	4.6	0.1	10.6	5.8		94	25	–	–	–
8-Mar-23	07:04	1112	1340ml	51	1801	-290	161	0.7	0.9	0.2	10.7	5.2		–	466	–	–	–
8-Mar-23	07:04	1095	1340ml	51	1817	-269	178	0.5	0.4	0.1	10.6	4.7		–	453	–		–
8-Mar-23	17:04	1560	1507ml	56	2517	-121	-287	0.3	0.5	-0.2	10.3	4.4		–	77	–	–	–
9-Mar-23	07:07	1295	1340ml	60	2842	-529	-22	0.8	0.2	0.5	11	4.8		16	41	–	–	–
10-Mar-23	05:22	1539	1507ml	55	2512	-117	-266	0.9	0.6	0.5	11	5.2		19	50	–	–	–
11-Mar-23	05:04	1592	1507ml	55	2507	-97	-319	0.6	0.4	0.2	10.7	4.7		24	30	–	–	–
12-Mar-23	05:20	1476	1457ml	55	2489	-137	-203	0.4	5.2	-0.5	10	5.2		34	34	–		–

13-Mar-23	17:01	1487	1473ml	56	2529	-147	-214	0.2	0.4	-0.2	10.3	4.4		20	28	–	–	–
13-Mar-23	19:08	935	1340ml	51	1465	-129	338	0.1	0.9	-0.6	10	4.4		–	743	–	–	–
14-Mar-23	05:15	1500	1490ml	56	2533	-134	-227	0.5	0.3	0.1	10.6	4.6		21	31	–	–	–
14-Mar-23	12:57	1008	1340ml	51	1797	-261	265	0.7	0.3	0.4	10.9	4.8		–	511	–	–	–
14-Mar-23	17:00	1507	1490ml	56	2526	-127	-234	0.7	0.3	0.4	10.9	4.8		17	41	–	–	–
15-Mar-23	05:18	1509	1490ml	56	2528	-132	-236	0.6	0.4	0.2	10.7	4.8		19	37	–	–	–
15-Mar-23	05:46	1508	1507ml	62	3078	-436	-235	0.5	0.2	0.2	10.8	4.5		11	44	–	–	–
15-Mar-23	05:46	1490	1507ml	62	3083	-430	-217	0.6	0.2	0.3	10.8	4.5		–	54	–	–	–
15-Mar-23	05:18	1480	1473ml	56	2521	-161	-207	0.6	0.3	0.2	10.7	4.7		21	32	–	–	–
15-Mar-23	08:34	8397	1340ml	51	-5329	-4875	-7124	0.9	36.4	-0.2	10.3	6.3		–	11336	–	–	–
15-Mar-23	17:19	1505	1490ml	56	2521	-136	-232	0.6	0.2	0.3	10.8	4.6		13	43	–	–	–
16-Mar-23	05:04	1497	1507ml	55	2522	-75	-224	0.3	0.4	-0.1	10.4	4.5		17	33	–	–	–
17-Mar-23	17:10	1532	1507ml	56	2535	-104	-259	1.3	0.9	0.8	11.3	5.8		31	52	–	–	–
18-Mar-23	03:47	931	1340ml	51	1800	-265	342	0.2	0.2	-0.1	10.4	4.1		–	564	–	–	–
18-Mar-23	17:04	1531	1507ml	56	2521	-120	-258	0.9	0.5	0.5	11	5.2		14	58	–	–	–
19-Mar-23	05:54	1491	1473ML	55	2437	-113	-218	1	5.3	0.2	10.8	6		53	42	No damage recorded	–	–
21-Mar-23	05:02	1474	1457ML	55	2482	-136	-201	0.7	7	-0.2	10.3	5.7		55	33	–	–	–
23-Mar-23	16:59	1491	1457ML	55	2474	-130	-218	0.3	0.8	-0.3	10.2	4.6		17	34	–	–	–
24-Mar-23	05:18	1477	1457ML	55	2470	-126	-204	1	1.5	0.4	10.9	5.6		78	25	–	–	–
24-Mar-23	17:31	1512	1490ml	56	2515	-136	-239	0.7	0.3	0.4	10.9	4.8		11	54	–	–	–
25-Mar-23	05:02	1483	1440ml	55	2401	-141	-210	1	5.6	0.2	10.8	6		25	69	No damage recorded	–	–

M

25-Mar-23	04:51	1233	1340ml	52	2015	-162	40	0.2	0.4	-0.2	10.3	4.3		–	211	–	–	–
25-Mar-23	17:00	1494	1490ml	55	2519	-115	-221	0.9	0.3	0.5	11	5		15	48	–	–	–
26-Mar-23	04:51	1471	1440ml	55	2412	-133	-198	1.1	4.5	0.4	10.9	6		40	52	No damage recorded	–	–
26-Mar-23	20:55	1417	1390ml	64	3125	-690	-144	0.2	0.5	-0.3	10.2	4.4		–	47	–	–	–
27-Mar-23	05:07	1493	1457ml	55	2465	-143	-220	1	1.8	0.4	10.9	5.7		33	46	–	–	–
27-Mar-23	17:00	1511	1457ml	55	2400	-122	-238	0.8	4.5	0	10.5	5.7		14	83	–	–	–
28-Mar-23	07:52	1023	1340ml	54	2052	-477	250	0.4	0.2	0.1	10.6	4.4		–	521	–	–	–
28-Mar-23	17:01	1496	1490ml	56	2512	-136	-223	0.9	0.3	0.5	11	5		14	52	–	–	–
29-Mar-23	05:05	1478	1440ml	55	2408	-125	-205	1	6	0.2	10.7	6		31	60	–	–	–
31-Mar-23	17:02	1483	1473ml	56	2516	-136	-210	0.5	0.3	0.2	10.7	4.6		11	45	–	–	–
31-Mar-23	05:11	1480	1457ml	55	2416	-107	-207	0.9	4.3	0.2	10.7	5.8		30	53	–	–	–
Apr-23	**Time of Occurance**	**Location (mL)**	**Nearest working level**	**Block name**	**Co-ordinates**			**Magnitude**	**logEs/Ep**	**logP**	**logM**	**logE**	**AppVol**	**Hypo-PPV(mm/s)**	**Hypo-EPPI(m)**	**Rockmass Damage Report**	**Surface Observation**	**IMS Correspondence**
					X	**Y**	**Z**											
1-Apr-23	04:58	1404	1507ml	60	2984	-247	-131	0.5	1.3	-0.1	10.4	5		–	175		–	–
1-Apr-23	16:56	1549	1507ml	55	2504	-134	-276	0.8	0.3	0.5	11	5		–	77		–	–
2-Apr-23	17:28	1497	1507ml	55	2545	-40	-224	0.1	0.5	-0.5	10	4.2		–	65		–	–
3-Apr-23	04:58	1556	1507ml	55	2496	-132	-283	0.9	0.4	0.6	11.1	5.1		–	78		–	–
3-Apr-23	09:05	1473	1473ml	62	2978	-637	-52	1.3	0.5	1.2	11.7	5.9		124	22	No damage recorded	–	–
3-Apr-23	17:20	1547	1490ml	55	2485	-145	-274	0.6	0.4	0.2	10.7	4.8		–	82		–	–
4-Apr-23	05:05	2040	1507ml	54	2300	-175	-767	0.8	0.6	0.3	10.8	5.1		–	568		–	–

N

4-Apr-23	17:04	1520	1507ml	55	2513	-102	-247	0.9	0.3	0.6	11.1	5.1		23	41		–	–
5-Apr-23	05:20	1613	1507ml	60	2903	-352	-340	0.4	0.9	-0.2	10.3	4.8		–	108		–	–
6-Apr-23	09:53	1359	1340ml	63	3052	-744	-86	1.5	0.5	1.2	11.7	5.9		23	69	No damage recorded	–	–
7-Apr-23	05:05	1526	1473ml	54	2401	-106	-253	0.9	8.6	0	10.5	6		18	83			
7-Apr-23	17:05	1595	1507ml	60	2945	-318	-322	0.3	0.6	-0.2	10.3	4.6		–	110			
7-Apr-23	17:05	1571	1507ml	60	2930	-339	-298	1.1	0.3	0.8	11.4	5.4		12	76	No damage recorded		
8-Apr-23	17:14	1530	1507ml	55	2498	25	-257	0.8	3.8	0.1	10.6	5.7		–	101			
9-Apr-23	05:20	1548	1507ml	60	2939	-347	-275	0.2	0.5	-0.4	10.2	4.3		–	60			
9-Apr-23	17:00	1520	1490ml	55	2481	-132	-247	0.7	1.2	0.1	10.6	5.2		15	55			
10-Apr-23	05:00	1528	1507ml	55	2536	-58	-255	0.4	0.4	0	10.5	4.6		–	54			
10-Apr-23	17:01	1538	1507ml	55	2515	-75	-265	0.7	0.3	0.4	10.9	4.9		17	42			
10-Apr-23	21:56	1485	1473ml	64	3160	-609	-212	0.7	0.2	0.5	11	4.7		–	52			
11-Apr-23	04:55	1518	1490ml	55	2476	-131	-245	1.1	2.4	0.4	10.9	5.8		31	53	No damage recorded	–	–
11-Apr-23	17:10	1575	1507ml	55	2491	-92	-302	0.4	0.3	0	10.5	4.5		–	72		–	–
12-Apr-23	04:54	1633	1440ml	53	2201	-180	-360	0.8	0.9	0.2	10.8	5.2		–	271		–	–
16-Apr-23	05:06	1513	1457ml	55	2408	-130	-240	0.8	16.2	-0.2	10.3	6		20	80		–	–
16-Apr-23	17:02	1500	1473ml	55	2472	-121	-227	1.1	1	0.6	11.2	5.6		53	34	No damage recorded	–	–
17-Apr-23	05:06	1532	1507ml	55	2492	-85	-259	0.1	0.4	-0.4	10.1	4.1		14	29		–	–
18-Apr-23	05:01	1482	1473ml	55	2466	-119	-209	1.1	1	0.6	11.1	5.6		101	21	No damage recorded	–	–

18-Apr-23	17:22	1465	1440ml	55	2412	-113	-192	1	9.1	0.1	10.6	6.1		42	51	No damage recorded	–	–
19-Apr-23	05:04	1493	1473ml	55	2466	-120	-220	0.8	1.1	0.3	10.8	5.3		46	29		–	–
21-Apr-23	17:45	1485	1457ml	54	2400	-104	-212	1.9	2.6	1.4	11.9	6.8		77	58	No damage recorded	–	–
22-Apr-23	07:37	1601	1490ml	55	2461	-197	-328	0.3	0	0.3	10.8	3.7		–	159	–	–	–
23-Apr-23	12:17	1467	1490ml	63	3152	-517	-194	1	0.2	0.3	11.3	5		20	42	Damage was recorded on 1490ml-Cob-63P5 mining drive junction	–	–
24-Apr-23	00:25	936	1340ml	51	1527	-145	337	0.5	0.3	0.2	10.2	4.6		–	697	–	–	–
24-Apr-23	21:14	875	1340ml	63	2719	-1092	398	0.1	0.1	-0.3	10.3	3.9		–	706	–	–	–
25-Apr-23	05:09	1505	1490ml	55	2502	-121	-232	0.8	0.2	0.6	11.1	4.8		15	44	–	–	–
25-Apr-23	17:01	1492	1490ml	55	2518	-97	-219	0.7	0.7	0.2	10.7	5		22	39	–	–	–
26-Apr-23	03:39	1501	1507ml	63	3135	-539	-228	0.5	0.2	0.2	10.7	4.5		89	11	–	–	–
26-Apr-23	07:02	884	1340ml	53	1838	-628	389	0.6	0.5	0.1	10.7	4.8		–	802		–	–
27-Apr-23	04:05	1381	1373ml	61	2935	-549	-108	0.2	0.1	-0.1	10.4	4		10	31	–	–	–
28-Apr-23	05:16	1470	1507ml	60	2952	-264	-197	0.4	0.2	0.1	10.7	4.3		–	117	–	–	–
28-Apr-23	17:12	1492	1490ml	55	2503	-111	-219	0.8	0.2	0.6	11.1	4.8		22	33	–	–	–
May-23	**Time of Occurance**	**Location (mL)**	**Nearest working level**	**Block name**	**Co-ordinates**			**Magnitude**	**logEs/Ep**	**logP**	**logM**	**logE**	**AppVol**	**Hypo-PPV(mm/s)**	**Hypo-EPPI(m)**	**Rockmass Damage Report**	**Surface Observation**	**IMS Correspondence**
					X	**Y**	**Z**											

1-May-23	05:18	-13846	1340ml	70	-6512	-24130	15119	2.1	6.3	1.5	12	7.3		–	29404	No damage recorded	–	–
1-May-23	05:37	1795	1507ml	54	2326	-117	-522	0.4	0	0.4	10.9	3.8		–	318		–	–
1-May-23	22:14	1538	1507ml	55	2491	-68	-265	0.3	0.2	0	10.6	4.2		13	33		–	–
2-May-23	05:03	1515	1507ml	55	2477	-76	-242	0.1	0.6	-0.5	10	4.3		42	15		–	–
2-May-23	05:02	1500	1473ml	55	2451	-133	-227	1	1.5	0.4	10.9	5.6		29	47	No damage recorded	–	–
2-May-23	17:06	1522	1507ml	60	2901	-302	-249	1.1	1.7	0.5	11	5.7		23	61	No damage recorded	–	–
3-May-23	15:32	1425	1423ml	55	2458	-174	-152	0.1	0	0	10.5	3.7		–	32		–	–
4-May-23	03:47	1104	1340ml	52	1933	-311	169	0.5	0.2	0.1	10.7	4.5		–	419		–	–
5-May-23	17:08	1434	1340ml	61	2856	-677	-161	0.4	0.1	0.2	10.7	4.3		–	153		–	–
8-May-23	17:04	1481	1457ml	54	2413	-87	-208	0.9	15.9	0	10.5	6.2		49	50		–	–
9-May-23	17:03	1499	1457ml	54	2395	-107	-226	1	11.3	0.1	10.6	6.1		30	67	No damage recorded	–	–
10-May-23	05:02	1533	1507ml	55	2503	-128	-260	0.8	0.3	0.5	11	5		–	63		–	–
10-May-23	05:02	1553	1507ml	55	2493	-136	-280	0.9	0.4	0.5	11.1	5.1		–	79		–	–
11-May-23	05:25	1568	1507ml	55	2464	-74	-295	0.4	0.2	0	10.6	4.4		–	68		–	–
11-May-23	12:09	1544	1457ml	56	2489	-220	-271	0.3	0	0.2	10.8	3.9		–	114		–	–
12-May-23	16:59	1491	1473ml	54	2401	-83	-218	0.9	3.9	0.2	10.7	5.8		38	45		–	–
13-May-23	03:10	1452	1440ml	55	2462	-159	-179	0.1	0.1	-0.1	10.4	3.9		–	33		–	–
13-May-23	17:00	1531	1507ml	55	2505	-113	-258	1	0.6	0.5	11.1	5.3		20	50	No damage recorded	–	–
14-May-23	17:08	1543	1507ml	55	2477	-65	-270	0.8	0.7	0.4	10.9	5.2		25	40		–	–

15-May-23	15:57	1365	1440ml	56	2620	-136	-92	0.1	0	-0.1	10.4	3.6		–	123		–	–
16-May-23	09:01	776	1340ml	65	2876	-1274	497	0.9	0.2	0.7	11.2	4.9		–	815		–	–
16-May-23	21:15	2420	1507ml	70	4525	126	-1147	0.1	0.7	-0.5	10	4.3		–	1619		–	–
17-May-23	09:39	1541	1457ml	55	2418	-189	-268	0.1	0.1	-0.1	10.4	3.8		–	121		–	–
18-May-23	21:03	1496	1457ml	62	3035	-570	-223	0.8	0.2	0.5	11	4.9		–	65		–	–
19-May-23	05:03	1516	1507ml	56	2556	-132	-243	0.8	0.9	0.3	10.8	5.2		83	19		–	–
19-May-23	16:58	1561	1507ml	60	2876	-358	-288	0.9	2.4	0.3	10.8	5.7		22	60		–	–
20-May-23	05:41	1509	1507ml	56	2564	-142	-236	0.9	1.4	0.4	10.9	5.5		175	14		–	–
21-May-23	05:01	1499	1490ml	55	2504	-108	-226	0.2	0.1	0	10.5	4		–	33		–	–
22-May-23	21:11	1571	1473ml	58	2660	-370	-298	0.7	0.2	0.5	11	4.7		–	149		–	–
26-May-23	04:58	1472	1507ml	60	2923	-312	-199	0.9	2	0.3	10.8	5.6		18	65		–	–
26-May-23	17:01	1512	1507ml	56	2561	-122	-239	0.9	1	0.4	10.9	5.4		136	15		–	–
27-May-23	17:09	1488	1507ml	56	2562	-122	-215	0.9	0.8	0.4	10.9	5.3		75	21		–	–
28-May-23	17:00	1507	1490ml	56	2561	-156	-234	0.5	0.5	0.1	10.6	4.8		41	22		–	–
29-May-23	05:44	1629	1507ml	60	2894	-376	-356	0.9	2.8	0.2	10.7	5.6		–	124		–	–
29-May-23	21:06	978	1340ml	55	2174	-526	295	0.5	0.2	0.2	10.7	4.5		–	527		–	–
31-May-23	05:32	1523	1507ml	56	2563	-129	-250	0.8	0.7	0.4	10.9	5.2		79	19		–	–
Jun-23	**Time of Occurance**	**Location (mL)**	**Nearest working level**	**Block name**	**Co-ordinates**			**Magnitude**	**logEs/Ep**	**logP**	**logM**	**logE**	**AppVol**	**Hypo-PPV(mm/s)**	**Hypo-EPPI(m)**	**Rockmass Damage Report**	**Surface Observation**	**IMS Correspondence**
					X	**Y**	**Z**											
1-Jun-23	05:11	1595	1507ml	62	3054	-466	-322	0.7	0.1	0.6	11.1	4.5		–	90	–	–	–
		1273														–	–	–

		1273														–	–	–
		1273														No damage recorded	–	–
		1273														–	–	–